ELECTROSTATICS OF GRANULAR FLOW IN PNEUMATIC CONVEYING SYSTEMS

ZHANG YAN

(B.Eng. Tianjin Univ.)

A THESIS SUBMITTED FOR THE DEGREE OF DOCTOR OF PHILOSOPHY

DEPARTMENT OF CHEMICAL AND BIOMOLECULAR ENGINEERING

NATIONAL UNIVERSITY OF SINGAPORE

2006

Acknowledgments

First of all, I would like to express my sincere appreciation to my thesis advisor Professor Chi-Hwa Wang for his guidance throughout this study. Furthermore, I would like to acknowledge National University of Singapore for offering me the research scholarship.

I am truly grateful to Dr. Jun Yao for his invaluable assistance and encouragement which has been greatly helpful and useful for my PhD studies. I would like to extend my appreciation to Professor Yung Chii Liang, Professor Hiroaki Masuda and Professor Shuji Matsusaka for their kind recommendations on electrostatic characterization experiments. Furthermore, I would also like to thank Wee Chuan Lim, Fong Yew Leong, Lai Yeng Lee, Dr. Kewu Zhu, Dr. Yee Sun Wong and Dr. Rensheng Deng for their constructive discussions, as well as lab technicians and other group members for their support.

Finally, I wish to express my profound appreciation to my husband and my parents for their unconditional support. Without such sustained support from my family, I could not complete my studies overseas over four years. Nevertheless, words cannot describe my appreciation for their assistance.

Table of Contents

Summary

Particle charge generation is a significant characteristic in the pneumatic conveying systems and is unavoidable in many industrial processing operations. In the present study, the electrostatic charge phenomena and their effects on granular flow behavior were studied in a pneumatic conveying system. The main parameters used for quantitative characterization were the induced current, particle charge density and the equivalent current of the charged granular flow. These were measured using a digital electrometer, Faraday cage and Modular Parametric Current Transformer (MPCT), respectively. Disperse, half-ring and ring flow patterns corresponding to different electrostatic effects through the horizontal and vertical conveying systems were observed. It was found that the accumulated electrostatic charge increased with decreasing flow rates and became stronger with time. The effects of several factors were investigated and found to be important in determining the charge generation and granular flow patterns. Three similar flow patterns were also studied in a 45 ° inclined pneumatic conveying pipe. Solid concentration and velocity distribution were measured using Electrical Capacitance Tomography (ECT), Particle Image Velocimetry (PIV) and high-speed camera. Solid velocities obtained from measurements data of ECT and PIV systems were compared. High-speed camera images showed three distinct regions in reverse flow. Reverse flow occurred predominantly in a transition region between dense and dilute regions. Analyses of forces acting on single particle showed that reverse flow and ring flow formation may be attributed to electrostatics. This has been validated with a control experiment. Among many factors affecting electrostatic characteristics, attrition effect was

highlighted in this research work. Particle attrition in the rotary valve of a pneumatic conveying system was studied. The dependence of physical properties on attrition behaviour was compared between intact (fresh/unused) and attrited particles. It was observed that attrited particles become more breakable and have lower flowability. Attrition experiments were conducted in a rotary valve and pneumatic conveying system separately and in each case the result could be described reasonably well by the Gwyn function. The influence of particle attrition on electrostatic characteristics was examined. Charge density of attrited particles was higher than that of intact ones, but induced current showed a reverse trend. Finally, the study of hazard of electrostatic generation in pneumatic conveying systems was attempted by analyzing the sensitivity of ECT and the phenomena of spark generation due to the strong electrostatics. The influence to ECT measurement accuracy by electrostatic charge was theoretically analyzed and demonstrated according to the switch capacitor configuration model. Consequently, it was found that electrostatic charge introduced from the bend with sharp angles in pneumatic conveying system influenced the ECT results significantly. This investigation of spark generation summarized the conditions under which the phenomenon of spark could usually be observed. The findings presented here could be a good starting point for future researchers.

List of Tables

List of Figures

List of Symbols

c correlation coefficient, -

c_D drag coefficient, -

C electrical capacitance, F

C_{12} actual capacitance between electrode 1 and 2 in the example of switch capacitor configuration, F

C_{12}' measured capacitance between electrode 1 and 2 in the example of switch capacitor configuration, F

C_{s12} system capacitance in the example of switch capacitor configuration

$\vec{C}$ actual electrical capacitance distribution, F

$\vec{C}'$ measured electrical capacitance distribution, F

d delay time for the cross-correlation, s

D value of d at which c assumes the largest value, s

D_p particle diameter, m

D_{pT} initial particle diameter, m

$\vec{E}$ electric field intensity, N/C

$\vec{F}_D$ aerodynamic drag force, N

$\vec{F}_E$ electrostatic force, N

G exponent characterizing the size distribution of particles, -

$\vec{G}_p$ gravity of one particle, N

I induced current on pipe wall measured from the electrometer, A

$\bar{I}$ averaged induced current on pipe wall, A

I_c equivalent current of a granular flow system due to the motion of charge-carrying particles measured from MPCT, A

i,j dimensionless coordinates in cross-sectional downstream plane 2, -

K empirical constant of Gwyn function, s^{-m}

l vertical distance from pipe wall to object point charge, m

m empirical constant of Gwyn function,-

P perimeter of the projected area, m

q total charge on pipe wall, C

dq point charge on pipe wall, C

Q charge on each particle, C

Q_p particle charge density, C/g

Q_T total charge measured in switch capacitor configuration, C

r distance from point charge on the pipe wall to object point charge, m

R pipe radius, m

Re_p particle Reynolds number, -

R_i radius of inner arc of bend, m

R_o radius of outer arc of bend, m

S projected area, m^2

SF particle mass transported per unit time or solid flow rate, kg/s

t instant time, s

Δt time lag, s

T time period, s

T_c charging time, s

$\vec{u}_g$ translational velocity vectors of gas, m/s

$\vec{u}_{g,a}$ average velocity vectors of gas, m/s

$\vec{u}_p$ translational velocity vectors of particle, m/s

U source voltage to excite electrode, V

U_0 actual voltage between electrode 1 and 2 in the example of switch capacitor configuration, V

U_0' measured voltage between electrode 1 and 2 in the example of switch capacitor configuration, V

U_1 potential on electrode 1 due to the electrostatic charge in the example of switch capacitor configuration, V

U_2 potential on electrode 2 duet to the electrostatic charge in the example of switch capacitor configuration, V

U_s potential difference between electrode 1 and 2 due to electrostatic charge in the example of switch capacitor configuration, V

V pattern velocity of particles, m/s

$\vec{V}$ actual particle velocity distribution, m/s

V_l lateral velocity of particles, m/s

V_x magnitudes of the velocity components in x direction, m/s

V_y magnitudes of the velocity components in y direction, m/s

V_z magnitudes of the velocity components in axial direction, m/s

W mass of the attrited particles that has a size less than $D_{p,}$ kg

W_T mass of the attrited particles having a size less than D_{pT}, kg

X fraction of the initial feed, -

x,y dimensionless coordinates in cross-sectional upstream plane 1, -

z axial coordinate of the ECT electrode location, m

z_1 axial coordinate of the ECT electrode location of upstream plane 1, m

z_2 axial coordinate of the ECT electrode location of downstream plane 2, m

Greek letter

α particle concentration, -

$\overline{\alpha}_s$ instantaneous value of the cross-sectional average particle concentration, -

$\overline{\alpha}_t$ time-averaged particle concentration, -

<α>(z) time-averaged value of $\overline{\alpha}_s$, -

ε strain, -

ε_0 permittivity constant, $C^2/(N \cdot m^2)$

β internal friction angle, °

θ angle between r and l, °

λ linear charge density along pipe wall, C/m

μ_g gas viscosity, kg/(m·s)

ρ_g gas density, kg/m^3

Φ shape factor of particle, -

$d\Phi$ mass fraction of particles, -

Subscript

1, 2 electrode 1 and 2 or ECT plane 1 and 2

g gas phase

p particle phase

T initial or total

Chapter 1. Introduction

1.1 Granular flow in pneumatic conveying system

Granular flow systems are widely used in energy, petrochemical, pharmaceutical, food and material processing industries, where particles can act as staples or catalysts in the operation of transportation or separation. The practical applications of granular systems involve fluidized bed, cyclone separator, coal combustion and pneumatic conveying systems. Investigations of granular flow in pneumatic conveying systems have drawn more attention; since it is essential for the design and operation of granular related industrial works, such as constructing pipelines, granule feeder or conveying pump. Pneumatic conveying systems include transportation of a variety of dry powders or granular solids in gas stream; and the latter is focused on our current study. Research work carried out in this field can be categorized into dilute-phase and dense-phase transport according to the average solid concentration in conveying pipe (Klinzing et al., 1997) and can also be classified in terms of different conveying section including horizontal, vertical and inclined and bend conveying systems. In addition, some studies depend on different granular flow patterns, for example, it has been reported three main types of flow patterns in vertical conveying pipe (Leung and Wiles, 1976) and five sorts of flow patterns in horizontal conveying (Tsuji and Morikawa, 1982). Despite the importance of such materials to the industry and everyday life, their unusual flow behavior, which is different from those of liquids and solids, has not been fully understood. For granular solids transportation, pneumatic conveying systems have numerous advantages: comparatively high levels of safety,

low operational costs, flexibility of layout, convenience of automation and installation and easy of maintenance. However, there exist some problems, for instance, particle attrition, conveying pipe abrasion, electrostatic charge generation and danger caused by the interaction of above-mentioned problems.

Static charge is usually generated due to the friction, collision or rolling between particle and particle or between particle and pipe wall, when particles are transported along conveying pipes, which is named triboelectrification. Two-polarity electrostatics on particle and pipe wall respectively would make particles stick on the conveying pipe or choke in transport facility (Joseph and Klingzing, 1983) and lead to the decrease of transportation efficiency. Occasionally, the electrostatics would cause the malfunction and inaccuracy of some sensitive instruments (Zhu et al., 2004b). Moreover, if the static charge was extremely strong, it would result in instant discharge and cause explosion or fires (Glor, 2003). Itagaki (1998) reported that static electrification is probably the main cause of dust explosions. A number of studies on this phenomenon have been performed by some researchers. Their focus is usually on the relation between transport parameters and the generated electrostatic charge. However, the accompanying physical phenomenon, in particular spark generation, has not been investigated in detail. On the other hand, electrostatics could also be applied to a plenty of industrial processes in granular transport or pneumatic conveying systems. Such applications involve mass flow rate measurement (Matsusaka and Masuda, 2006), separation of mixture powders (Gupta et al., 1993, Yanar and Kwetkus, 1995), powder coating (Kleber and Makin, 1998) and tomography (Machida and Scarlett, 1998). Therefore, in order to avoid the disadvantages but employed well the advantages brought by static charge, it is necessary to investigate

the electrostatics in pneumatic conveying systems. Electrostatic effects and the associated charge generation mechanisms are complex phenomena often dependent on a great many of factors such as physical, chemical, and electrical characteristics of the material used and ambient conditions. This may lead to poor reproducibilities and repeatabilities of experiments. However, the amount of work reported in the literature that involves measuring or calculating electrical charges on particles in granular flow systems has also been limited due to the inherent difficulties in such investigations.

1.2 Electrostatic investigations in pneumatic conveying systems

Granular flow systems have a tendency to acquire electrostatic charges due to friction, collision or rolling between particle and particle or between particle and surface of facilities. In recent years, a great deal of works have been reported on electrostatics studies in pneumatic conveying systems, consisting theoretical and experimental works. Most theoretical works are focused on trying to probe the mechanism of electrostatic. In his research on the static electrification in gas-solid pipe flow, Masuda et al. (1976) explained in theory that the electrostatics is generated by the contact between particles and pipe wall. Subsequently, Masuda and Iinoya (1978) proposed a mechanism of electrification due to polymer particles impacting on metal plates. Based on this, Watano (2006) developed and applied it to the control of electrification in pneumatic conveying of powders. However, in these explanations of charge generations, few research touches the reason for granular material behavior caused by electrostatics, especially investigation of flow patterns in pneumatic conveying transport, which are significant in granular flow systems as Molerus (1996) has already pointed out the first priority of theoretical consideration is the prediction of

the type of flow in his overview of pneumatic transport of solids. Furthermore, the study on flow patterns is the fundamental concepts in pneumatic conveying system and is helpful to understand some problems arisen in the operation, such as granule choking. However, in previous works, flow patterns were generally associated with all kinds of experimental conditions, for instance the gas-solid flow rates, (Tsuji and Morikawa, 1982), or gas pressure, but were not analyzed under electrostatics influence. Besides, some special phenomena of flow patterns are not able to be explained by classical mechanics, thus are supposed to have a relationship with electrostatics.

As for experimental work, a range of investigations were concentrated on factors affecting electrostatics. Kanazawa et al. (1995) investigated charge generation and accumulation on the inner surface of a plastic pipe in a flow system during the transport of powder and found surface charge density and charge polarity of the pipe wall depend on the successive number of tests and pipe material. Furthermore, the charging characteristics of the pipe wall during the transport of glass beads and industrial granules were found to depend on the pipe material and transport method. Such work was attended to the electrification on the pipe wall, whereas with regard to another element in pneumatic conveying systems, Smeltzer et al. (1982) tested glass beads in a pneumatic conveying system and demonstrated that small particles exhibit greater electrostatic effects than larger particles. Matsusaka and Masuda (2003) developed a formulation for the variation of particle charging caused by repeated impacts on a wall and employed the formulation to particle charging in a granular flow where each particle carried a different amount of charge. Nevertheless, these investigations on particle effect neglected attrition effect on electrostatics, which is

another main issue in pneumatic conveying as mentioned in Section 1.1. Attrition often occurs during conveying and processing of particles and causes loss of valuable product, formation of dust and environmental pollution. Some attrition is inevitable and has been reported in a wide range of industries, (Bemrose and Bridgwater, 1987), but it is seldom related to electrostatics including the attrition effect on charge generation and the counteractive by static charge.

The rate of attrition of particles could be expressed by a simple function of initial diameter and time (Gwyn, 1969). The initial rate is a function of initial diameter, whereas the decrease in attrition rate of a given size depends only on time. This equation has been verified by laboratory and commercial data. Paramanathan and Bridgwater developed an annular cell that enables solid attrition to be studied (Paramanathan and Bridgwater, 1983a) and investigated the material behaviour and kinetics of attrition (Paramanathan and Bridgwater, 1983b). Neil and Bridgwater also tested granular materials in an annular attrition cell (Neil and Bridgwater, 1994 and 1999), a fluidized bed and a screw pugmill (Neil and Bridgwater, 1999). For each experiment, the attrition was characterized using the Gwyn function effectively. Bemrose and Bridgwater have indicated attrition was affected by many variables, such as properties of the particles (e.g. size, shape, surface, porosity, hardness and cracks), and categorized mechanical tests as single-particle or multi-particle type; whereas, physical properties of particles would be changed mostly after attrition (Bemrose and Bridgwater, 1987). Furthermore, flow properties are sensitive to particle size and particle size distribution. Attrition also affects the flow behaviour of particles, such as solid flow rate, pipe wall abrasion and the electrostatic charge generation characteristics. The abrasion of pipelines in pneumatic conveying systems

can be as significant as the damage inflicted on the particles. Soo observed that pipeline erosion is most severe around pipe bends (Soo, 1980). Such phenomenon arises due to collisions or friction between particles and pipe wall. Moreover, due to collisions or friction with a different material surface, solid particles in pneumatic conveying systems have the propensity to acquire electrostatic charges (Masuda et al., 1976). A previous experimental work (Inculet et al., 1997) demonstrated that the elbows in a pipeline are the major source of triboelectrification of particles in pneumatic conveying systems and these are also important sites of pipe abrasion. The electrostatic charge generation characteristics of granular materials in a pneumatic conveying system have been investigated. Smeltzer and colleagues studied this phenomenon occurring during pneumatic transport and found that smaller particles had greater electrostatic effects (Smeltzer et al., 1982). Electrostatic characteristics have been applied to measure the mass flow rate, but there have been few investigations on the relationship between electrostatics and solid flow rate (Mathur and Klinzing, 1984).

In addition, experimental conditions have been discovered as significant characters to influence electrostatics. Masuda et al. (1977) found that powder flow rate, air velocity, pipe size; bend and powder feeding all affect electrostatics when they studied gas-solid suspensions flowing in steel and insulating-coated pipes. Air humidity and conveying velocities were also verified to influence electrostatic charge generation and charge distribution in their work of glass beads flowing in copper pipe loop (Nieh and Nguyen, 1988). They confirmed that when the system moisture content exceeded a cutoff relative humidity (RH) of 76%, the charges on glass beads became effectively neutralized. However, although Inculet et al. (1997) demonstrated that

tribo-electrification occurs at the elbow of conveying system, all these works are limited to that there is not much consideration and comparison on charge distribution in different sections of the pneumatic conveying systems. The comprehension on such is convinced to be benefit to take preventative action on the part, where charges are generated seriously.

Many studies have been carried out on gas-solid flow in horizontal and vertical pipes, while relatively fewer studies are available on solid transport in inclined pipes. These are mainly focused on pressure drop data through the conveying pipes. For example, Levy et al. (1997) developed an analytical model for gas-solid suspension flow through an inclined pipe section, which predicted the ratio of the total pressure drop in an inclined pipe to that of a horizontal pipe and agreed with the experimental data satisfactorily; Hirota et al. (2002) examined the effect of mechanical properties and the angle of an inclined pipe on the pressure drop for the pneumatic conveying of fine powders. Other studies of granular flow focused on the different flow patterns arising from different physical conditions and operating parameters imposed. Zhu et al. (2004a) used computational fluid dynamics simulations to investigate the pneumatic conveying of granular solids through an inclined pipe at different inclinations and reported results on the influence of model parameters, inclination angle, and feeding conditions on the flow patterns. Experiments have also been carried out to study solid flow patterns in pneumatic conveying through vertical and inclined pipes and various flow patterns were observed (Zhu et al. 2003). In their work, regimes such as eroding dune flow and flow over a settled layer were imaged using Electrical Capacitance Tomography (ECT); and some flow regimes with downflow were observed visually. However, detailed analyses were not given. The study on downflow or reverse flow

has not drawn much attention among researchers. Among the limited literature on this subject, most have concentrated on heat transfer investigations in liquid systems. Maré et al. (2005) investigated the laminar flow of water in an inclined isothermal tube numerically and experimentally using three dimensional elliptical model and Particle Image Velocimetry (PIV) respectively and concluded that the combination of the Reynolds number, Grashof number and Prandtl number determined the phenomena of reverse flow.

On the other hand, the effects of electrostatic charge on the flow of granular material have been studied by a few research workers. Zhang et al. (1996) carried out a comprehensive and complete study of the effects of electrostatic forces on cohesive particles. On basis of experimental data on instantaneous velocities of shale particles in a dilute gas/solid system, it was found that the particles oscillate about the mean values in a chaotic manner, the velocity distribution could be approximated by the Maxwellian distribution function, and kinetic theory was a very promising approach to describe gas/particle flow systems. Al-Adel et al. (2002) examined the characteristics and extent of lateral segregation arising from static electrification in riser flows, and analyzed the steady and fully developed gas-particle flow in a vertical riser. However, flow patterns of the granular material which can arise due to such effects in a pneumatic conveying system have not been reported. On the basis of our previous work done in our laboratory, it has been established that electrostatic effects play an important role in determining the flow patterns in a vertical pneumatic conveying system (Rao et al. 2001, Zhu et al. 2003 and 2004b).

Our research group carried out detailed studies of solid flow behavior in pneumatic

conveying systems of various configurations. The complicated dynamics of granular flows had been studied by using Electrical Capacitance Tomography (ECT). It was initially studied pneumatic conveying of solids in horizontal pipes to identify the various flow regimes using ECT (Rao et al. 2001). ECT was then applied to investigate solid flow of pneumatic conveying in vertical and inclined pipes and it is observed seven flow patterns in vertical riser (Zhu et al., 2003). More recently, our research group has already attempted a study of electrostatic charge generation in pneumatic conveying systems. This was initiated by experiments done by Zhu et al. (2004b), who observed the occurrence of electrostatics in their experiments. They reported that the non-conducting wall generally attains static charges arising from particle-wall collisions at the initial stage of the conveying process till it reaches equilibrium. Consequently, the perturbations in the capacitance signal due to charge accumulation are found to be larger at smaller air superficial velocity and denser flow regimes give larger wall residual charges. This presumably suggests that the presence of electrostatic charges has significant influence on the accuracy of ECT results. However, this work was restricted in presenting the influence of electrostatic charges on the accuracy of ECT results, but was lacked of thorough analysis on electrostatic characters in pneumatic conveying systems. For the measurement of the electric field, the electrostatic effects on solid flow behaviour as well as the influence of various external conditions on its strength have been characterized (Zhu et al., 2004b; Yao et al., 2004). This early work concluded that the accuracy of ECT result under the occurrence of electric field is an important research issue and should be explored further. Therefore, current research will continue to operate the experiment in the same conveying systems as the previous work, and to investigate the electrostatics more deeply.

1.3 Significance and organization of current research

The aim of this research was to extend the existing investigations on electrostatics of granular flow in the entire pneumatic conveying systems and to study the flow behavior of solid particles under the effects of electrostatic charge generation in pneumatic conveying systems. It is possible from this extensive research program that a set of standard operating procedures for the diagnosis, troubleshooting and effective process control of plant equipment and unit operations utilizing multiphase systems may be useful to the chemical or pharmaceutical industries. This study firstly reports three flow patterns observed in both vertical and horizontal conveying pipes, which are named as disperse, half-ring and ring flow depending on different airflow rates. The induced current on pipe wall and particle charge density measured for these three flow patterns by electrometer and Faraday cage respectively will provide a general concept that these phenomena can be explained according to the electrostatic characters in conveying systems. Subsequently and analogously, electrostatics for additional flow patterns, disperse, reverse and half-ring flow, investigated on 45 degree inclined conveying pipe and associated solid fraction image and velocity explored by using ECT, PIV and high speed camera will offer an analysis from the electrostatic forces and the usual hydrodynamics forces present between the gas and solid phases, which may interpret the forming of flow patterns. Among the numerous factors affecting on electrostatics of the granular flow, such as air humidity and pipe materials analyzed in this research, another significant element, granular attrition, is highlighted. The features of particle attrition emphasized in conveying systems, including granular physical properties and their variation by attrition, would explain

particle size variation with attrition time and effect of attrition on electrostatics in pneumatic conveying systems. Such physical properties were measured according to amounts of experiment, including compression, granulate and shear strength tests. Finally, the study of hazards to electrostatic charge generation in pneumatic conveying systems is to be carried out quantitatively, which is observed from previous experimental works and involves spark generation resulting from rapid discharging across an insulating medium and sensitivity of ECT disturbed by electrostatics. It would give a threshold and caution to the subsequent investigator. However, due to the time limit, this part is focused on some pilot works and is not discussed in detail here.

In general, this thesis offers perspectives on the electrostatics of granular flow in pneumatic conveying systems. It consists of seven chapters. The first chapter describes briefly the background of pneumatic conveying systems, the overview of previous electrostatic characteristics studies on such system and the motivation and scopes of current research work. The second chapter completely describes the experimental apparatus, methods and details. The third chapter investigates preliminarily the electrostatics of granular flow on vertical and horizontal conveying pipes. The forth chapter further extends the study of electrostatics on the pneumatic transport of granular materials to an inclined conveying pipe. The fifth chapter presents particle attrition due to rotary valve feeder in a conveying system and its electrostatic and mechanical characteristics. The sixth chapter provides a pilot work with regard to the sensitivity of ECT and spark generation on pneumatic conveying systems due to the strong electrostatic charge. The conclusions and recommendations are summarized in the final chapter. This work aims to provide insights into the

relationship between the solids flow behavior and electrostatic charges and thereby utilize the benefits and eliminate the inconvenience and insecurity aroused by electrostatics in industrial powder handling.

Chapter 2. Experimental

2.1 Experimental setup

2.1.1 Circulatory conveying system for Chapter 3 (Experimental setup A)

The experimental setup used in our present study was modified from the pneumatic conveying system used by Rao et al. (2001) and Zhu et al. (2003 and 2004b). The schematic diagram of the modified system (Experimental setup A) is given in Figure 2.1, and the experimental conditions are listed in Table 2.1. Solid particles were introduced into the rotary valve and entrained by air flowing from the compressor mains. The rotary valve (General Resource Corp., Hopkins, Minnesota, US) has eight pockets on the rotary and rotates at 30rpm. The inner diameter of the pipe is 40mm, and the length of the vertical pipe section between two smooth 90 °elbows (R_o/R_i=2) is about 2.97m, while the horizontal section is about 4.12m in length. The conveying pipe is made of transparent polyvinyl chloride (PVC) material and has a wall thickness of 5mm. Induced current measurements were placed on the vertical pipe 1.36m away from the bottom elbow. Polypropylene (PP) granules and one type of antistatic powder were used throughout the experiment. Visual observations of the various solid flow patterns that arise during the experiments were facilitated through the use of transparent pipes. The entire configuration is held in position using metal castings and various pipe segments joined by connectors.

Air from the compressor mains flowed through the rotary feeder, driving granules fed into the conveying system from the feed hopper. Control valves (labeled 1, 11 and 14

in Figure 2.1) were used to adjust the air and solid flow rates. The air flow rate was also controlled via a rotameter which allowed a maximum flow rate of 2000L/min. The air humidity was controlled by the dryer (silica gel, labeled 2 in Figure 2.1) at RH=5% and was checked using a high-performance digital thermo-hygrometer (OMEGA RH411, Connecticut, US) before and after each test. As PP granules were fed back to the recycle solid hopper, they passed through a manual valve (labeled 11 in Figure 2.1). Closing valve 11 would enable the solid mass flow rate to be measured using the electronic weight indicator (labeled 13 in Figure 2.1). Valve 14 was used to control the solid feed rate from the solid feed hopper into the conveying system. Ambient temperature was controlled at 28-30℃, and other experimental conditions are listed in Table 2.1

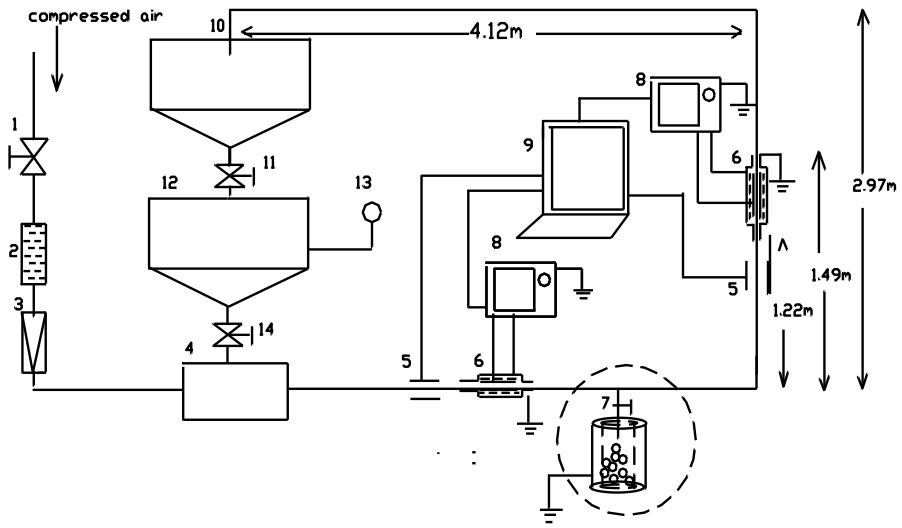

Figure 2.1 Schematic of the pneumatic conveying facility (Experimental setup A used for the measurements presented in Sections 3.1~3.4, 3.5.2 and 3.5.3): 1. Air control valve; 2. Air dryer (silica gel); 3. Rotameter; 4. Rotary valve; 5. MPCT; 6. Induced current measurement; 7. Faraday cage; 8. Electrometer; 9. Computer; 10. Feed recycle hopper; 11. Feed control valve; 12. Intermediate hopper; 13. Electronic weight indicator; 14. Feed control valve.

Table 2.1 Experimental conditions for Chapter 3.

Experimental conditions	Experimental setup A (Figure 2.1)	Experimental setup B (Figure 2.2)
Temperature	28~30 ℃	28~30 ℃
Relative humidity (RH)	5%	5%
Air pressure	500kPa	500kPa
Air flow rate	860~1600L/min	1600L/min
Air superficial velocity	11.4~21.2m/s	21.2m/s
Solid mass flow rate	10.2±2.0g/s~44.4±4.0g/s	44.4±4.0g/s
Particles conveying style	Cycle	No cycle
Particle diameter	2.8mm	2.8mm
Particle material	Polypropylene (PP)	Polypropylene (PP)
Particle density	1123kg/m^3	1123kg/m^3
Pipe material	Polyvinyl chloride (PVC)	Copper
Pipe inner diameter (ID)	40.0mm	50.0mm
Pipe thickness	5.0mm	1.0mm

2.1.2 Single conveying system for Chapter 3 (Experimental setup B)

The experimental setup shown in Figure 2.2 was used to investigate the tribocharging characteristics of PP particles contacting with surfaces of pipe. The conveying pipes were made of copper except at the test section where pipes made of PVC or covered with a polyethylene (PE) film were used. The various layers of materials consisted of PVC (5mm) or PE (0.04mm), conductive adhesive (0.07mm), copper sheet (0.10mm) as electrode, nonconductive adhesive (0.12mm) and copper sheet (0.10mm) as electric shield. The copper electrode was connected to the electrometer and the electric shield was grounded. The whole conveying system was well grounded so that the particl-charging conditions are kept constant during their impact with the metal wall. When the air pressure and flow rate were adjusted to about 500kPa and 1600L/min respectively, dried particles passed through the horizontal pipe, continuously at a rate of 44.4±4.0g/s. Electrostatic charge was generated at the test section and the induced current was measured using the electrometer (ADVANTEST R8252, Tokyo, Japan) and was stored in a computer at intervals of 0.1s. The charge density of the particles was measured by a Faraday cage (ADVANTEST TR8031, Tokyo, Japan). All particles were collected in a metal container and grounded for discharging at the end of each experimental run. VIEW I shows the detailed cross section of the test section following the design used by Matsusaka et al. (2003), which was shaped as a cylinder (ID=50mm, length=72mm).

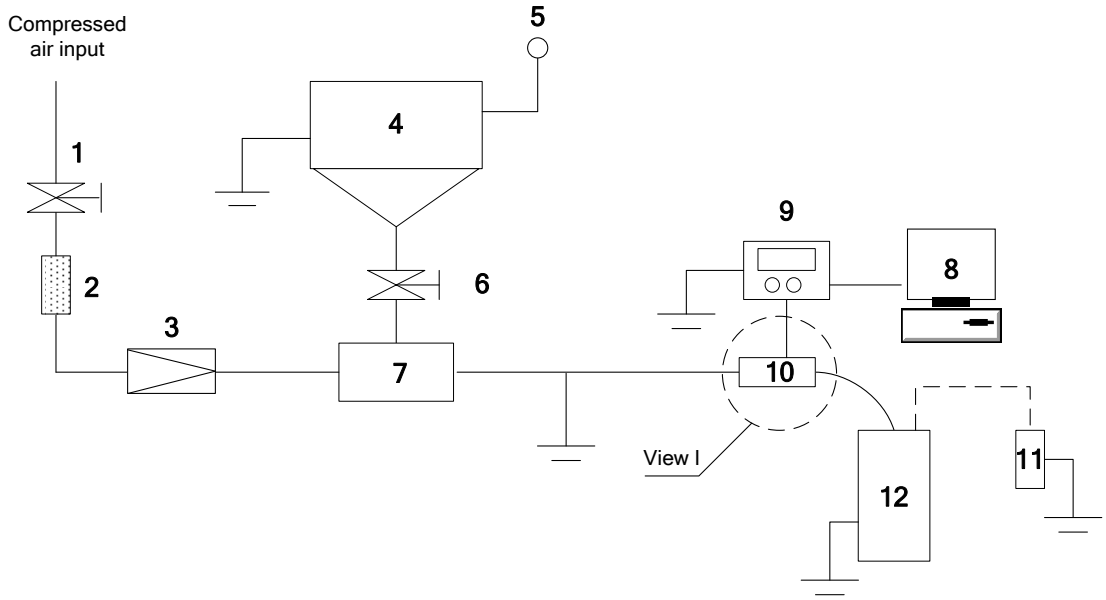

Figure 2.2 Schematic of the pneumatic conveying facility (Experimental setup B used for the measurements presented in Section 3.5.1): 1.Air control valve; 2. Air dryer (silica gel); 3. Rota meter; 4. Feed hopper; 5. Electronic weight indicator; 6. Feed control valve; 7. Rotary valve; 8. Computer; 9. Electrometer; 10. Test segment (detailed shown in View I); 11 Faraday cage; 12. Metal container.

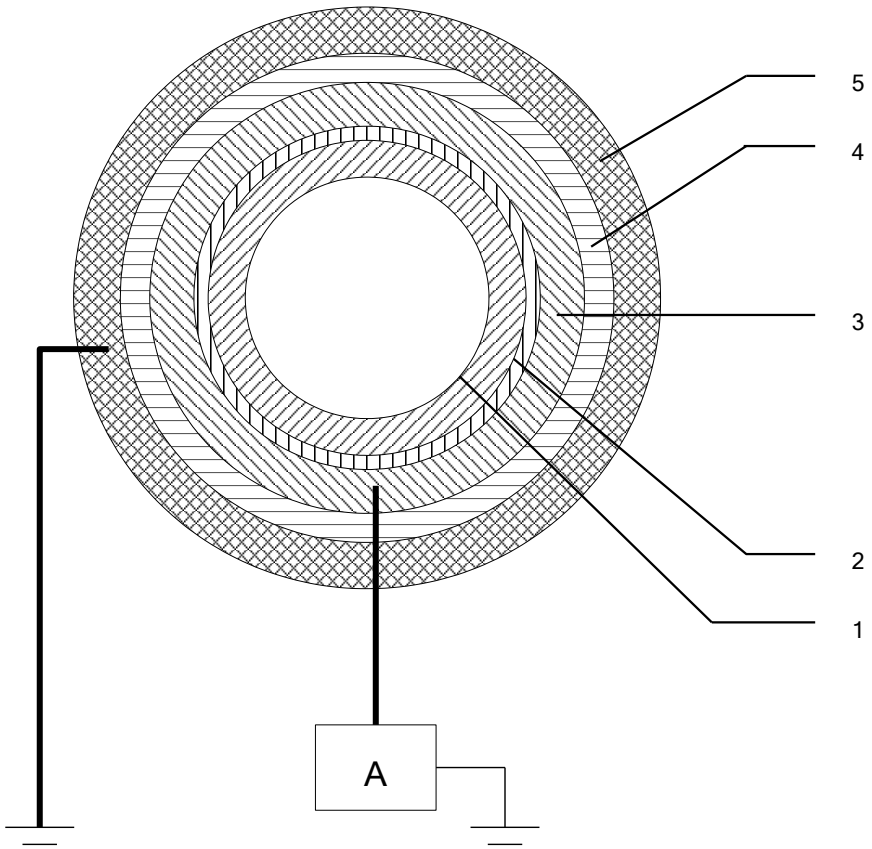

View I Cross section of the test segment (inner diameter 50mm, length 72mm):1. Film (PVC: 5mm/PE: 0.04mm); 2. Conductive adhesive (0.07mm); 3. Copper-electrode (0.10mm); 4. Nonconductive adhesive (0.12mm); 5. Copper-electric shield (0.10mm).

2.1.3 Pneumatic conveying system for Chapter 4

The experimental facility, which was modified from a previous study (Zhu et al. 2003) and used to carry out the measurements, is shown schematically in Figure 2.3; and the experimental conditions are listed in Table 2.2. Air from the compressor was metered and sent to the rotary air lock feeder (General Resources Corp., Hopkins, Minnesota, US), where it entrained the particles. The rotary feeder equipped with eight pockets and a vent at the body of the rotary valve providing the passage of the air leakage, was operated at a fixed speed of 25rpm. The test section consisted of two 4cm-ID horizontal pipes with the distance of 3.41m and the lower one is 4.12m. A 45° inclined pipe (4cm-ID) was connected to the two horizontal pipes. The entire conveying loop was made of PVC pipes.

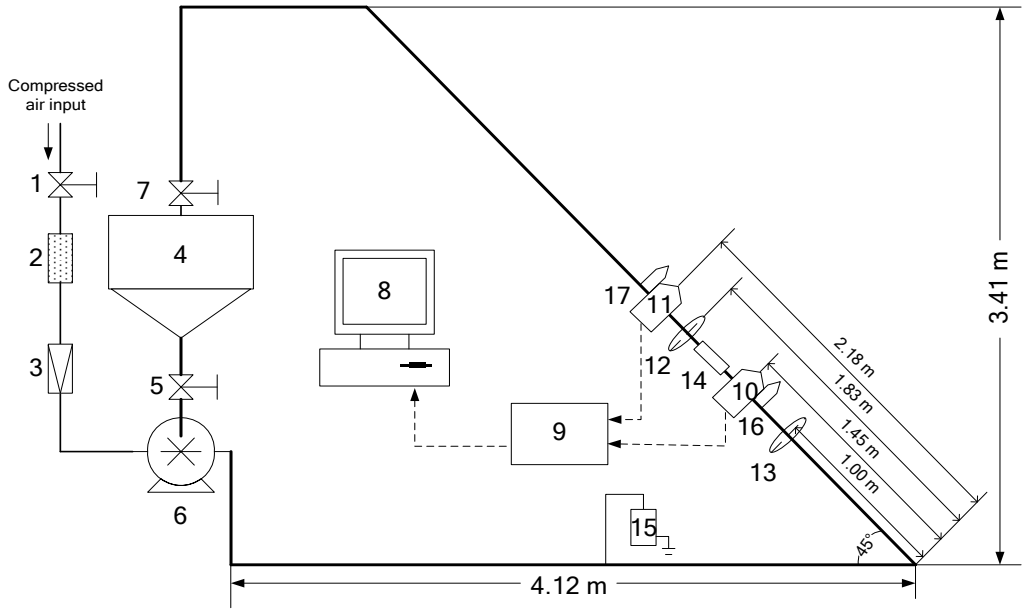

Figure 2.3 Schematic of the pneumatic conveying experiment facility. 1. Air control valve; 2. Dryer; 3. Rotameter; 4. Hopper; 5. Solids feed valve; 6. Rotary valve feeder; 7. Feed control valve; 8. Computer; 9. DAM; 10. ECT plane 1; 11. ECT plane 2; 12. Plane of PIV measurements; 13. Plane of measurements for high speed camera; 14. Measurements for induced current; 15. Measurements for particle charge; 16. Pressure transducer sensor 1; 17. Pressure transducer sensor 2.

Table 2.2 Experimental conditions for Chapter 4.

Air flowrate	1600L/min, 1100L/min, 1000L/min
Air superficial velocity	21.2m/s, 14.6m/s, 13.3m/s
Solids feed valve	75% opening
Roll speed of rotary valve	25rpm
Pipe material	Polyvinyl Chloride (PVC)
Pipe diameter (inner)	40.0mm
Pipe thickness	5.0mm
Particles conveying style	Cycle
Particle material	Polypropylene (PP)
Particle size	2.80mm
Particle density	1123kg/m^3

2.1.4 Pneumatic conveying system and rotary valve for Chapter 5

The experimental setup used in the present study was modified from previous pneumatic conveying system (Yao et al. 2004). The schematic diagram of the modified system is given in Figure 2.4 and the experimental conditions are listed in Table 2.3. Solid particles were introduced into the rotary valve (General Resource Corp., Hopkins, Minnesota, US) (Figure 2.5) and entrained by air flowing from the compressor. The inner diameter (ID) of the pipe was 40mm, and the length of the vertical pipe section between two smooth 90° elbows (R_o/R_i=2) was about 2.97m, while the horizontal section was about 4.12m in length. The conveying pipe was made of transparent polyvinyl chloride (PVC) material and had a wall thickness of 5mm. The entire configuration was held in position using metal castings and various pipe segments joined by connectors. Two types of particles, polyvinyl chloride (PVC) and polypropylene (PP) granules, were used throughout the experiments.

Based on the type of feeder, rotary valve can be classified as the following three types: (1) drop-through rotary valve, (2) side-entry rotary valve, and (3) blow-through rotary valve. The blow-through rotary valve used in this study is commonly seen in industrial-scale pneumatic conveying systems. This style of rotary valve has two ports on the sides near the bottom. The conveying line connects directly to the valve, with the air stream flowing through the rotor pockets. Figure 2.5 shows the schematic diagram of the rotary valve. The rotary valve has 8 pockets with a clearance of 1mm. The speed of rotary valve was fixed at 25rpm ($5\pi/6s^{-1}$). The time taken for one pocket to pass through the inlet orifice (40mm ID) could be calculated from the rolling speed and the sum of the total angular displacement of the pocket ($\pi/4$) and the orifice size

(π/8). This gives a time interval of 0.45s. The average weight of solid input to each pocket could also be calculated by multiplying the solid flow rate by 0.45s. The featured capacity of one pocket is 1.05L and the pocket filling percentage is between 1.00% and 1.46%.

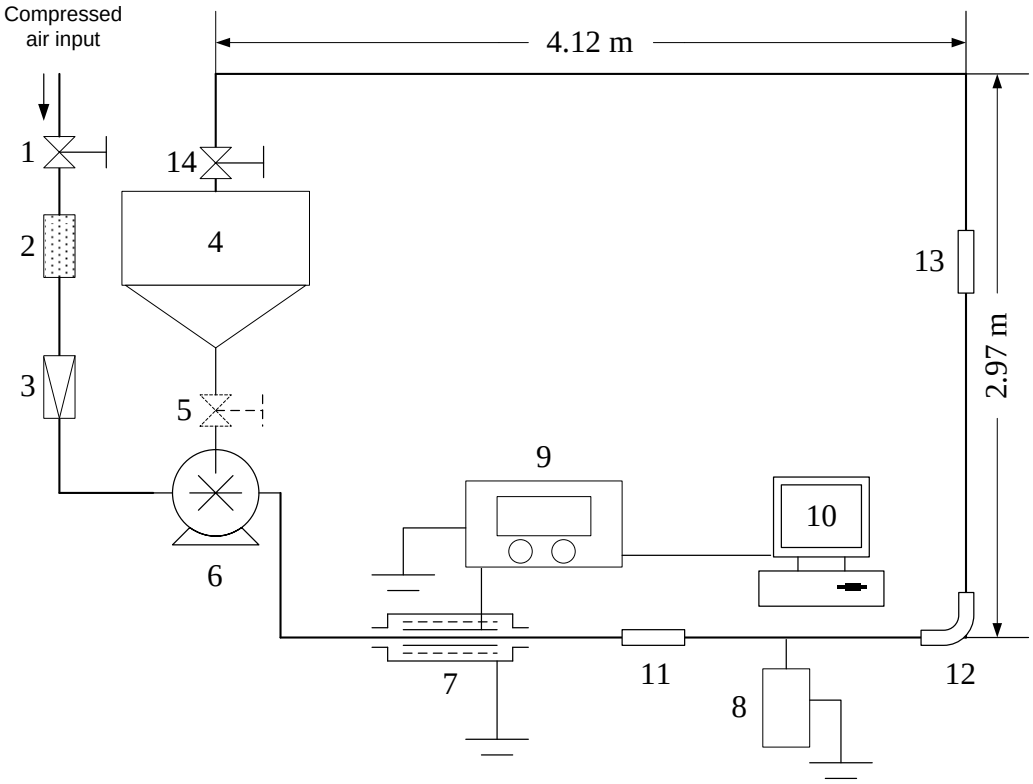

Figure 2.4 Schematic of the pneumatic conveying facility: 1. Air control valve; 2. Dryer (silica gel); 3. Rotameter; 4. Hopper; 5 Solids feed valve (Optional); 6. Rotary valve feeder (Figure 2.5); 7. Induced current measurement; 8. Faraday cage; 9. Electrometer; 10. Computer; 11. Horizontal abrasion film; 12. Abrasion film in bend; 13. Vertical abrasion film; 14. Control Valve.

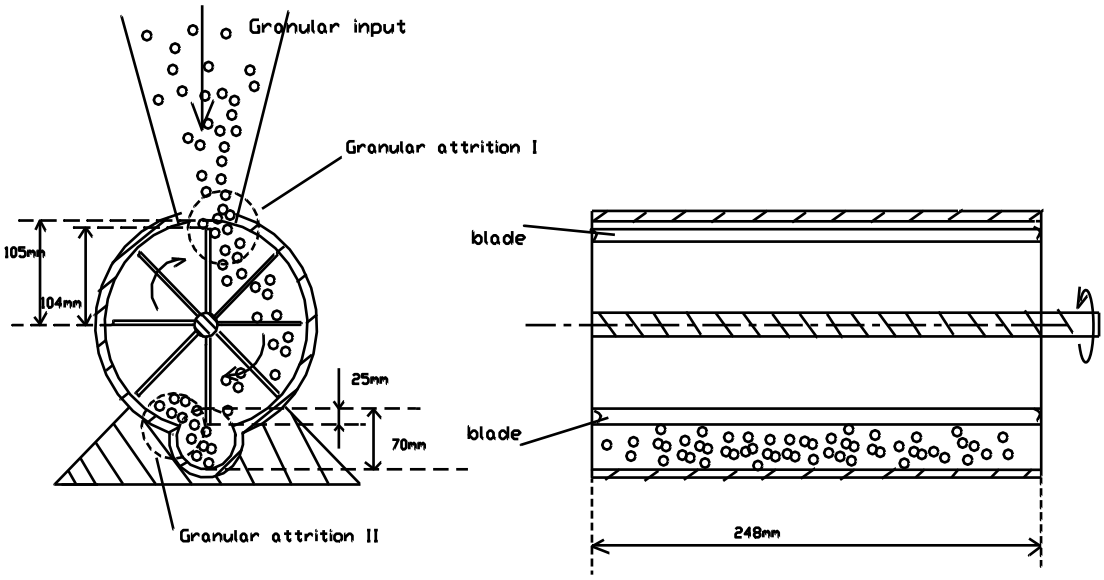

(a) (b)

Figure 2.5 Schematic diagram of rotary valve: (a) Front view; (b) Side view.

Table 2.3 Experimental conditions for Chapter 5.

Temperature (℃)	28~30	
Relative humidity (RH) in systems	5%	
Air pressure (kPa)	500	
Air flow rate (L/min)	1600	
Air superficial velocity (m/s)	21.2	
Solids feed valve	75% opening/ 100% opening/ flood-fed	
Roll speed of rotary valve (rpm)	25	
Pipe material	Polyvinyl Chloride (PVC)	
Pipe inner diameter (ID) (mm)	40.0	
Pipe thickness (mm)	5.0	
Particles conveying style	Circulation	
Particle material	Polyvinyl Chloride (PVC)	Polypropylene (PP)
Particle initial size range	3.5mm~4.2mm	2.8mm~3.35mm
Particle shape	Cylinder	Ellipsoid
Particle density (g/cm^3)	1.4	1.1
Hardness	R113	R90
Heat deflection temperature at 1.8 MPa(℃)	67	80
Sample mass (g)	745	939

2.1.5 Pneumatic conveying system for Chapter 6

In this section, the experimental facility modified from the previous study (Sections 2.1.3 and 2.1.4) was used to carry out the measurements as shown in Figure 2.6. The experimental conditions are listed in Table 2.4. Air from the compressor is metered and sent to the rotary air lock feeder (General Resource Corp., Hopkins, Minnesota, US), where it entrains the polypropylene (PP) particles. The test section consists of two horizontal pipes, which are connected by an inclined/vertical pipe. The conveying loop is made of pipes with an inner diameter of 40mm and the thickness of 5mm. Visual observations of the various solid flow patterns that arise during the experiments are facilitated through the use of transparent polyvinyl chloride (PVC) pipes.

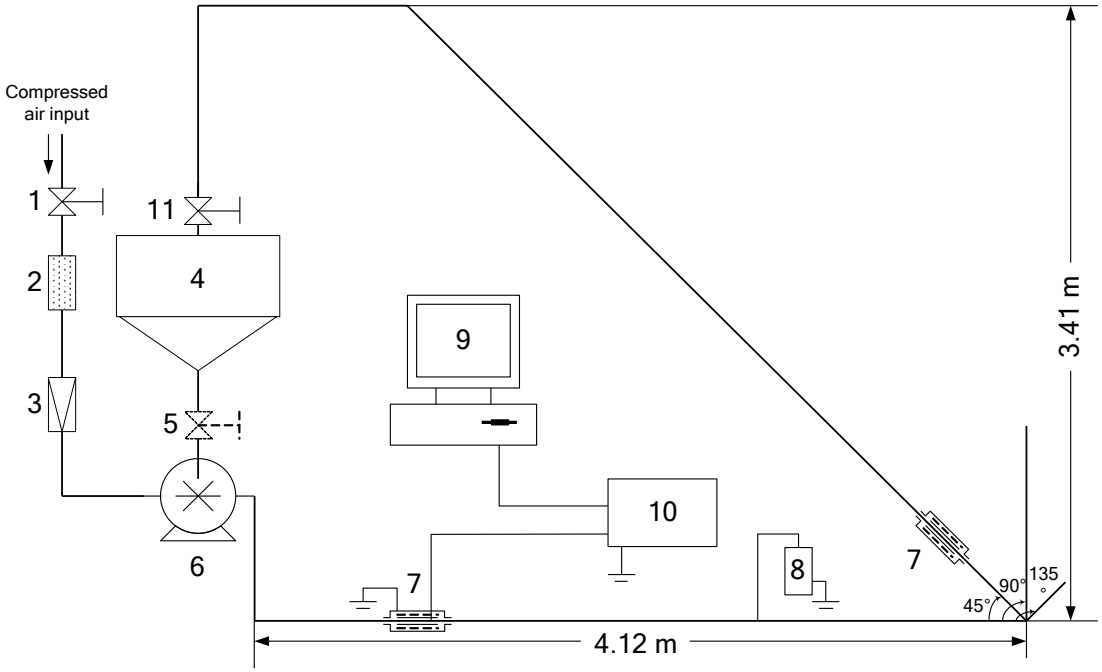

Figure 2.6 Schematic of the pneumatic conveying experiment facility: 1. Air control valve; 2.Dryer; 3.Rotameter; 4. Hopper; 5. Solids feed valve; 6. Rotary valve feeder; 7. Induced current measurement; 8. Faraday cage; 9. Computer; 10. Electrometer; 11. Feed control valve.

Table 2.4 Experimental conditions for Chapter 6.

Temperature (℃)	28~30	
Relative humidity (RH) in systems	5%	
Air pressure (kPa)	500	
Air flow rate (L/min)	1600	
Air superficial velocity (m/s)	21.2	
Solids feed valve	75% opening/ flood-fed	
Roll speed of rotary valve (rpm)	25	
Pipe material	Polyvinyl Chloride (PVC)	
Pipe inner diameter (ID) (mm)	40.0	
Pipe thickness (mm)	5.0	
Particles conveying style	Circulation	
Particle material	Polyvinyl Chloride (PVC)	Polypropylene (PP)
Particle initial size range	3.5mm~4.2mm	2.8mm~3.35mm
Particle density (g/cm^3)	1.4	1.1
Sample mass (g)	745	939

2.2 Electrostatic measurements

2.2.1 Induced current measurement

During the pneumatic conveying process, contact between the solid particles and the pipe wall generates electrostatic charges. The current induced along the surface of the pipe wall as a result of these charges was measured as a function of time. This was done by wrapping an aluminum foil sheet tightly over the outer wall of the PVC pipe. A coaxial line (connected to the high input end of an electrometer) was connected to the outer surface of the aluminum foil sheet. A polymer film was then wrapped tightly over the aluminum foil sheet to separate this sheet from another aluminum foil sheet whose external surface was connected to the low input end of the coaxial cable. Subsequently, this external layer of aluminum foil sheet was grounded and used as an extra electrical shield. The induced current through the pipe wall was measured as a function of time through digital readings from the electrometer and stored in a computer at intervals of 0.5s.

2.2.2 Particle charge density

The charge on the particle was measured by a Faraday cage. Charged particles were placed into a metal enclosure that was isolated electrically and the amount of charges present was then measured. The mass of particles collected in the cage was measured using an electronic balance to an accuracy of 10^{-4}g and the mass-to-charge ratio of the particles was then calculated.

2.2.3 Equivalent current of charged granular flow

Additionally, a Modular Parametric Current Transformer (MPCT, Bergoz, France) which allows for current measurement with a resolution of 1μA using a noninvasive DC beam was also used to measure the equivalent current of charged particles flow.

2.3 Electrical Capacitance Tomography (ECT) for Chapter 4

ECT is a non-invasive technique for measuring and displaying the concentration distribution of a mixture of two dielectric fluids. In this experiment, two sets of 12-electrode (10cm long) ECT sensors (labeled as 10 and 11 in Figure 2.3) were arranged on the inclined pipe at locations 1.45m and 2.18m from a bend connecting this inclined riser to a horizontal duct at the bottom. A data acquisition module (DAM) (Process Tomography, Wilmslow, Cheshire, UK) was connected to the ECT sensors to gather capacitance data. The ECT was sampled at 40Hz, corresponding to a time period of 0.025s for each frame. The resolution of each frame was 1024 (32×32) pixels. The ECT system was calibrated for the lower (air with 0 as reference value) and upper (solids with 1 as reference value) permittivity bounds.

2.4 Particle Image Velocimetry (PIV) for Chapter 4

PIV is generally employed to exhibit the magnitudes and vectors of particle velocities and afford exact values of velocities. Measurements using a PowerView 2D PIV system (TSI, Shoreview, MN, USA) were conducted at the inclined pipe region 1.83m downstream from the bend. The laser light sheet generated by the Laser Pulse^{TM} Solo Mini Dual Nd: YAG laser was introduced from the top of the wall/sidewall to lighten

the granules at the center plane (labeled as 12 in Figure 2.3). Images of the granules were captured by a PowerView^{TM} 4M (2K×2K) camera in the direction perpendicular to the lightsheet and transmitted to the computer for processing. The cross-correlation yields the distance traveled by the granules in a small time interval (50μs~58000μs) from the first snapshot to the second and the velocity distribution of granules in the plane can be determined by dividing by the time interval. In this study, the variation of velocity in the axial direction of the 45°inclined pipe was measured.

2.5 Physical properties of particles for Chapter 5

In order to investigate the attrition characteristics of particles, it was deemed necessary to study their physical properties. In the present section, particle size and shape, load-strain characteristics, flow-time and internal friction angle of PVC and PP samples were measured.

2.5.1 Particle size and shape

Particle size and shape were basic properties for particulate materials used in this investigation. They were measured simultaneously using a particle size/shape analyzer (Analytical Technologies Pte Ltd, Singapore).

2.5.2 Single particle compression test

Single particle compression test was performed to measure the relationship between load and strain of a single particle. Such data is important to understand the attrition process in a rotary valve. A single particle was put on the lower support of the

Compression Tester (AGS-10kNG, Shimadzu, Kyoto, Japan), and a continuous load was applied until permanent deformation of the particle was achieved. Load and deformation data were recorded during the process.

2.5.3 Granulate test

Flowability is another important parameter for characterizing the physical property of particles. It is supposed to be related with attriton process in the whole pneumatic conveying system. It can be measured by two methods: granulate test and shear strength test. The Granulate Tester (GT/GTB, ERWEKA, Heusenstamm, Germany) was used to determine the flowability of powders and granules as defined by EP (European Pharmacopoeia) by measuring the flow time of a sample of such material. In a typical test procedure, a known mass of particles was allowed to flow out of a hopper with a 25mm-diameter nozzle into a collecting vessel in the Granulate Tester and the total time taken was recorded.

2.5.4 Shear strength test

The Consolidation Isotropic Undrained (CIU) test was used to characterize shear strength. The internal friction angle of polymer particles was measured using a Triaxial Tester (Wykeham Farrance, Slough, England). This parameter determines the friction between particles and can be used to explain the flowability of particles as mentioned above. Each test was applied to 3 specimens, consisting of particles and water in the form of right cylinders of nominal diameter, 50mm, and height, approximately equal to twice the diameter. The CIU experiment procedure consisted of four major steps: Firstly, the frozen specimen was prepared; secondly, the specimen

in the triaxial apparatus was set up; thirdly, the specimen was allowed to thaw, saturate and consolidate; lastly, the specimen was compressed and the experiment data were read from a computer.

2.6 Particle size variation due to attrition for Chapter 5

The procedure for determining particle size distribution following granular attrition was as follows. Firstly, a sample of particles was allowed to undergo attrition for a given time either in a rotary valve feeder or pneumatic conveying system. Secondly, a weight–size analysis on representative samples of the attrited particles was then performed by sieving. Thirdly, the procedure was then repeated for other attrition times to track changes in particle size distribution with respect to attrition time. In this experiment, the sieves were made of metal and grounded using electrical wires. This arrangement ensured that charge generated during shifting would be removed and the electrostatic problem would hardly lead to the inaccuracy of particle size measurements.

2.7 Solid flow rate in pneumatic conveying system for Chapter 5

The present study makes use of electrostatic characteristics of particle to measure the solid flow rate. The solid flow rate was obtained by measuring the induced current with valve 14 shut (Figure 2.4) so as to allow particles to be conveyed once through the system only. The rotary valve is connected to the atmosphere, therefore, gas can vent from the system. The particles were accumulated in upper pipe (this pipe segment has enough space to store the particles) of the valve 14 until the experiment

was finished, then the particles were released to the hopper 4. If particles did not flow through the pipe, there was no charge generated, and the output signal of the induced current was close to nil. On the other hand, if particles passed through the pipe, induced current was detected with a non-zero value. Therefore, the time interval for one circulation could be obtained easily by observing the signal of induced current; accordingly, solid flow rate was calculated as the ratio of total mass of granules to time in one circulation. The validity of such a method had been proven using a similar approach (Mathur and Klinzing, 1984) to generate solid flow rate readings comparable to those collected from load cells.

2.8 Pipe wall abrasion for Chapter 5

The friction and collisions between particles and pipe wall would also lead to pipe abrasion in a conveying system. The material of all pipes used in the present pneumatic conveying system was polyvinyl chloride (PVC) except at three test sections (referred to as the bend, vertical and horizontal sections and shown in Figure 2.4) where acrylate copolymer film was rolled into a cylinder and attached to the inner surface of the pipe wall. The study of pipe wall abrasion was based on a polymer film not PVC pipe, because it is difficult to sampling the PVC pipe wall for its hardness. Although these are two different materials, the results are comparable. The aim is to investigate the effect of different particles (intact vs attrited and PP vs PVC) on pipe wall abrasion not the effect of pipe materials on wall abrasion. Furthermore, the thickness of polymer film was only 0.12mm and the length of film was up to 210mm, and the film was attached to the inner surface of pipe wall tightly, thus can furthest reduce the influence of the film on particle flow behavior. Four types

of particles (intact/attrited PVC and intact/attrited PP samples) were conveyed separately through the system at an airflow rate of 1600 L/min for about 3h. In the present work, the term “intact particle” refers to fresh/unused material. The extent of abrasion of the polymer film resulting from frictional forces between moving particles and the film was quantified by measurements of the mass of the film before and after each experiment.

2.9 Sensitivity of ECT measurements due to the electrostatic charge effect for Chapter 6

Pipe bends in the conveying system made of non-conductive material and with different angles of inclination was used for results presented in this section. It is known that charges are more easily generated on the wall of the bend due to more frequent particle-wall impacts in small curvatures. The resulting high potential difference due to the strong electric field created would then tend to introduce errors to capacitance measurements on the interior of the conveying pipe. In the first stage of this work, an estimate of the orders of magnitude of such errors can be obtained by artificially creating a well-controlled environment within a section of pneumatic conveying system and comparing ECT measurements both in the presence and absence of electrostatic charge effects. The experimental methodology is summarized as follows. Firstly, ECT was used to obtain the particle concentration distribution of a collection of stationary particles in a pipe segment in the absence of electrostatic charges. Secondly, electrostatic charges were induced artificially in a separate system by allowing particles to flow about a pipe bend. Thirdly, induced charges were transferred from the second step to the pipe segment with ECT sensors used in the

first step and make a second measurement in the presence of these electrostatic charge effects. Finally, ECT measurements obtained in the presence of electrostatic charges (step three) was compared with those obtained from step one.

Schematically, the length of pipe segment (ID=0.50m) is 0.69m and ECT sensor (length=0.23m) is arranged 0.07m away from the left side of pipe segment. In this way, the quantitative effects of electrostatic charges on ECT measurements can be obtained. In this experiment, another two pipe segments (horizontal and vertical section, both with the distances of 0.26m away from the bend) were used (Figure 2.7 (a)). Furthermore, different angles of inclination: 90 º(Figure 2.7 (a)), 135 º(Figure 2.7 (b)) and 45 º(Figure 2.7 (c)) at the ECT measurement section were used. The point on the pipe segment in which electrostatic charge was introduced is placed 0.25m away from the left-hand side of pipe segment. Two test cases were performed where charge is introduced into the top and bottom of the pipe respectively, as shown in Figure 2.8. A data acquisition module (DAM) (Process Tomography, Wilmslow, Cheshire, UK) was connected to the ECT sensor, and capacitance data were collected for the stationary particles through the conveying pipes.

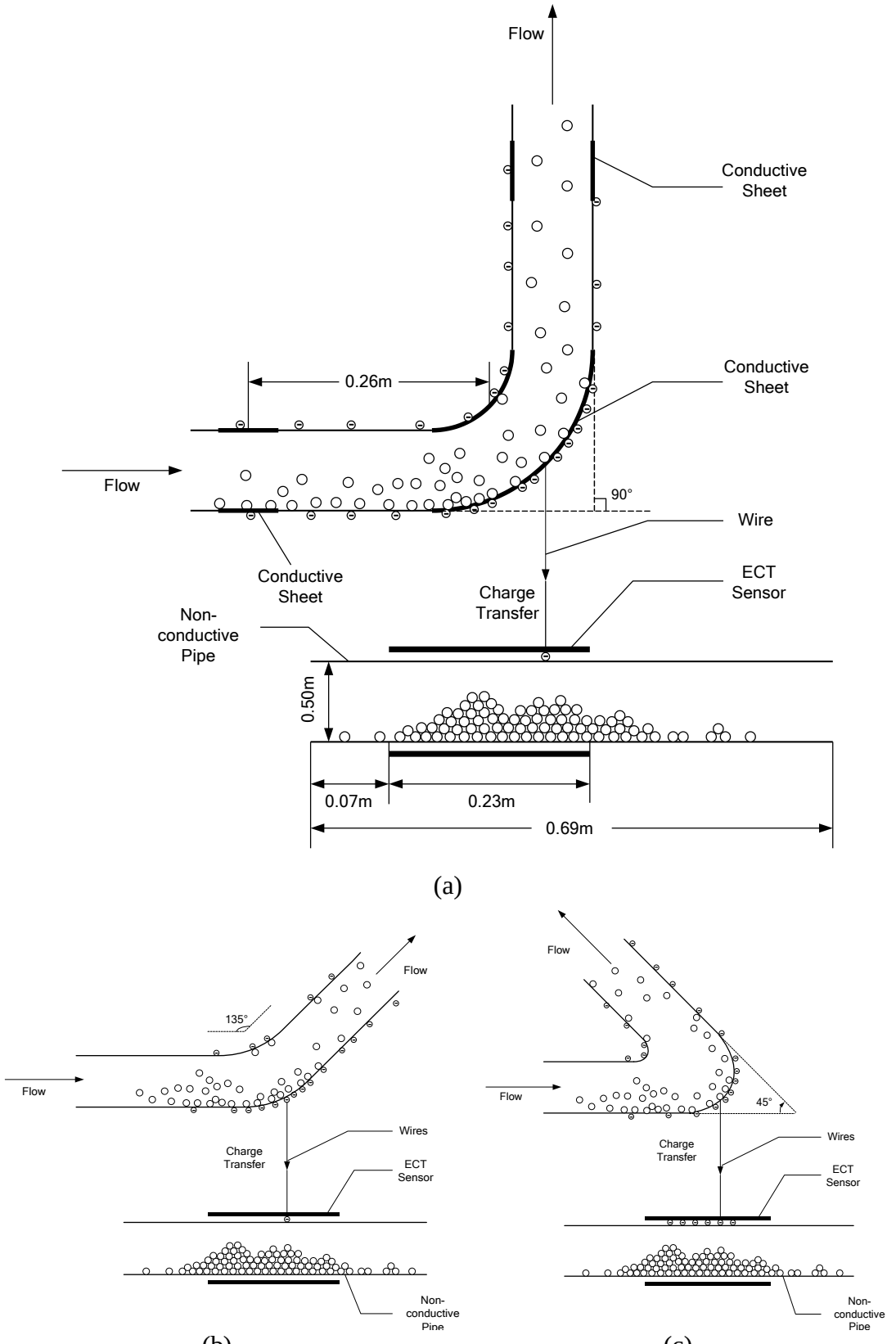

Figure 2.7 Schematic diagram of charges transferred from conveying pipe to ECT measuring system (nonconductive material): (a) 90 ºbend; (b) 135 ºbend; (c) 45 ºbend.

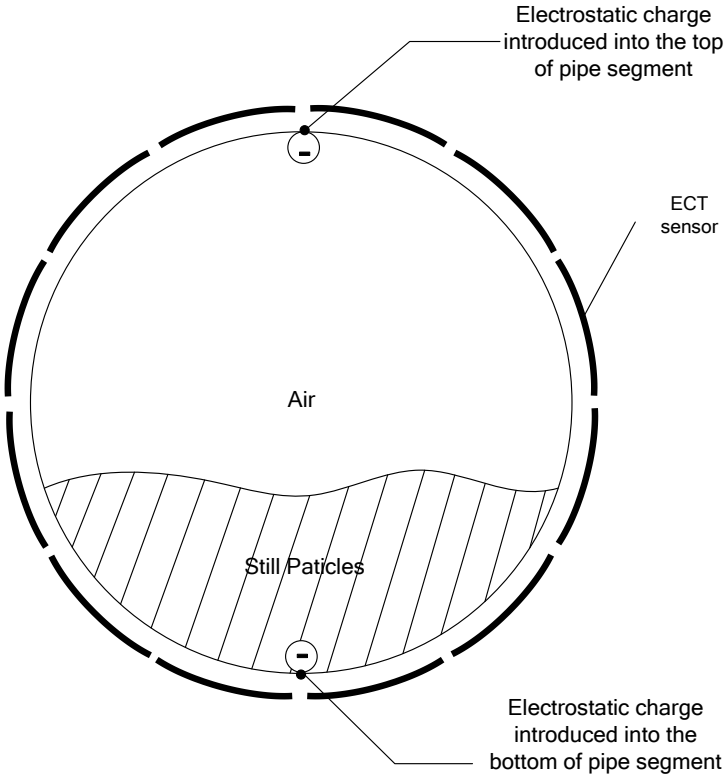

Figure 2.8 Cross section of pipe segment with ECT sensor

Chapter 3. Electrostatics of granular flow on vertical and horizontal pneumatic conveying pipe

Pneumatic conveying systems are widely used in the energy, chemical, pharmaceutical and material processing industries for the transportation of granular material. Solid particulate in such systems have a natural tendency to acquire electrostatic charges due to collision with surface of a different material type (Masuda et al. 1976). The accumulation of charges on system components may pose possible electrical hazard and lead to compromises in the safety standards of such operations. As such, a comprehensive understanding of the effects of electrostatics on the flow of granular material in a pneumatic conveying system is required. This chapter aims to study the electrostatics of the granular flow in pneumatic conveying system and reports on three flow patterns which have been named disperse, half-ring and ring flow. These are believed to arise according to the relative importance between the electrostatic forces and the usual hydrodynamics forces present between the gas and solid phases. The results and analysis are focused on the electrostatics of the granular flows at vertical pipe according to measure three electrostatic parameters: induced current on pipe wall, particle charge density and equivalent current of charged granular flow. Electrostatics of the granular flow at horizontal pipe for three flow patterns observed in vertical conveying is compared to that at the vertical pipe. Furthermore, the factors that affect the electrostatics of the granular flow, such as pipe material, relative humidity of conveying gas, and the mixture of anti-static agent (Larostat-519) are analyzed respectively.

As mentioned above, the solid flow patterns observed in the vertical section of the pneumatic conveying system can be classified into the disperse flow, half-ring flow and ring flow regimes. The airflow rates and superficial velocities at which each flow pattern occurs and the corresponding solid flow rates are shown in Table 3.1.

3.1 Electrostatics of granular flow in the vertical pipe

3.1.1 Granular flow patterns

3.1.1.1 Disperse flow pattern

When the airflow rate exceeds 1200L/min, particles are transported at high velocities up the vertical pipe and do not concentrate on the pipe wall (Figure 3.1 (a)). However, after a long time (about 2h for the case of 1200L/min), some particles were found to concentrate on the vertical pipe wall from time to time in the form of clusters (Figure 3.1 (b, c)). Due to the strong airflow, the cluster of particles seemed fairly unstable and exhibited much fluctuation in their vertical positions along the pipe. The clusters were located fairly high up in the pipe and traveled along a curved path by the pipe wall (Figure 3.1 (b)). These clusters appeared and disappeared intermittently in an unpredictable manner.

3.1.1.2 Half-ring flow pattern

When airflow rate is about 900~1150L/min, particles tend to move along curvilinear tracks in the vertical pipe (Figure 3.2 (a)). However, after about half an hour of cycling through the pneumatic conveying system, particles were observed to cluster on the side of the vertical pipe wall distant from the position of the lower horizontal pipe to form a half-annular ring structure (Figure 3.2 (b, c)). This structure was

located at a height of about 30cm above the bottom elbow.

3.1.1.3 Ring flow pattern

When the airflow rate was less than 850L/min, the effects of gravitational and electrostatic forces became more significant. Initially, particles slid upwards in contact with the surface of the pipe (Figure 3.3 (a)). After about 15min, the particles were observed to travel in a spiral fashion up the vertical pipe along the pipe wall. This resulted in a ring or annulus structure with high particle concentrations adjacent to the wall and a relatively empty core region (Figure 3.3 (b, c)). The structure was similarly unstable and fluctuated in its vertical position along the pipe.

At an air flowrate of 880L/min, which was intermediate between those giving rise to the half-ring and ring flow regimes, the observed flow pattern alternated between the two characteristic half-ring and ring structures. This might be indicative of an unstable or oscillatory transition between the two flow regimes at this particular air flow rate used.

Table 3.1 Three characteristic patterns developed in a vertical conveying pipe.

Flow pattern	Air flowrate (L/min)	Air superficial velocity (m/s)	Solid flowrate (g/s)
Disperse flow	1600	21.2	44.4 ±4.0
Half-ring flow	1000	13.3	17.4 ±3.0
Ring flow	860	11.4	10.2 ±2.0

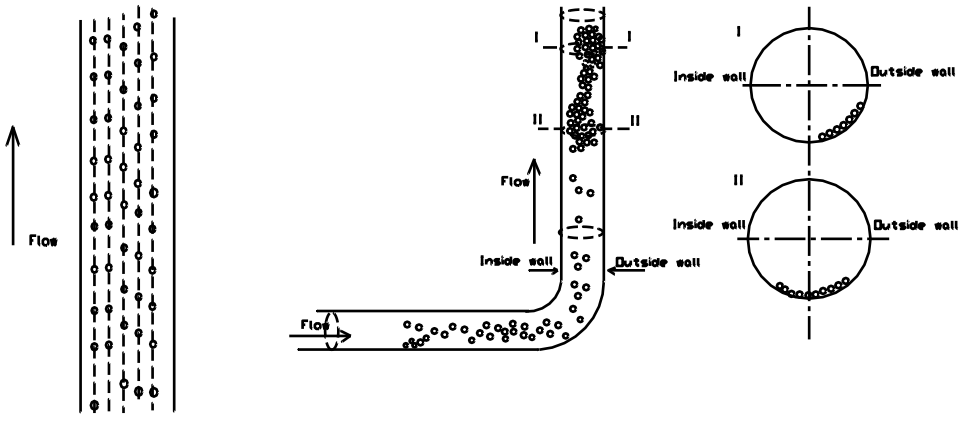

(a) (b)

(c)

Figure 3.1 Typical pattern of particles disperse flow (air flowrate>1200L/min, air superficial velocity>15.9m/s): (a) At the beginning; (b) About 2h later for the case of 1200L/min; (c) Snapshot at a pipe section.

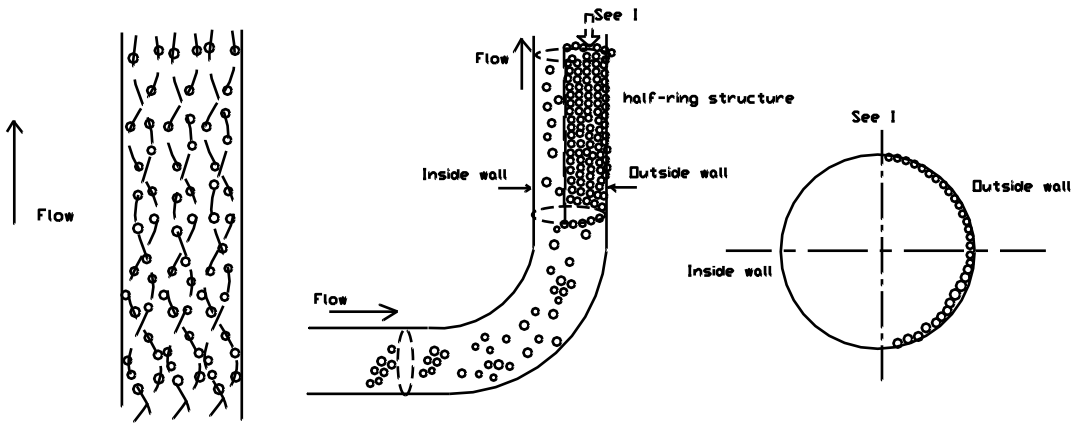

(a) (b)

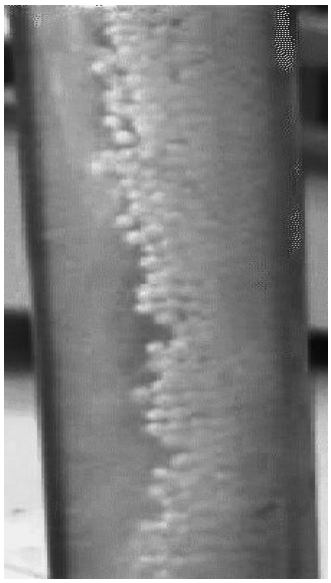

(c)

Figure 3.2 Typical pattern of particles half-ring flow (air flowrate 900~1150L/min, air superficial velocity 11.9~15.3m/s): (a) At the beginning; (b) About 30min later for the case of 900L/min; (c) Snapshot at a pipe section.

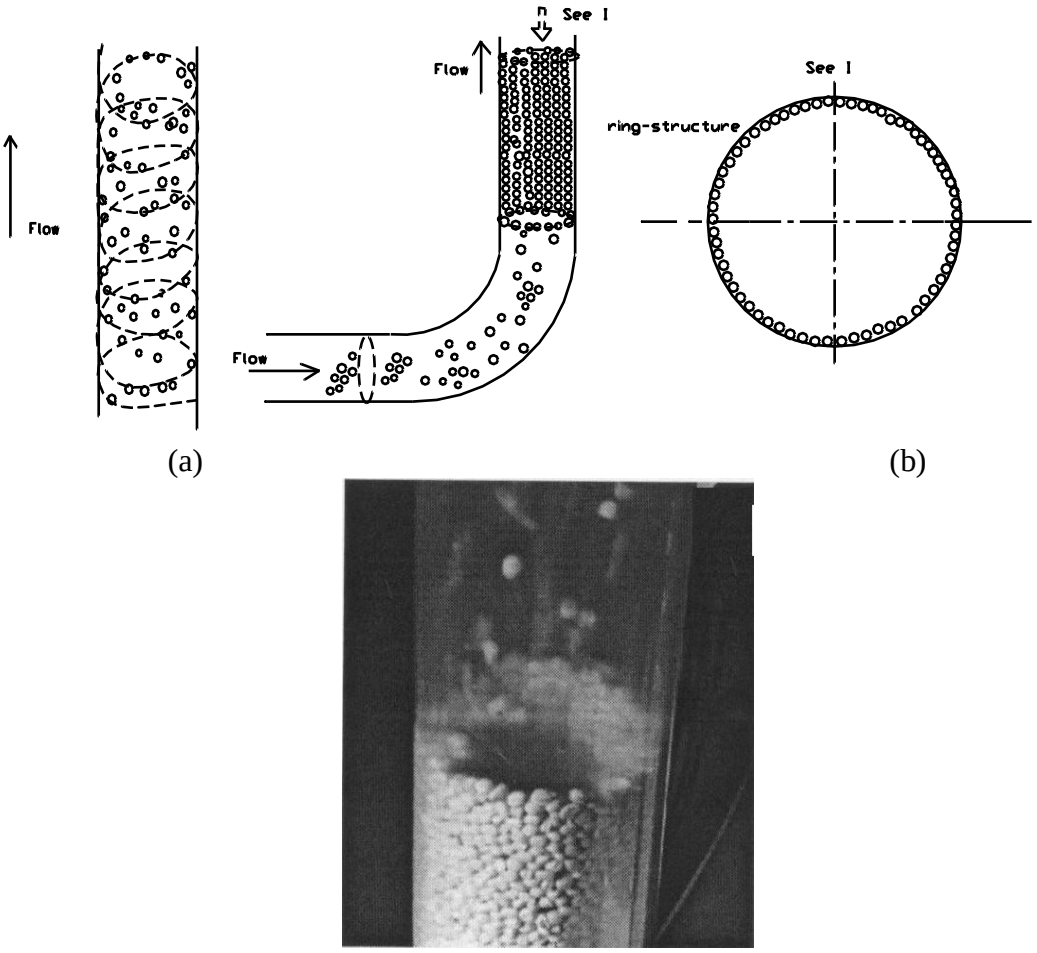

(a) (b)

(c)

Figure 3.3 Typical pattern of particles ring flow (air flowrate<850L/min, air superficial velocity<11.3m/s): (a) At the beginning; (b) About 15min later for the case of 850L/min; (c) Snapshot at a pipe section.

3.1.2 Induced current

In the experiments conducted, attempts have been made to analyze the induced current for the three types of flow described above (Figure 3.1~3.3). The induced current detected using the electrometer at the vertical pipe is illustrated in Figure 3.4. It can be seen that the induced current fluctuates with time and may be negative or positive in value.

It is known that particle-wall contacts in a conveying system may lead to charge generation both on the surface of the particles and on the pipe wall. On the basis of previous experiments (Zhu et al. 2004b) using PP particles and PVC pipes, it can be deduced that positive charges are generated on the PP particle surface while equal amounts of negative charges are accumulated on the PVC pipe wall. At the detection segment, if particles slide on the pipe wall as in half-ring or ring flow, charges on the pipe wall are partly neutralized by those on the surface of particles and leads to a lower induced current. On the other hand, when there are no particles sliding on the pipe wall of the detection segment, charges on the pipe wall is retained, leading to a higher induced current. It can be said that the induced current measured by the electrometer is a composite value resulting from a balance between the electrostatic charge on the particle surface and pipe wall. The absolute value of the induced current indicates the electrostatic charge storing capacity of the granular flow.

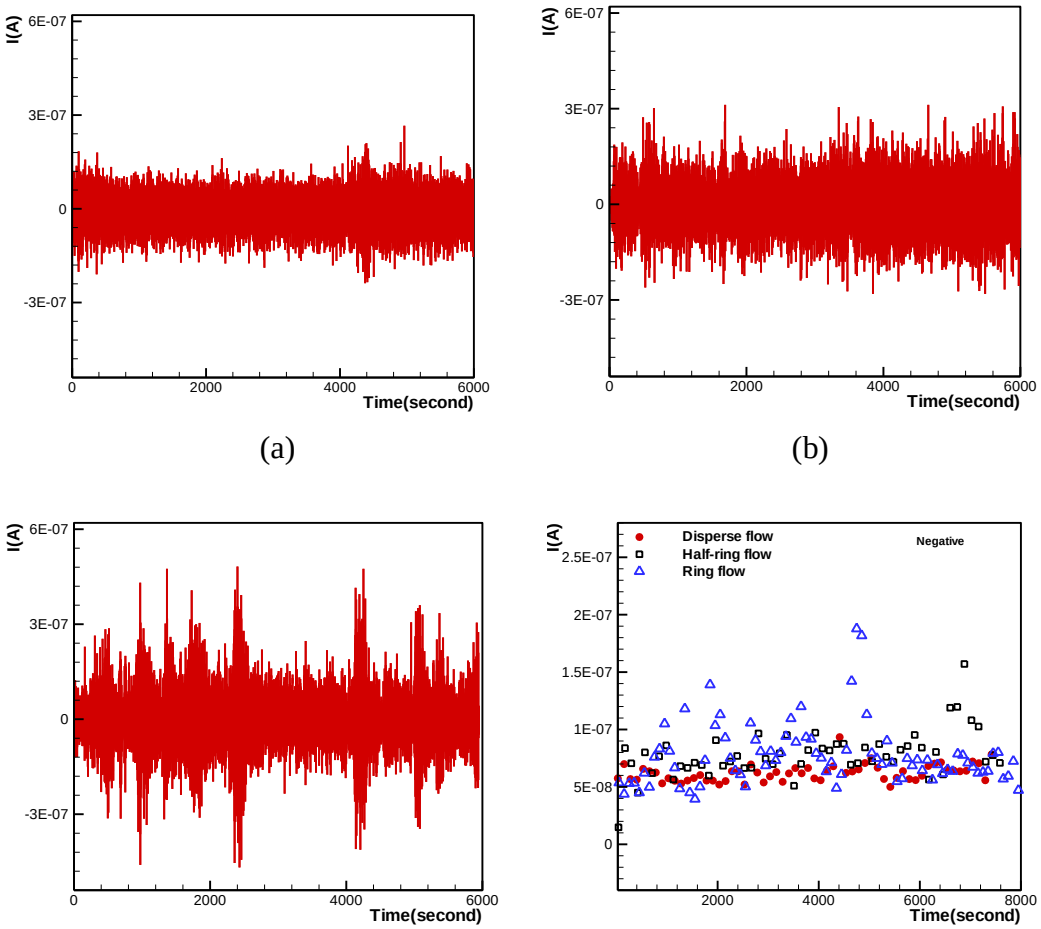

Figure 3.4 Induced current acquired at the vertical pipe: (a) Disperse flow (air flowrate 1600L/min, air superficial velocity 21.2m/s); (b) Half-ring flow (air flowrate 1000L/min, air superficial velocity 13.3m/s); (c) Ring flow (air flowrate 860L/min, air superficial velocity 11.4m/s); (d) Comparison of the current value (negative) for the three flows.

Figure 3.4 shows that the magnitude of the induced current increases with decreasing flow rate. Figure 3.4 (d) shows the absolute values of the negative current sampled at a rate of $200s^{-1}$. It is evident that the absolute current value increases with decreasing flow rate, implying enhanced electrostatics.

In addition, to eliminate the fluctuation caused by negative and positive values (Figure 3.4), induced currents were integrated with respect to time according to Equation (3.1) to obtain the charge *q*:

$$q = \int_0^T I \cdot dt \tag{3.1}$$

where *I* is the induced current measured from the electrometer, *T* is the time period.

Figure 3.5 (a) shows that the charge *q* detected at the detection segment increases linearly with time up to 5000s and the rate of increase seemed constant for each of the three flow patterns. Furthermore, the magnitudes of negative currents detected were generally larger than those of positive currents, implying a net electron gain by the pipe wall (Figure 3.5 (b)).

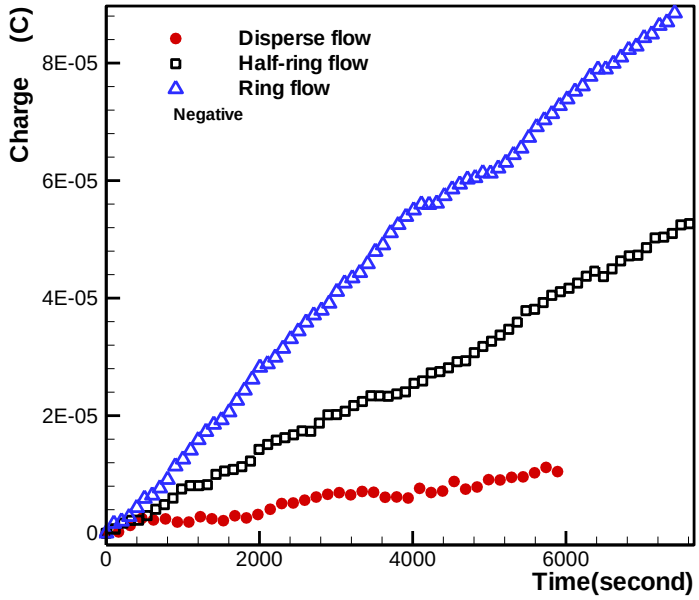

(a)

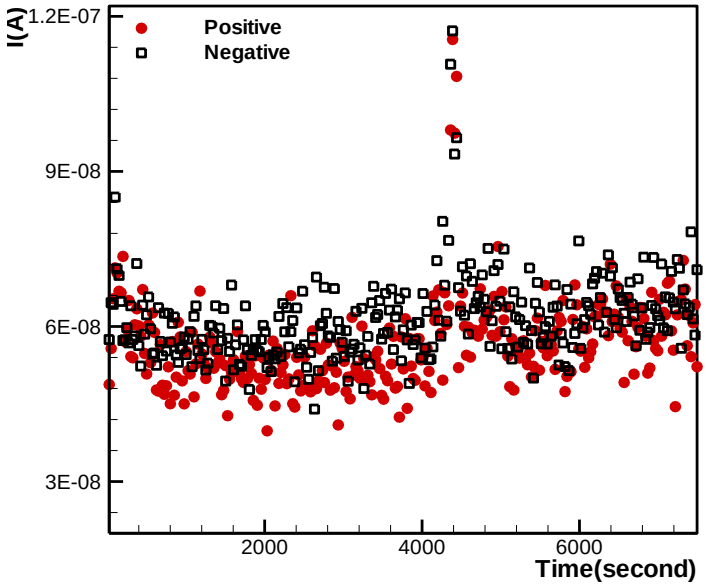

(b)

Figure 3.5 Comparison of the induced current acquired at the vertical pipe: (a) Charges obtained by integration of the currents (shown in Figure 3.4 (a~c); (b) The positive and negative values (absolute) of the induced current of the disperse flow (air flowrate 1600L/min, air superficial velocity 21.2m/s).

3.1.3 Particle charge density

The variations of the charge-to-mass ratio of particles with respect to time for the three types of flow are presented in Figure 3.6 and Tables 3.2~3.4. It can be seen that particle charge densities in the half-ring and ring flow are similar with both being larger than those in disperse flow. For all three cases, the general trend for particle charge density to increase with time does indicate possible accumulation of charges on the particle. This may eventually result in strong electrostatic interactions between the particles and the pipe wall and cause formation of the half-ring and ring structure described above.

3.1.4 Equivalent current of charged granular flow

The equivalent currents for the three flow patterns (disperse, half-ring and ring) at the vertical section of the pneumatic conveying system are presented in Figure 3.7 where each data point was obtained by time integration of 400 current readings from the MPCT over a time interval of 20s using Equation (3.1). It can be seen that the MPCT values in the half-ring and ring flows are fairly similar and larger than that in disperse flow. This is consistent with the trend observed for particle charge densities for the three flow patterns discussed above. Furthermore, Figure 3.7 also suggests that particles carry positive charge while being transported along the pipe and this agrees with the contact potential difference measurements by Zhu et al. (2004b).

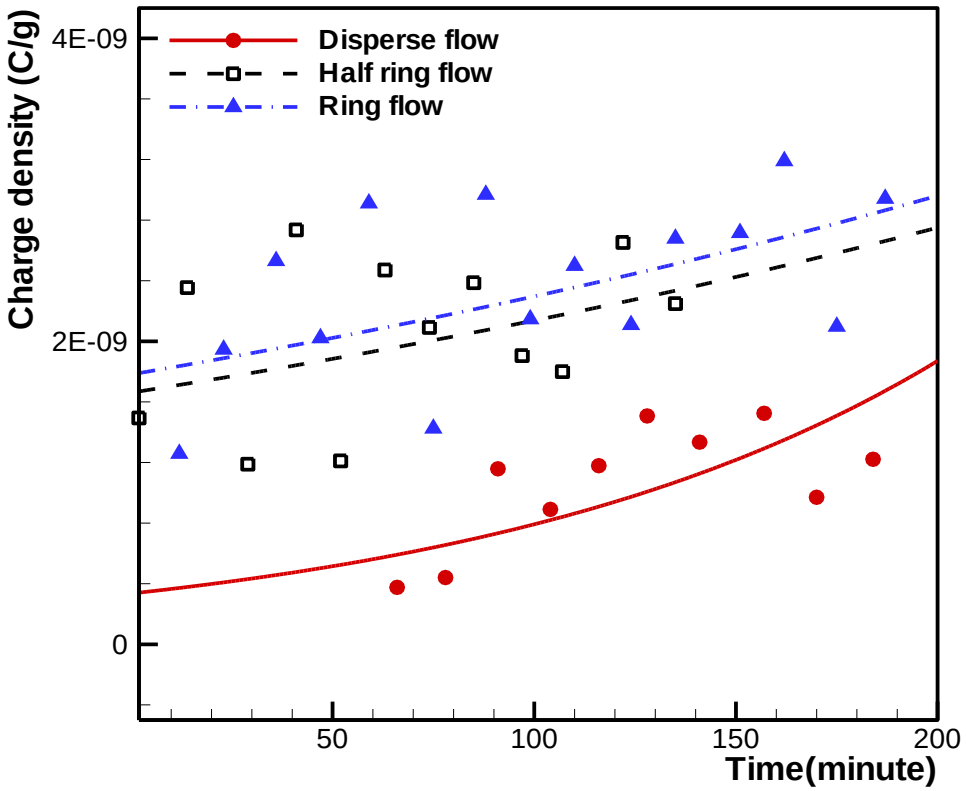

Figure 3.6 Comparison of particle charge density (using Faraday cage) for the three flows: disperse flow (air flowrate 1600L/min, air superficial velocity 21.2m/s), half-ring flow (air flowrate 1000L/min, air superficial velocity 13.3m/s), ring flow (air flowrate 860L/min, air superficial velocity 11.4m/s).

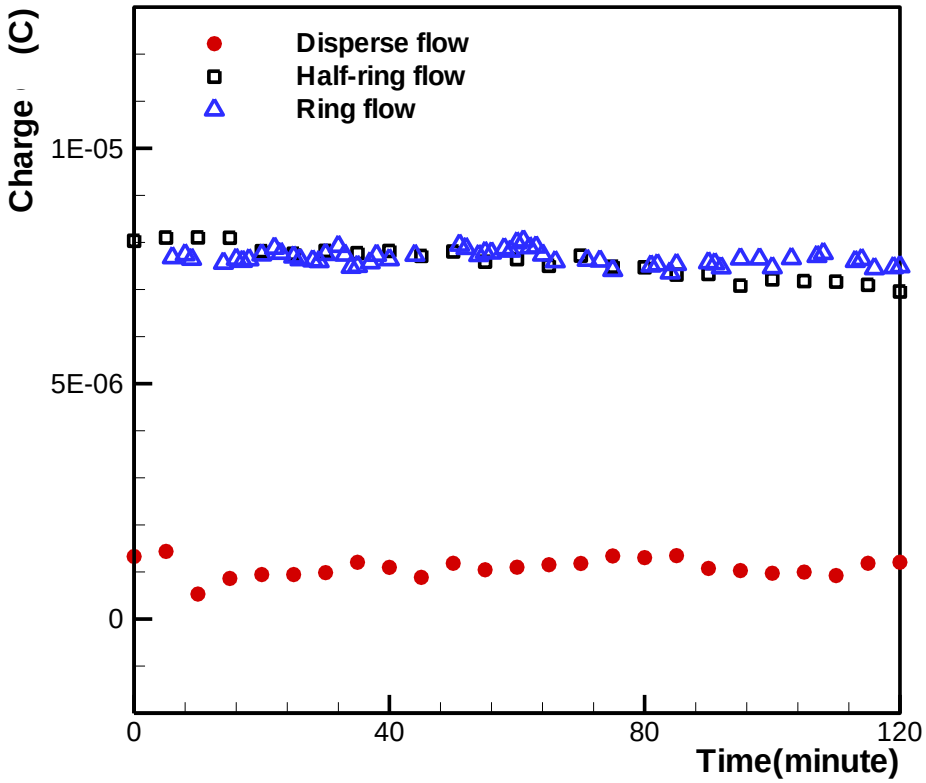

Figure 3.7 Comparison of charges obtained by integration of 400 MPCT values within a time interval of 20s acquired at the vertical pipe for the three flows: disperse flow (air flowrate 1600L/min, air superficial velocity 21.2m/s), half-ring flow (air flowrate 1000L/min, air superficial velocity 13.3m/s), ring flow (air flowrate 860L/min, air superficial velocity 11.4m/s).

3.2 Electrostatics of granular flow in the horizontal pipe

3.2.1 Granular flow pattern

The three flow patterns observed in vertical pneumatic conveying were not observed in the horizontal section of the system. However, the studies in this chapter are focused on three flow patterns observed at the vertical pipe. In order to describe conveniently, disperse, half-ring and ring flow patterns will continue to be used to name three different flow regimes observed at the horizontal pipe. At high air flowrates (1200~2000L/min), particles were seen to be transported as a dilute and homogenous solid phase dispersed in a continuous gas phase (Figure 3.8 (a)). As the flow rates (900~1150L/min) were decreased, particles started to cluster together intermittently (Figure 3.8 (b)), and as the flowrates were reduced further (around 850L/min), a fairly stable structure was formed which moved along the horizontal pipe at velocities smaller than the superficial air velocity (Figure 3.8 (c)).

3.2.2 Induced current

The induced currents for the three types of flow in the horizontal pipe segment were similarly measured using the electrometer. Figure 3.9 shows that the amplitude of fluctuations in the induced current increases with decreasing flow rate (about $\pm 9.0 \times 10^{-8}$A in disperse flow, $\pm 1.5 \times 10^{-7}$A in half-ring flow, and $\pm 2.8 \times 10^{-7}$A in ring flow). The magnitudes of the negative component of the induced current sampled at a rate of $200s^{-1}$ also increased with decreasing flow rates (Figure 3.9 (d)). This can also be deduced from variations of the total accumulated charge on the pipe wall obtained by time integration of the data presented in Figure 3.9 (a~c). Figure 3.10 shows that

the rate of charge accumulation is larger at lower airflow rates and vice versa. This implies that the total amount of charge accumulated on the pipe wall after a particular amount of time is larger in the ring and half-ring flow regimes than in the disperse flow regime.

3.3 Comparison of the electrostatics between the vertical pipe and horizontal pipes

Moreover, in our present work, particle concentration patterns, in terms of cluster, half-ring and ring structure were observed at the vertical pipe wall but were not observed at the horizontal pipe wall. In order to have an equivalent basis for comparison of the electrostatic charge generation characteristics on vertical and horizontal pipes, the experiment was carried out both in the air flowrate of 1600L/min. A comparison of the electrostatic charge effects occurring at the vertical and horizontal segment of the system shows larger amounts of charge being accumulated on the vertical pipe. This is seen in both the time-integrated data obtained from the electrometer (Figure 3.11 (a) and the MPCT (Figure 3.11 (b)). The MPCT data also show more fluctuations in vertical than horizontal conveying (Figure 3.11 (b). In addition, the absolute values of the negative component of the induced current are also larger in the vertical pipe as compared to those in the horizontal pipe (Figure 3.12). All of these characteristics seemed to point to the previously stated conclusion that electrostatic effects are much stronger in vertical pneumatic conveying than in horizontal pneumatic conveying. However, it is to be noted that the effects of the pipe bend connecting the two pipe segments have been neglected in this analysis. It is expected that particles impact against the pipe bend with high velocities and large

forces and so may cause significant charge generation after this point in the system. Suppose that the curvature of the elbow was small enough to avoid the intense impaction of particles on the pipe bend, and then particles would be conveyed smoothly in the pipe leading to less electrostatic charge generation downstream. This hypothesis will be demonstrated by the experiment of electrostatic charge influence on ECT measurement in Chapter 6. The possible contribution of this towards the stronger electrostatic effects observed in the vertical pipe segment remains the focus of a subsequent study.

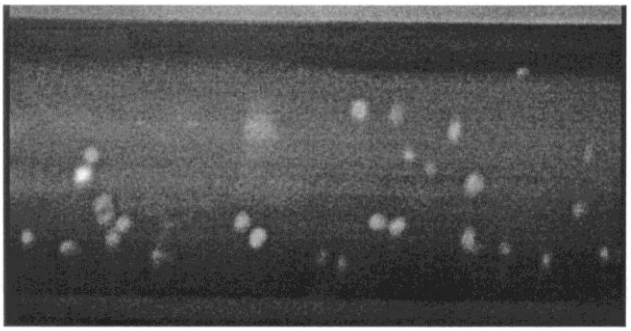

(a)

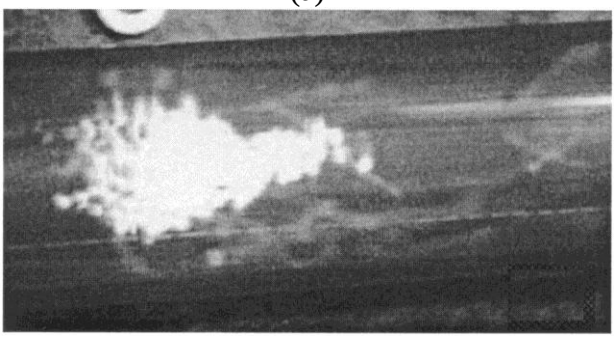

(b)

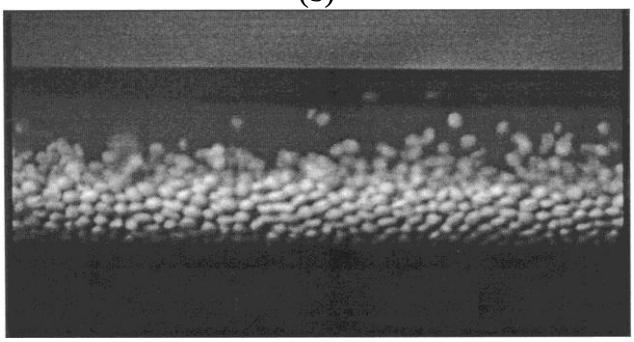

(c)

Figure 3.8 Typical pattern of particles flows at horizontal pipe: (a) Disperse flow (air flowrate 1600L/min, air superficial velocity 21.2m/s); (b) Half-ring flow (air flowrate 1000L/min, air superficial velocity 13.3m/s); (c) Ring flow (air flowrate 860L/min, air superficial velocity 11.4m/s).

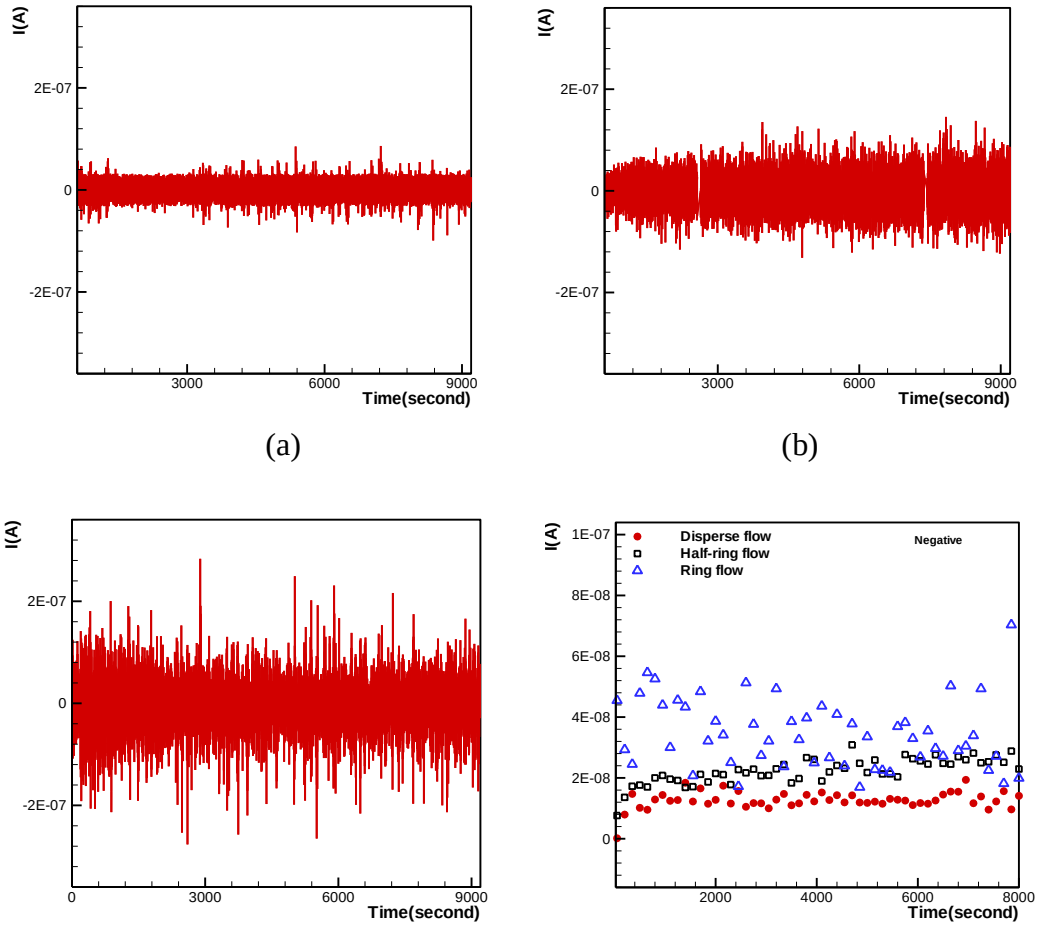

Figure 3.9 Induced current acquired at horizontal pipe: (a) Disperse flow (air flowrate 1600L/min, air superficial velocity 21.2m/s); (b) Half-ring flow (air flowrate 1000L/min, air superficial velocity 13.3m/s), (c) Ring flow (air flowrate 860L/min, air superficial velocity 11.4m/s); (d) Comparison of the induced current value (negative) for the three flows.

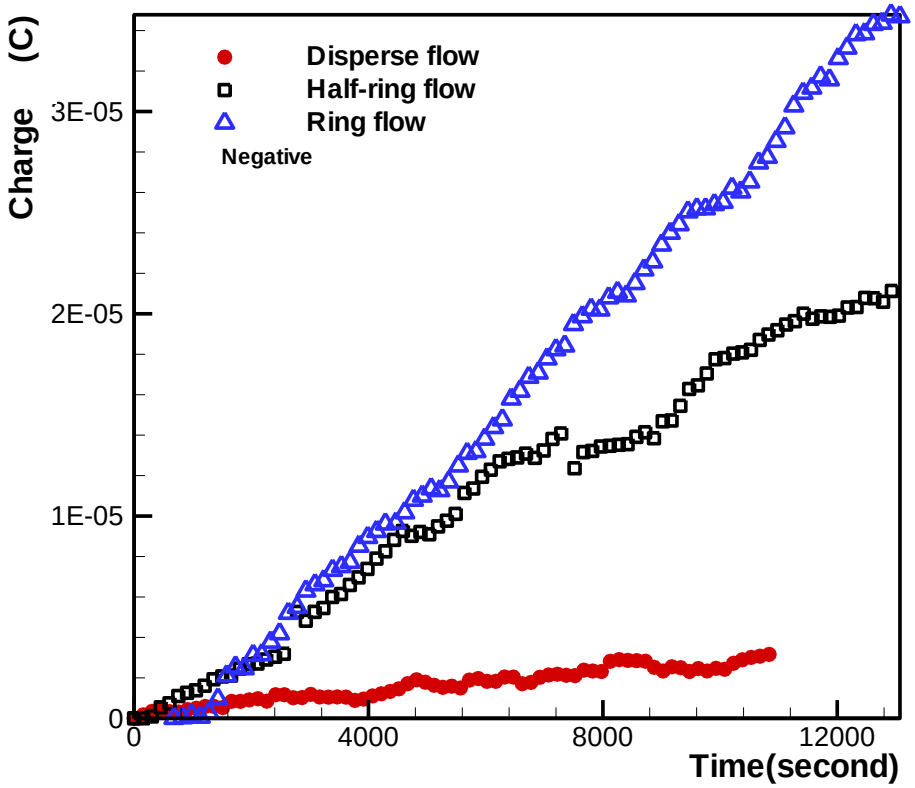

Figure 3.10 Comparison of charges obtained by integration of the induced currents acquired at horizontal pipe for the three flows (shown in Figure 3.9 (a~c)).

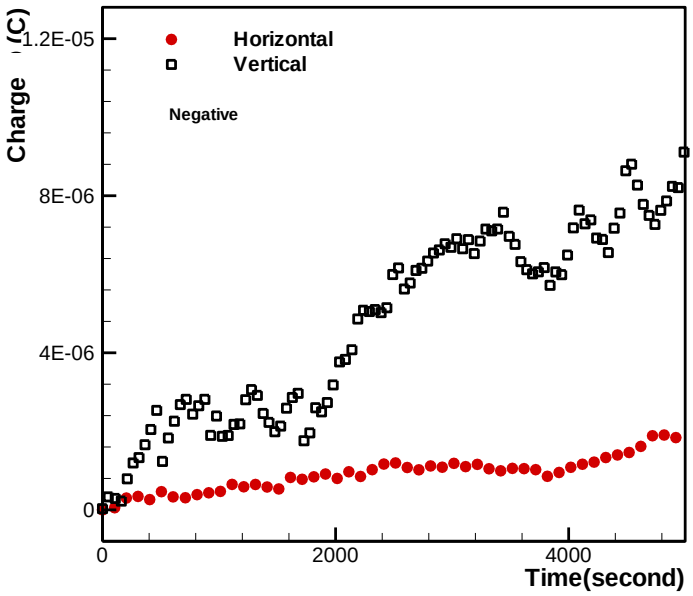

(a)

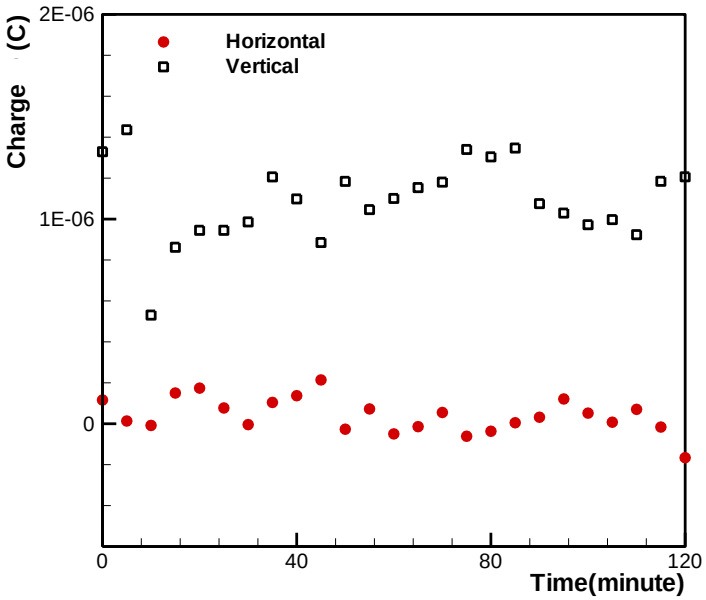

(b)

Figure 3.11 Electrostatics of vertical pipe versus horizontal pipe (disperse flow with air flowrate 1600L/min, air superficial velocity 21.2m/s): (a) Charges obtained by integration of induced currents (Figure 3.4 (a) and 3.9 (a)); (b) Charges obtained by integration of 400 MPCT values within a time interval of 20s.

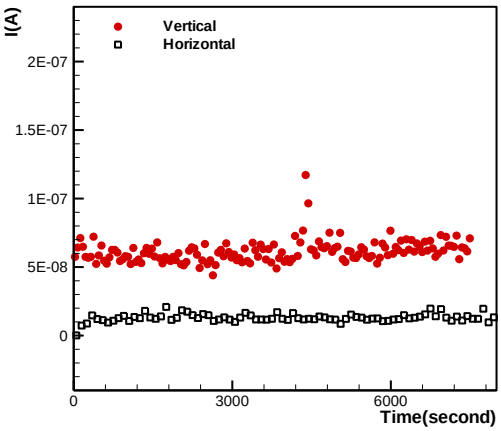

(a)

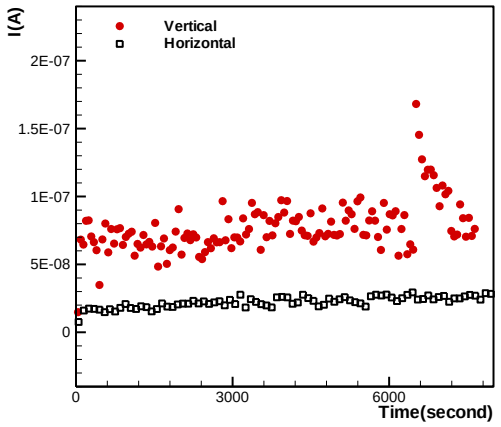

(b)

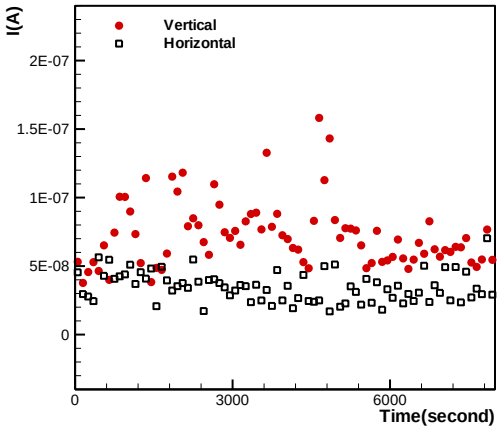

(c)

Figure 3.12 Induced current value (negative) of vertical pipe versus horizontal pipe: (a) Disperse flow (air flowrate 1600L/min, air superficial velocity 21.2m/s); (b) Half-ring flow (air flowrate 1000L/min, air superficial velocity 13.3m/s); (c) Ring flow (air flowrate 860L/min, air superficial velocity 11.4m/s).

3.4 Inter-comparison of electrostatic characteristics

The equivalent current, I_c, of a granular flow system due to the motion of charge-carrying particles can be calculated by the following equation:

$$I_c = Q_p \cdot SF \tag{3.2}$$

where Q_p is the particle charge density and SF is the particle mass transported per unit time or solid flow rate. The equivalent current calculated according to Equation (3.2) for the three types of flow are listed as I_c and compared to the experimental data measured by MPCT in Tables 3.2~3.4. The calculated values are of the same order of magnitude as those measured using the MPCT. For example at the time point of 3960 seconds in Table 3.2, particle charge density, Q_p, is 3.761×10^{-10}C/g; solid flow rate for disperse flow pattern, SF, is about 44.4g/s, thus the product of Q_p and SF, I_c, can be calculated as 1.670×10^{-8}A, which is nearly equal to the value of the equivalent current of granular flow measured by MPCT (1.713×10^{-8}A). Therefore, it demonstrated that the equivalent current of granular flow could be expressed as the product of particle charge density and solid flow rate. The agreement between the two is better at lower flow rates. This may be attributed to the fact that the MPCT is more accurate when electrostatic effects become stronger at lower flow rates or other experimental factors such as fluctuations in solid flow rate which may become significant at high air flow rates but is not taken into account in Equation (3.2).

Table 3.2 Transient equivalent current of charged disperse flow.

Time (sec)	Qp[a] (10^{-10}C/g)	MPCT (10^{-8}A)	Ic[b] (10^{-8}A)
3960	3.761	1.713	1.670
4680	4.406	1.746	1.956
5460	11.586	1.715	5.144
6240	8.908	1.548	3.955
6960	11.790	1.743	5.235
7680	15.076	1.735	6.694
8460	13.344	1.944	5.925
9420	15.248	1.704	6.770
10200	9.705	1.703	4.309
11040	12.216	1.763	5.424

[a] Q_p: particle charge density; [b] $I_c = Q_p \times SF$, SF=44.4g/s ±4g/s.

Table 3.3 Transient equivalent current of charged half-ring flow.

Time (sec)	Q_p[a] (10^{-9}C/g)	MPCT (10^{-8} A)	I_c[b] (10^{-8} A)
720	1.258	2.859	2.190
1380	1.946	3.124	3.386
2160	2.531	3.417	4.404
2820	2.022	2.537	3.518
3540	2.911	2.841	5.065
4500	1.425	2.734	2.479
5280	2.968	2.326	5.164
5940	2.146	2.096	3.735
6600	2.499	1.970	4.349
7440	2.108	1.974	3.668
8100	2.679	1.881	4.661
9060	2.716	2.060	4.725
9720	3.190	2.105	5.550
10500	2.097	2.058	3.650
11220	2.942	2.106	5.118

[a] Q_p: particle charge density; [b] $I_c=Q_p \times SF$, SF=17.4g/s ±3g/s.

Table 3.4 Transient equivalent current of charged ring flow.

Time (sec)	Q_p[a] (10^{-9}C/g)	MPCT (10^{-8}A)	Ic[b] (10^{-8} A)
120	1.494	2.444	1.524
840	2.355	2.609	2.402
1740	1.189	2.319	1.213
3780	2.471	2.573	2.520
4440	2.091	2.172	2.133
5100	2.387	2.342	2.435
5820	1.906	2.351	1.944
6420	1.800	2.416	1.836
7320	2.653	2.003	2.706
8100	2.249	2.894	2.294

[a] Q_p: particle charge density; [b] $I_c=Q_p \times SF$, SF=10.2g/s ±2g/s.

3.5 Factors affecting electrostatics of the granular flow

3.5.1 Pipe material

The phenomenon of electrostatic charge generation due to particle-particle or particle-wall contacts is known as tribocharging. This is a material-dependent process that has important practical applications such as in the design of photo printing and electrostatic coating machines. In the literature (Diaz and Felix-Navarro, 2004), common insulating materials can be ranked according to their charging tendency to form a triboelectric series. Materials (e.g. PP granules) higher up in the series tend to become positively charged when rubbed or brought into contact with those (e.g. PVC pipe) lower down in the series. The position of materials in triboelectric series can be related to chemical structures of polymers. The halogenated polymers usually develop the most negative charge, while the hydrocarbons develop almost no charge (Diaz and Felix-Navarro, 2004). Furthermore, the interactions between the two materials with higher discrepancy (e.g. PP granules and PVC pipe) in triboelectric series generate more electrostatic charges than those with lower discrepancy (e.g. PP granules and PE film). Figure 3.13 shows the induced current acquired by the film. The induced current caused by the sliding of a single particle over the film was in the form of a pulse, while that measured by the electrometer represented the sum of numerous such pulses to form a continuous current due to the motion of a large number of particles. The absolute values of the negative component of the induced current sampled at a rate of $200s^{-1}$ are compared in Figure 3.13 (c). It can be seen that the current induced on the PVC wall is higher than that on the PE film. Figure 3.14 shows that the total accumulated charge for both materials obtained by time integration of Figure 3.13

increases at a constant rate with respect to time. However, more charges were generated by interactions between the PP particles with the PVC pipe wall than with the PE film. The particle charge density measured with the Faraday cage was also found to be higher in the former case than in the latter (Figure 3.15).

To characterize the extent of mechanical interactions between the PP particles and the inner surface of the pipe during a typical conveying process, the PE film was examined using a scanning electron microscope (SEM) after being used for different lengths of time. Figure 3.16 shows micrographs of the PE film surface magnified 1000 times after being used for 0, 2 and 10min respectively. It is evident that the quality of the film surface deteriorates very quickly during usage with deep gorges forming after 10min. This confirms the presence of strong sliding effects and frictional forces between particles and the pipe wall.

As shown in the previous section, more particles tend to slide on the pipe wall with the airflow rate decrease, either at the vertical pipe (Figure 3.1~3.3) or horizontal pipe (Figure 3.8). Henthforth, it is reasonable to believe that for the three granular flows in the pneumatic conveying system, the electrostatic charge generation mechanism between particles and pipe wall mainly depends on the tribroelectrification.

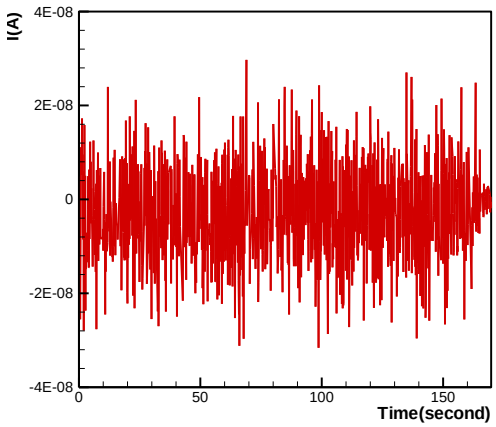

(a)

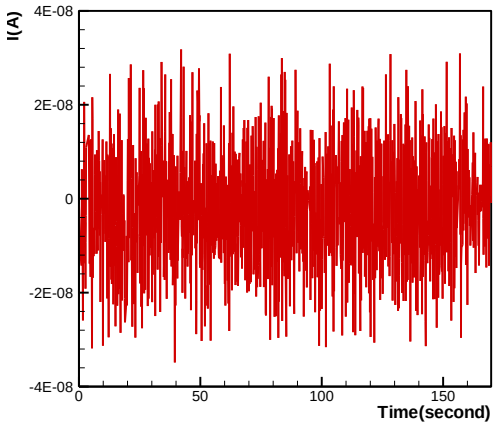

(b)

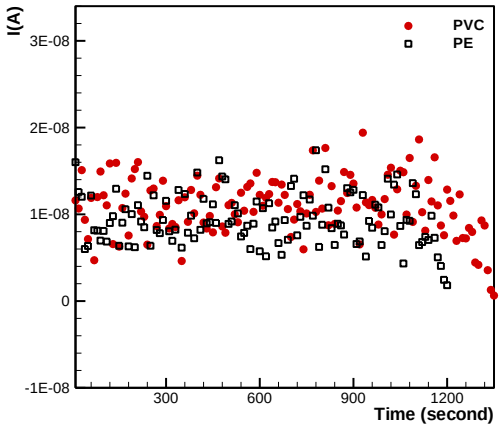

(c)

Figure 3.13 Induced current for two films (experiment setup B, horizontal pipe with air flowrate 1600L/min, air superficial velocity 21.2m/s): (a) PVC; (b) PE; (c) PVC versus PE (negative value).

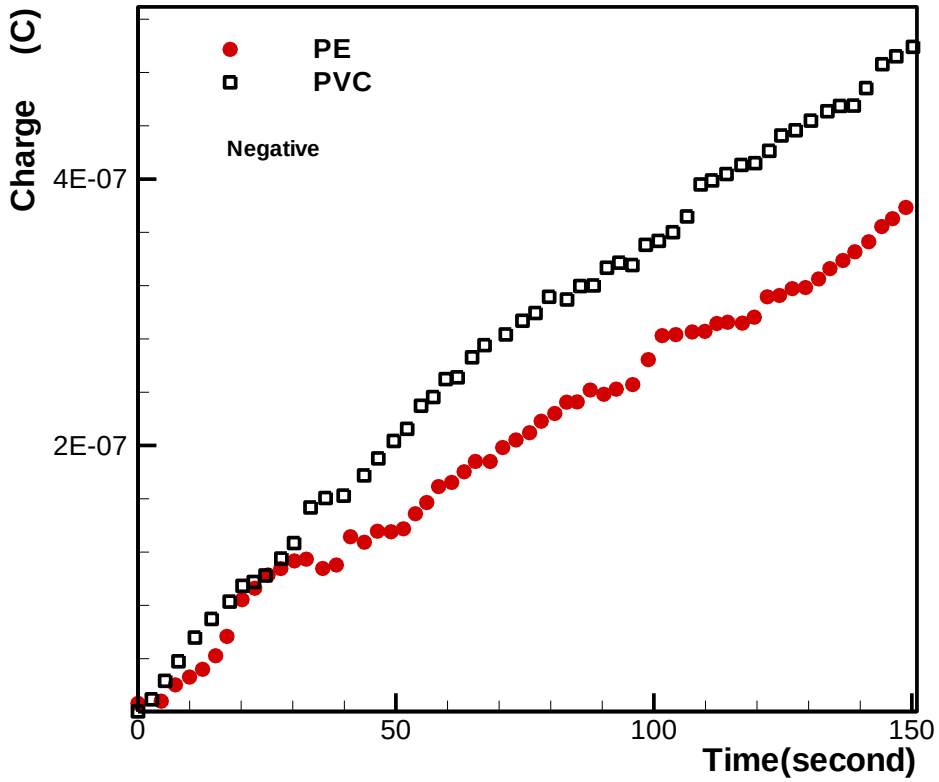

Figure 3.14 Charges obtained by integration of induced currents (shown in Figure 3.13 (a, b), experiment setup B) PVC versus PE.

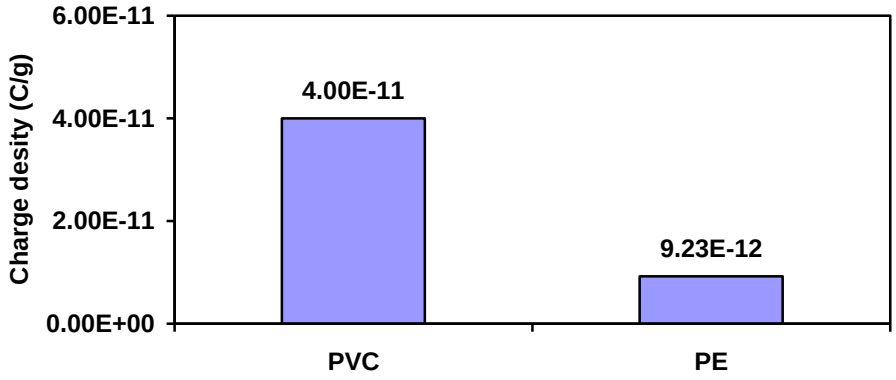

Figure 3.15 Particle charge density determined using Faraday cage (experimental setup B with air flowrate 1600L/min, air superficial velocity 21.2m/s): PVC versus PE.

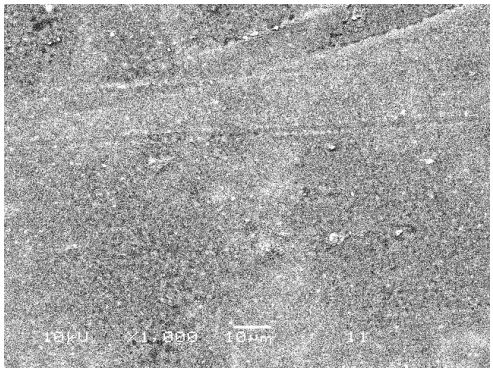

(a)

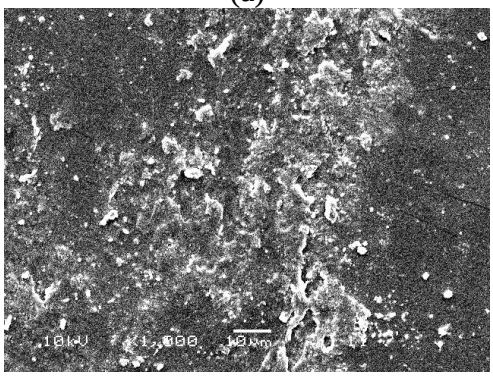

(b)

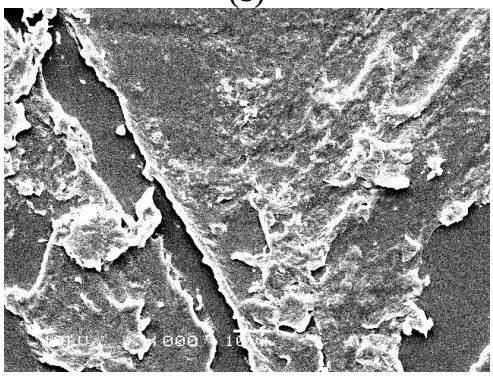

(c)

Figure 3.16 Scanning electron micrographs (SEM) of PE film (thickness 0.04mm, experimental setup B with air flowrate 1600L/min, air superficial velocity 21.2m/s): (a) Fresh film, (b) Used for 2min, (c) Used for 10min.

3.5.2 Relative humidity (RH)

The relative humidity of the ambient air is an important factor to be considered in any electrostatics experiment (Nieh and Nguyen, 1988). In the present work, both natural air from the atmosphere with an RH value of about 70% and air dried to an RH value of about 5% by passing through a silica gel column were used (labeled 2 in Figure 2.1 and Figure 2.2) under the ambient air temperature of 28~30 ℃. Figure 3.17 shows that particle charge density was lower at high humidity level and vice versa. There were also more fluctuations in both the particle charge density values and magnitudes of the induced current on the pipe wall at RH=5%. As seen previously in Figure 3.4 (a), induced currents fluctuated in the range $\pm 2.0 \times 10^{-7}$A when RH was 5% while the present investigation using ambient air resulted in a fluctuation range of $\pm 1.0 \times 10^{-7}$A (Figure 3.18 (a)). The absolute values of the induced current (Figure 3.18 (b)) as well as the total accumulated charge (Figure 3.19) showed similar trends. In other words, high RH of the conveying gas has a dampening effect on electrostatic charge generation. The reason may be that the enhanced probability of contact between electron and water vapor resulted in the formation of inactive ion, when the conveying air at high RH level was used. This claim is also supported by the fact that no half-ring or ring structure was visually observed when natural ambient air was used as the conveying medium, regardless of the flow rate used.

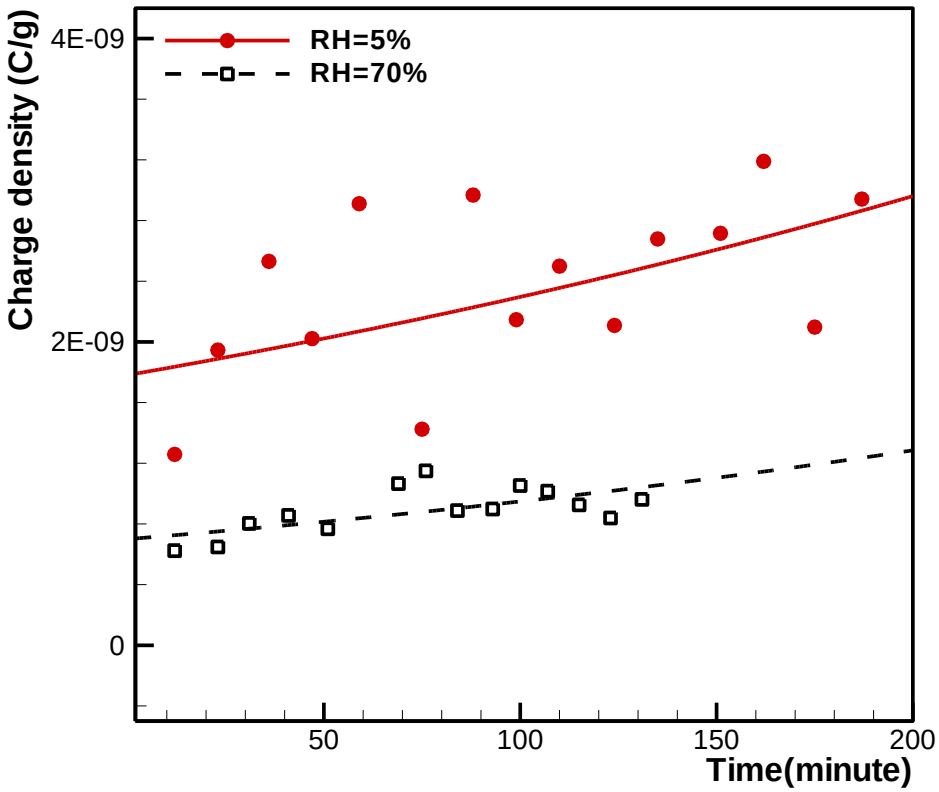

Figure 3.17 Particle charge density (determined using Faraday cage) of the half-ring flow (air flowrate 1000L/min, air superficial velocity 11.4m/s): RH=5% versus RH=70%.

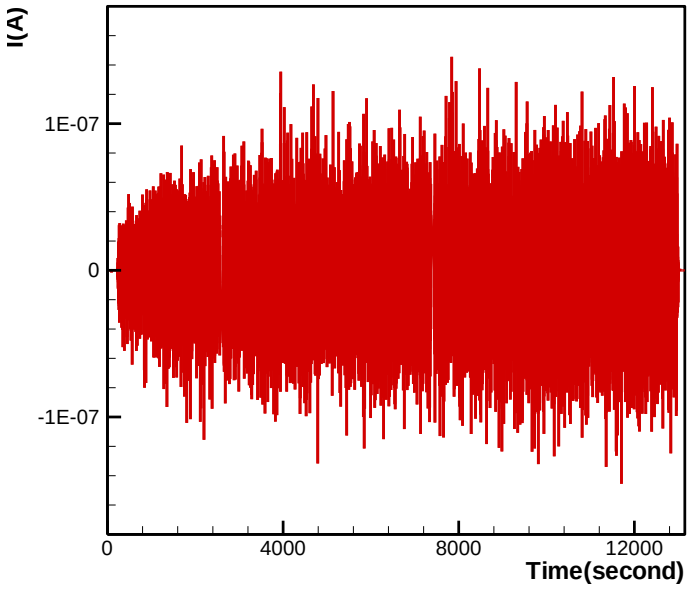

(a)

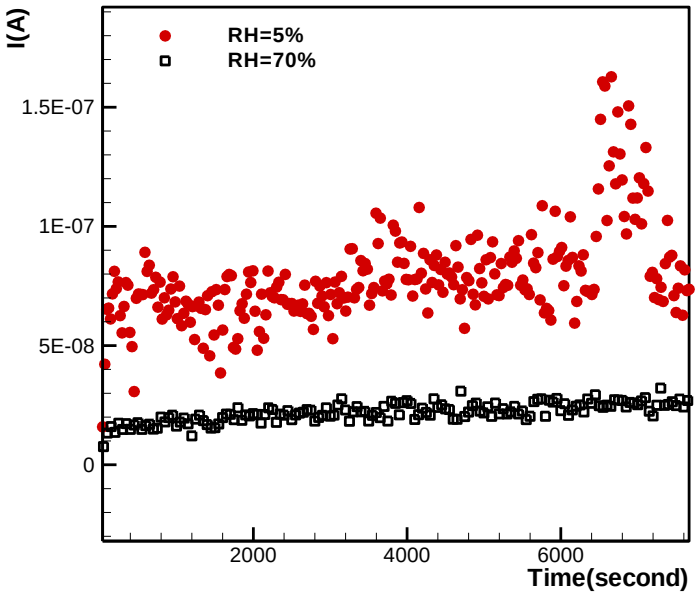

(b)

Figure 3.18 Induced current the vertical pipe (half-ring flow with air flowrate 1000L/min, air superficial velocity 11.4m/s): (a) RH=70%; (b) RH=5% versus RH=70%.

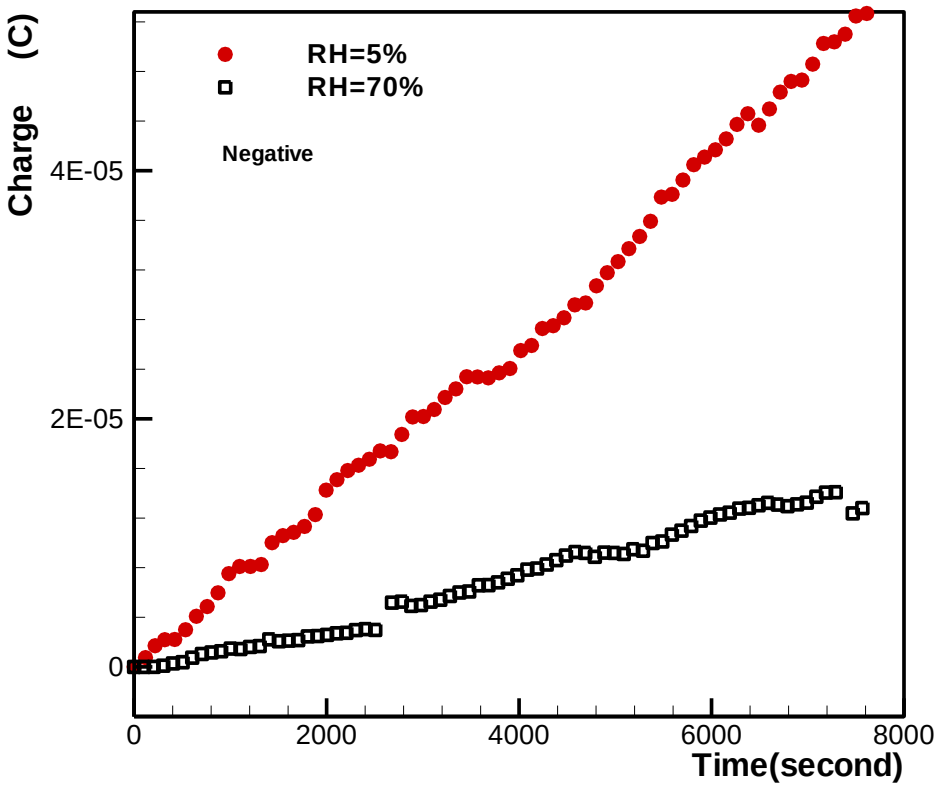

Figure 3.19 Charge obtained by integration of induced current at the vertical pipe: RH=5% (Figure 3.4 (b)) versus RH=70% (Figure 3.18 (a)).

3.5.3 Antistatic agent

The ability to effectively control and reduce electrostatic effects in a pneumatic conveying system is an important yet poorly understood research area. Wolny and Opalinski (1983) studied the mechanism of electric charge neutralization by the addition of fines to a fluidized bed. According to this mechanism, the fines change the contact conditions between particles of the bed, and transfer electric charge between particles, causing neutralization of the whole bed. For instances, antistatic powder Larostat-519 was used by Zhang et al. (1996) and Chang and Louge (1992), but its antistatic mechanism was never explained. However, such a commercially available anti-static agent, Larostat-519 powder (Zhang et al. 1996), may be a suitable means to achieve the purpose mentioned above. This is a non-inflammable white powder with bulk density 520kg/m^3, composed of about 60% soyadimethylethylammonium and 40% ethasulfate amorphous silica. In this section, the effectiveness of this anti-static agent was characterized. In comparison with previous cases where no such agent was used, the induced current measured in the presence of the Larostat-519 powder (0.5% by weight) was observed to be smaller by about three orders of magnitude (Figure 3.20). The same drastic drop in magnitude was also observed in the accumulated charge by comparing Figures 3.11 and 3.21. In terms of flow patterns, the Larostat-519 powder has the effect of suppressing the formation of half-ring and ring structures in the vertical pipe segment but not in the horizontal segment. This may be an indication that these structures formed in the horizontal pipe not as a result of electrostatic effects only and other factors may also be contributing to their appearance.

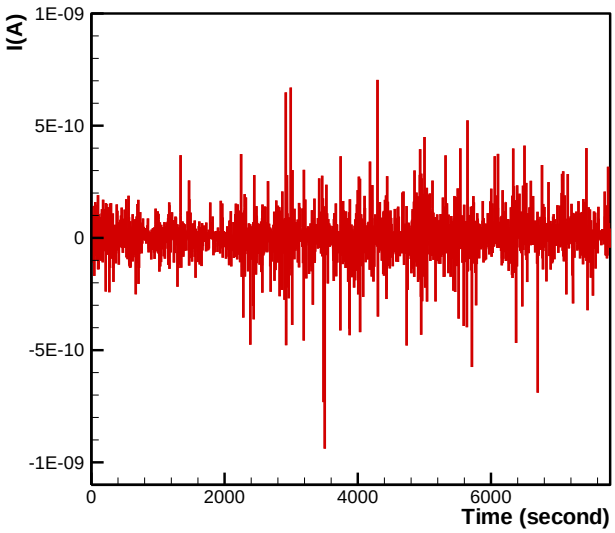

(a)

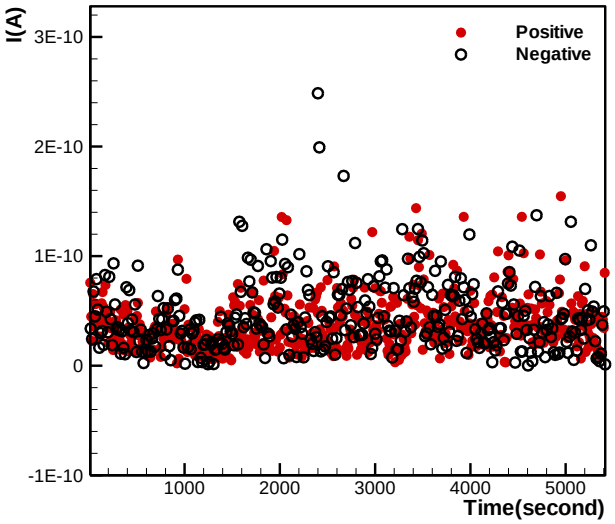

(b)

Figure 3.20 Induced current of the antistatic disperse flow measured at the vertical pipe (air flowrate 1600L/min, air superficial velocity 21.2m/s): (a) Temporal evolution of induced current; (b) Absolute values of positive versus negative values.

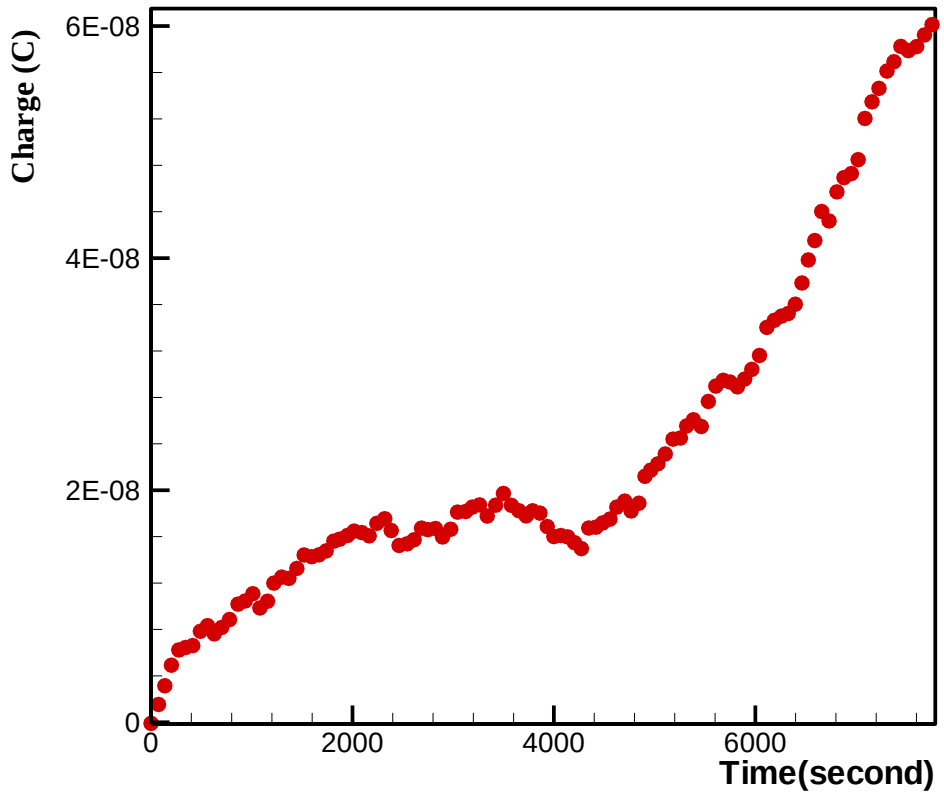

Figure 3.21 Charges obtained by integration of the induced current (shown in Figure 3.20 (a))

Figure 3.22 shows the scanning electron micrograph of the surface of a PP particle before and after mixing with the Larostat-519 powder. It is seen that the particle surface becomes coated with a thin film of powder after mixing. Here, a parallel can be drawn between a PP particle whose surface is covered with a film of Larostat-519 powder colliding with the pipe wall covered by a film made of the same material (Zhu et al. 2004b). Therefore, the interactions between two identical materials generate much less electrostatic charges than that between two different materials. It has been established previously that a pipe wall covered with a PE film leads to very different electrostatics phenomena and so a similar kind of observation is expected with the use of the Larostat-519 powder. The almost similar readings obtained from the MPCT for the cases where the powder was either absent or present in the system may be due to the inherent inaccuracies of the instrument in detecting low current signals (Figure 3.23).

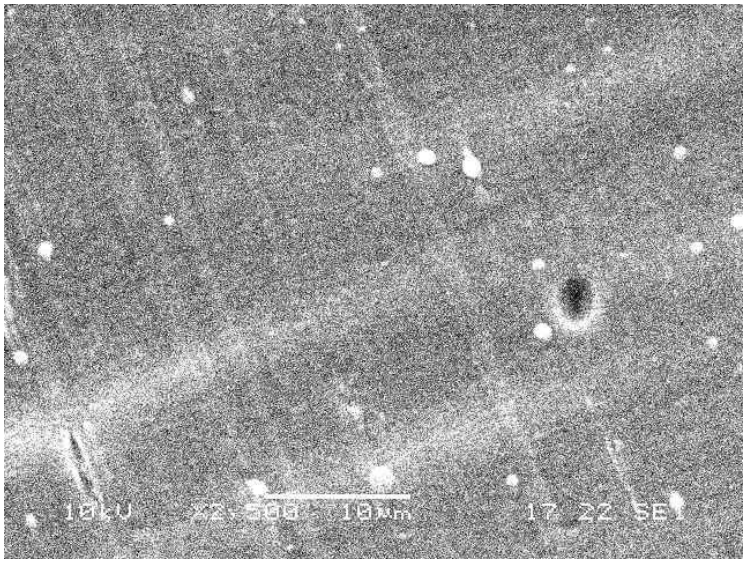

(a)

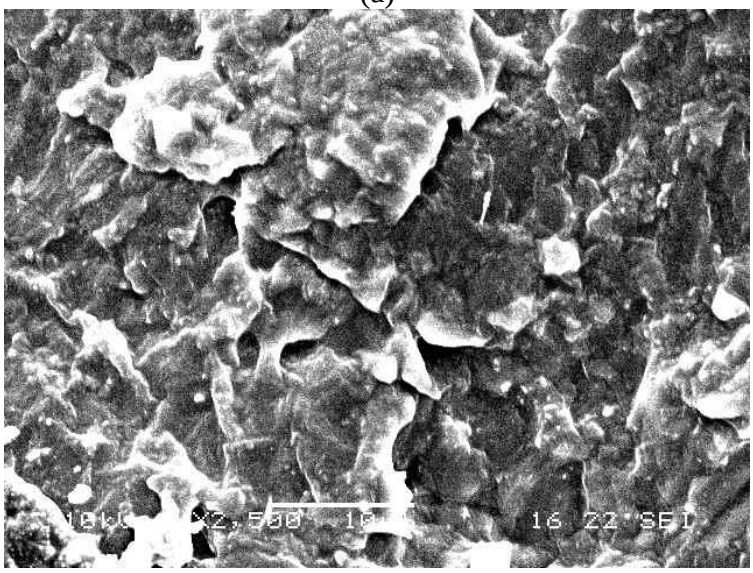

(b)

Figure 3.22 Scanning electron micrographs of PP particles in the pneumatic conveying system (dispersed flow with air flowrate 1600L/min, air superficial velocity 21.2m/s): (a) Clean particle; (b) Mixed with Larostat-519 powder.

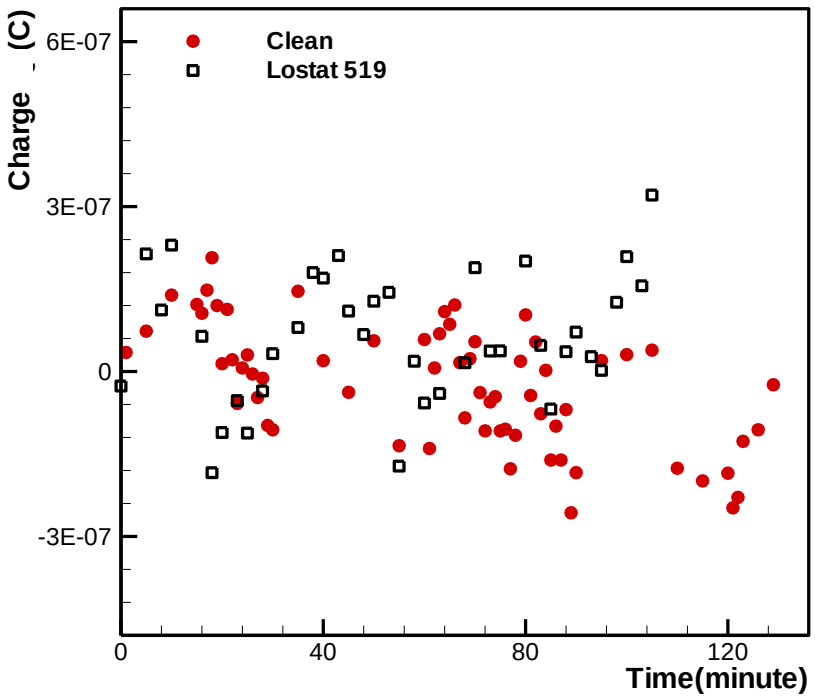

Figure 3.23 Charges obtained by integration of 400 MPCT values within a time interval of 20s: clean granular flow versus antistatic granular flow (disperse flow at the vertical pipe with air flowrate 1600L/min, air superficial velocity 21.2m/s)

3.6 Concluding remarks

The present work can be summarized as follows. First, air flow rate is the main element determining the electrostatic behavior of granular flow. The lower the airflow rate, the higher are the induced current and particle charge density. These in turn lead to particle clustering and the formation of such structures as half-ring and ring in the vertical conveying pipe. Second, electrostatic effects increase with time. The charge accumulated at the pipe wall increases with time, and the rate of increase seems to be constant for each of the three flow patterns. Particle charge density also increases with time and this may account for clustering behavior occurring at the vertical pipe wall even when a high air flow rate is used and the dominant flow regime is that of disperse flow. Third, , pipe wall material has an obvious effect on the electrostatics of the granular flow. The various parameters used throughout this work to characterize electrostatic effects such as the induced current and accumulated charge were shown to be higher when PVC pipe was used instead of a PE film attached to the inner wall in the conveying system. Fourth, air with high RH also tends to reduce electrostatic effects when used for pneumatic conveying of particles. No half-ring and ring flow patterns attributable to strong electrostatic effects were observed when ambient air with a RH of about 70% was used in the system. Fifth, the commercially available antistatic agent, Larostat-519 powder, was found to reduce electrostatic effects within the system effectively. Besides, it is clear that the mechanism of electrostatic charge generation for the granular flow in the pneumatic conveying system mainly depends on triboelectrification due to the strong force effect on the surface when the particles slide on the pipe wall.

Chapter 4. Electrostatic effect of granular flow on inclined pneumatic conveying pipe

Research work carried out in the field of pneumatic conveying systems can be categorized according to different geometries of the conveying section used in the transportation process. These include pneumatic conveying through horizontal, vertical and inclined pipes and about a bend. The aim of this work was to study three flow patterns, named dispersed, reverse and half-ring flow, observed in a 45° inclined conveying pipe. The methods applied for capturing solid flow patterns and velocity profiles include ECT, PIV and high-speed camera. The study on flow patterns is a fundamental concept in pneumatic conveying systems and is helpful towards understanding real life problems which may arise during actual operations. The appearance of the variety of solid flow patterns observed in laboratory experiments or actual industrial operations are normally attributed to the physical conditions used. However, some peculiar clustering behaviors may not be accounted for purely by hydrodynamics effects alone, such as the formation of ring structures in vertical and inclined pneumatic conveying. This chapter attempts to analyze such flow behaviors of solid particles in an inclined pneumatic conveying pipe through the consideration of the effects of electrostatic charge generation. This continues from previous research studies in Chapter 3 on the electrostatics of granular flow in horizontal and vertical pneumatic conveying systems and provides further insights into the relationship between solids flow behavior and electrostatic effects.

4.1 Flow patterns and velocities for particle transport in a 45 °inclined conveying pipe

Depending on the different airflow rates, three distinct phenomena, namely dispersed flow, reverse flow and half-ring flow for particles transport in a 45 ° inclined conveying pipe was observed and schematically illustrated in Figure 4.1 (a, b and c).

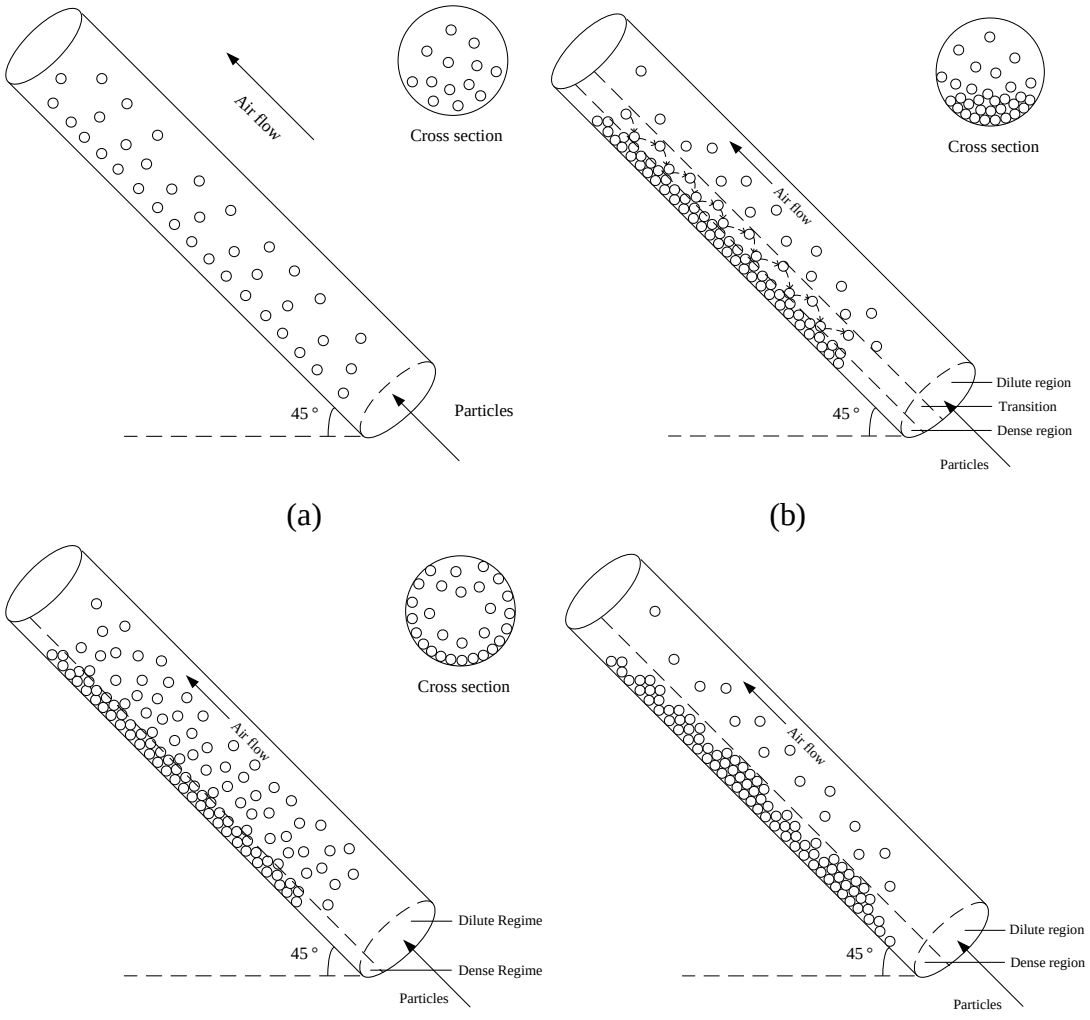

Figure 4.1 Schematic of particle flow in three different flow patterns in pneumatic conveying: (a) Dispersed flow; (b) Reverse flow; (c) Half-ring flow; (d) Reverse flow with pulsating wave.

4.1.1 Dispersed flow pattern

Figure 4.2 shows the images of particles concentration captured by ECT on plane 1 and plane 2 respectively. When airflow rate is 1600L/min, particle concentration is generally low and particles do not concentrate on the pipe wall. As such, it forms the dispersed flow pattern.

By post-processing the ECT data at each instant of time, *t*, using the simultaneous iterative reconstruction technique (SIRT) described by Su et al. (2000), the concentration of each pixel in one plane, $\alpha(x,y,z,t)$, was obtained. Here, as shown in Figure 4.3, *x* and *y* denote Cartesian coordinates in the cross-sectional plane, made dimensionless using the pipe diameter as the characteristic length, and *z* is the axial coordinate denoting the location of the ECT electrodes. The solid velocity can be calculated based on cross-correlation of twin plane data, which was described by Hua et al. (1999), Rao et al. (2001) and Zhu et al. (2003). The time-averaged particle concentration $\overline{\alpha}_t$ was found by averaging $\alpha(x,y,z,t)$ over a time period *T* (30s in this case):

$$\overline{\alpha}_t(x,y,z) = \frac{1}{T}\int_0^T \alpha\ (x,y,z,t)dt \tag{4.1}$$

The instantaneous value of the cross-sectional average particle concentration, $\overline{\alpha}_s(z,t)$, is defined as:

$$\overline{\alpha}_s(z,t) = \frac{1}{A}\iint \alpha(x,y,z,t)\ dx\ dy \tag{4.2}$$

and the time-averaged value of $\overline{\alpha}_s(z,t)$ is denoted by <α>(z):

$$\langle\alpha\rangle(z) = \frac{1}{T}\int_0^T \bar{\alpha}_s(z,t)dt \equiv \frac{1}{A}\iint \bar{\alpha}_t(x,y,z)dxdy \tag{4.3}$$

The correlation coefficient, *c(d)*, was then computed as

$$c(d) = \frac{1}{T}\int_0^T (\bar{\alpha}_s(z_1,t) - <\alpha>(z_1))(\bar{\alpha}_s(z_2,t+d) - <\alpha>(z_2))dt \tag{4.4}$$

here, z_1 and z_2 refer to upstream and downstream planes respectively; *d* denotes the delay time. The dominant pattern propagation velocity, *V*, was estimated from $V=L/D$, where $L=z_2-z_1$ (L=2.18-1.45=0.73m in the current work), is the axial distance between the two ECT sensors and *D* is the value of *d* at which *c(d)* assumes the largest value. *V* estimated in this manner is clearly based on cross-sectional averages. One can also define pixel-pixel cross-correlation function as:

$$c(x,y,d) = \frac{1}{T}\int_0^T (\alpha(x,y,z_1,t) - \bar{\alpha}_t(x,y,z_1))\ (\alpha(x,y,z_2,t+d) - \bar{\alpha}_t(x,y,z_2))\ dt \tag{4.5}$$

The dominant pattern propagation velocity, *V(x,y)*, was estimated from Equation (4.6):

$$V(x,y) = L/D(x,y) \tag{4.6}$$

where *D(x,y)* is the value of *d* at which *c(x,y,d)* assumes the maximum value (for *x*, *y*).

One limitation of the classical cross-correlation method arises from a basic assumption that the particle motion between the sensors is parallel to the pipe axis, i.e. perpendicular to the sensor plane. However, the actual movements are quite complex, and the trajectories of particles do not remain parallel to the pipe axis. Thus, it is necessary to introduce a new method (Msosorov et al. 2002), namely best-correlated pixel method, which does not require the assumption about the solid trajectories within a sensor volume.

This method is to calculate cross-correlation between a pixel from the first plane and a number of pixels from the second plane. The pixels from the second plane are chosen from the corresponding pixel and all its neighbors. Equation (4.7) describes the function in details:

$$c(x,y,i,j,d)=\frac{1}{T}\int_0^T(\alpha(x,y,z_1,t)-\overline{\alpha_t}(x,y,z_1))(\alpha(i,j,z_2,t+d)-\overline{\alpha_t}(i,j,z_2))dt \tag{4.7}$$

where *(i,j)* are dimensionless coordinates of the pixel in plane 2, $\alpha(x,y,z_1,t)$ and $\alpha(i,j,z_2,t+d)$ are the values associated with pixel *(x,y)* from the image at time *t* obtained from plane 1 and pixel *(i,j)* from image at time *(t+d)* obtained from plane 2 separately. Therefore, similar to the classical cross-correlation method, when $c(x,y,i,j,d)$ reaches its maximum, *d* is $D(x,y)$ and according to Equation (4.6), axial solid velocity of each pixel, $V_z(x,y)$, can be obtained. Figure 4.4 shows the result of velocity calculated by the best-correlated pixel method. It is observed that velocities are high over the entire pipe.

Furthermore, the coordinates *(i, j)* on plane 2 (non-dimensionalized by pipe diameter as the characteristic length scale) can be obtained, according to the best-correlated pixel method. If $i=x$, $j=y$, it shows that the particles maintain their direction during the transport from plane 1 to plane 2; otherwise, it reflects the direction change of particles. Therefore, in such case, the actual velocity for particle transport between planes 1 and plane 2 is:

$$\vec{V}=\begin{pmatrix}V_x\\V_y\\V_z\end{pmatrix} \tag{4.8}$$

here, V_x, V_y and V_z are the magnitudes of the velocity components in the three perpendicular directions respectively. The lateral velocity can be defined as the

projection of $\vec{V}$ on the pipe cross section and described as:

$$V_l(x,y) = 2R\sqrt{(x-i)^2 + \quad (y-j)^2} \,/\, D(x,y) \tag{4.9}$$

where R is pipe radius. The average lateral velocity for the dispersed flow pattern was calculated to be around 8×10^{-4} m/s and appeared negligible as compared to the axial velocity, as will be shown in Figure 4.6.

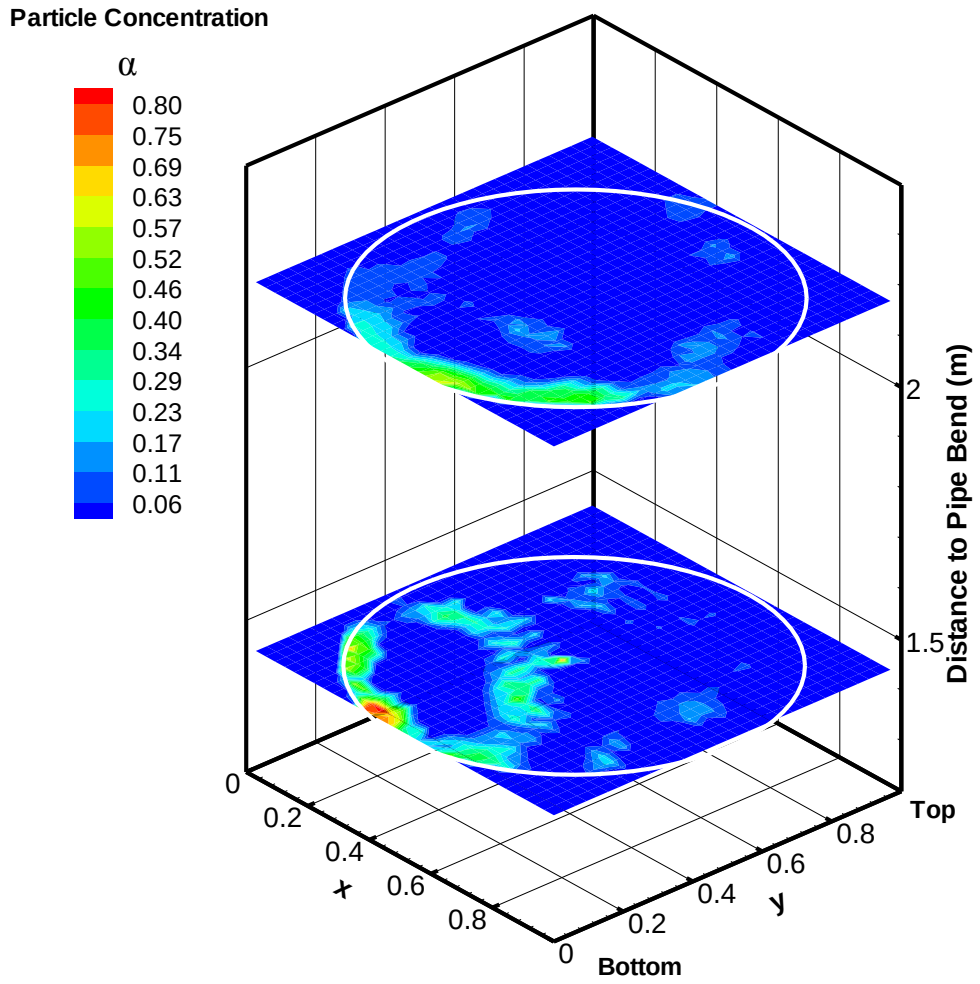

Figure 4.2 Images of particle concentration (α) at twin planes captured by ECT for the disperse flow pattern (air flowrate=1600L/min, air superficial velocity 21.2m/s).

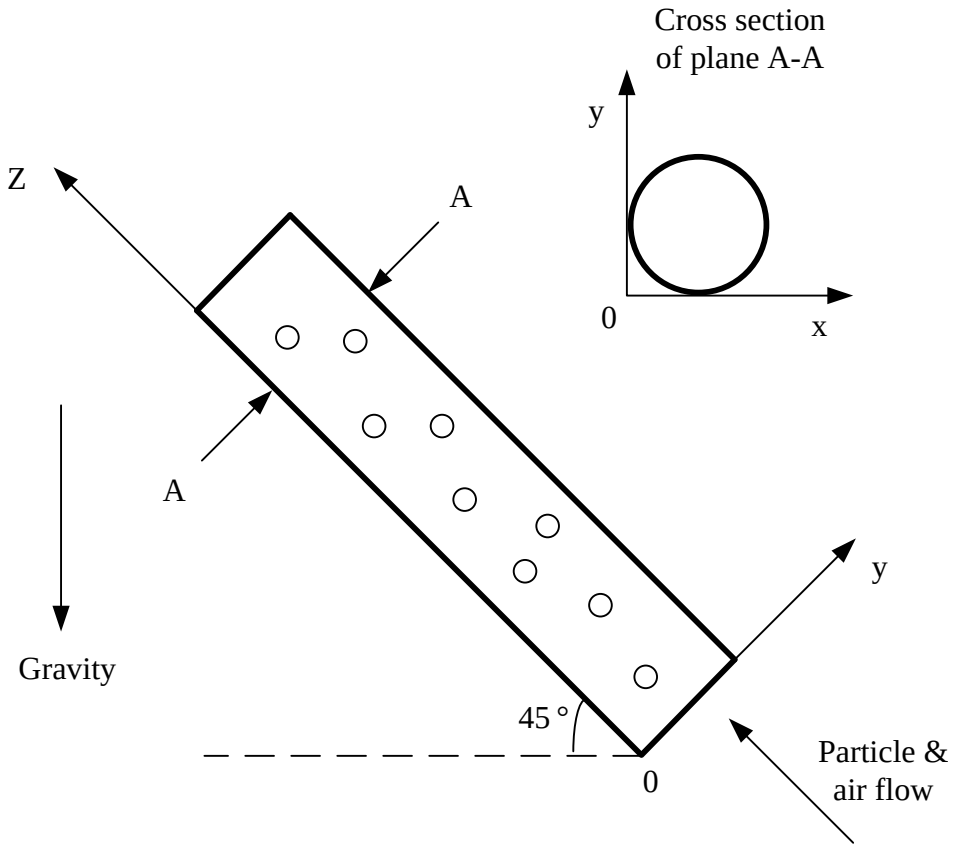

Figure 4.3 Geometry of inclined pneumatic conveying pipe.

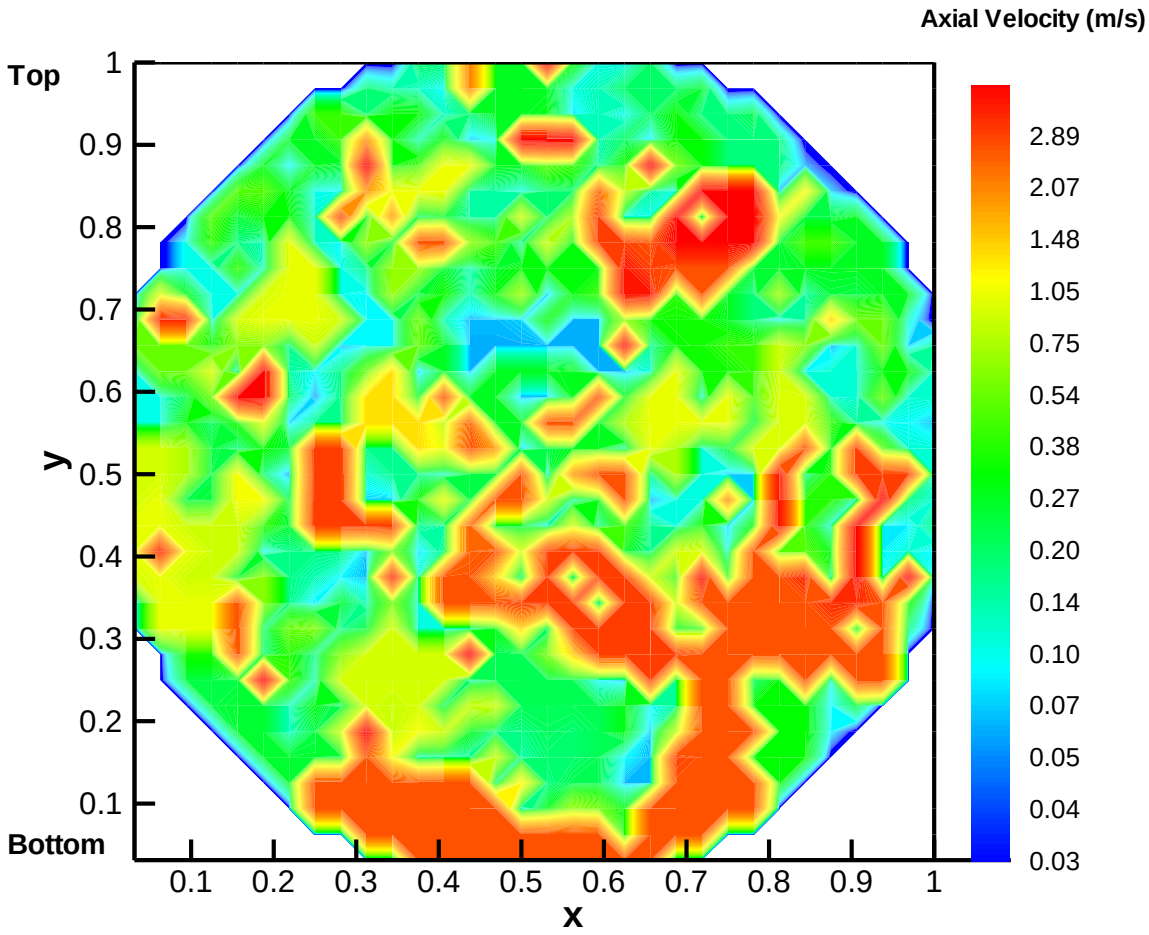

Figure 4.4 Particle axial velocity on pipe cross-section correlated from ECT data for the disperse flow pattern (air flowrate=1600L/min, air superficial velocity 21.2m/s).

Figure 4.5 shows the image of particle transport captured by high-speed video camera (FastCam PCI, Photron, CA, USA) at the frame rate of 250fps. The inclined pipes are positioned with the pipe axis at an angle of 45^{o} relative to the direction of gravity as indicated in Figure 4.5 (c). The direction of air flow is from right to left. Similar illustration is also applied to Figures 4.7, 4.10, 4.12, 4.15 and 4.21. In Figure 4.5, most particles are transported in regions close to the bottom pipe wall and the overall space among particles is fairly large, thus resulting in a dilute solid phase. For illustration purpose, one particle was chosen as an example and traced over several images. The positions of this particle in three images are marked in circles as shown in Figure 4.5. In general, particle motion is observed to follow the gas flow direction. Subsequently, 10 particles were chosen randomly from 1000 pictures over a period of 4s and the average velocity of particles was computed as the distance between the two positions in selected images divided by the duration between these two images. The average particle velocity value obtained was 1.59 ± 0.41m/s.

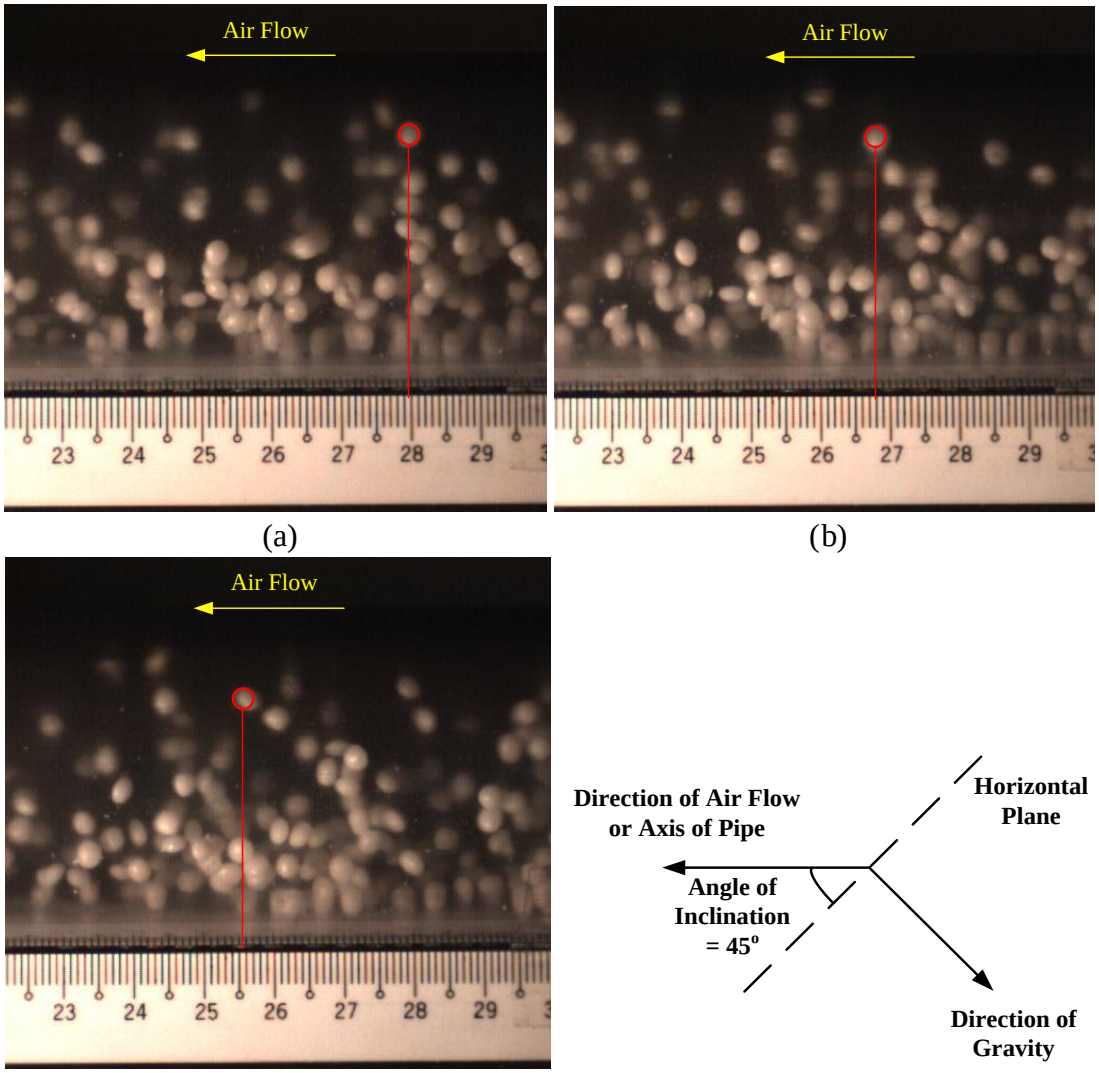

Figure 4.5 Image of particles transport for the disperse flow pattern captured by high-speed video camera (time difference between two successive pictures=0.004s, air flowrate=1600L/min, air superficial velocity 21.2m/s).

Figure 4.6 displays the velocity profile of particles at different positions along the pipe diameter. The data were obtained from ECT and PIV experiments, respectively. The figure shows that velocity profiles obtained from these two different methodologies exhibited similar trends. There are, however, some quantitative differences probably due to different extents of experimental errors associated with the two instruments. Here, velocities are normalized with respect to the maximum value of velocity observed within the pipe cross section. The normalized velocities are high near the pipe center, but decrease towards the pipe wall. Such profile was observed in both side view (Figure 4.6 (a)) and top view (Figure 4.6 (b)). This was also predicted by CFD simulation of pneumatic conveying of granular solids in inclined pipe (Zhu et al. 2004a). It may also be observed from the velocity profiles in both side and top views in Figure 4.6 that lateral velocities are much lower than those of axial velocities, implying that axial movement is primary for such flow pattern and thus validating the results obtained by Equation (4.9) from ECT data.

Figure 4.7 shows the side view image from the top to the bottom of the pipe of the dispersed flow pattern captured by PIV where the vector arrows verify the observation that particle flow directions are consistent with the airflow.

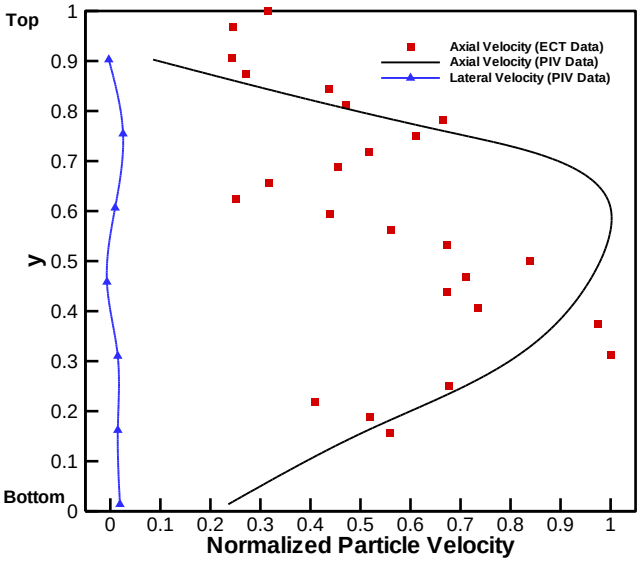

(a)

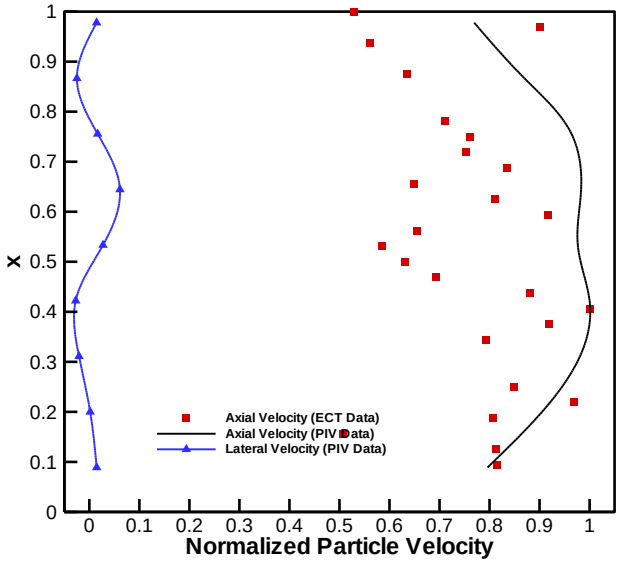

(b)

Figure 4.6 Diametrical distribution of particle axial velocity for the disperse flow pattern (air flowrate=1600L/min, air superficial velocity 21.2m/s): (a) Side view; (b) Top view.

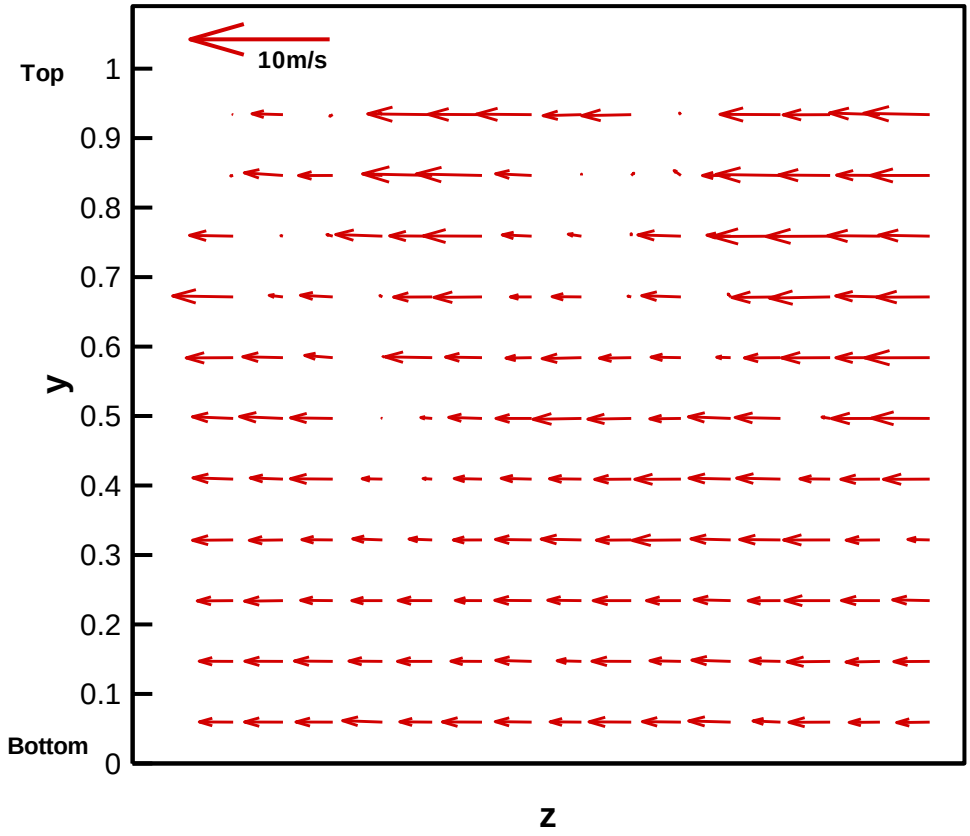

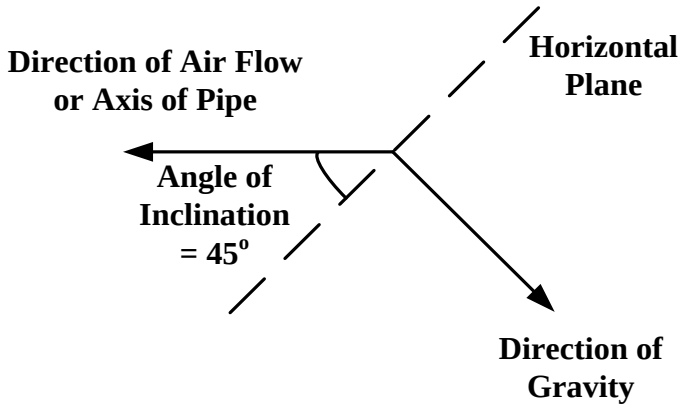

Figure 4.7 Velocity vectors for the dispersed flow pattern by PIV measurements (air flowrate=1600L/min, air superficial velocity 21.2m/s).

4.1.2 Reverse flow pattern

When the airflow rate is decreased to 1100L/min, it is observed in the experiment that some particles near or above the pipe center moved forward with fairly high velocities; while most particles were deposited and formed layers at the bottom of the pipe. These slid backwards in a direction opposite to that of the general flow direction at relatively slow velocities. These are represented by the red parts in Figure 4.8.

Figure 4.9 presents the resulting velocity obtained with the best-correlated pixel method for the reverse flow pattern. In this figure, the whole solid phase is divided into three parts. It is observed that velocities are relatively high and positive near and above the center of the pipe, where the corresponding coordinate along the *y* axis are 0.35~1; while those at the bottom (y=0~0.18) are very small and negative. These two areas are defined as dilute and dense regions respectively. Particles at the interface between these regions (referred to as the transition region with y=0.18~0.35) flowed backwards with relatively higher negative velocities. The lateral velocities calculated from Equation (4.9) also show three distinct velocity scales increasing from 10^{-6} m/s, 10^{-5} m/s to 10^{-4} m/s from the dense region to the dilute region, respectively.

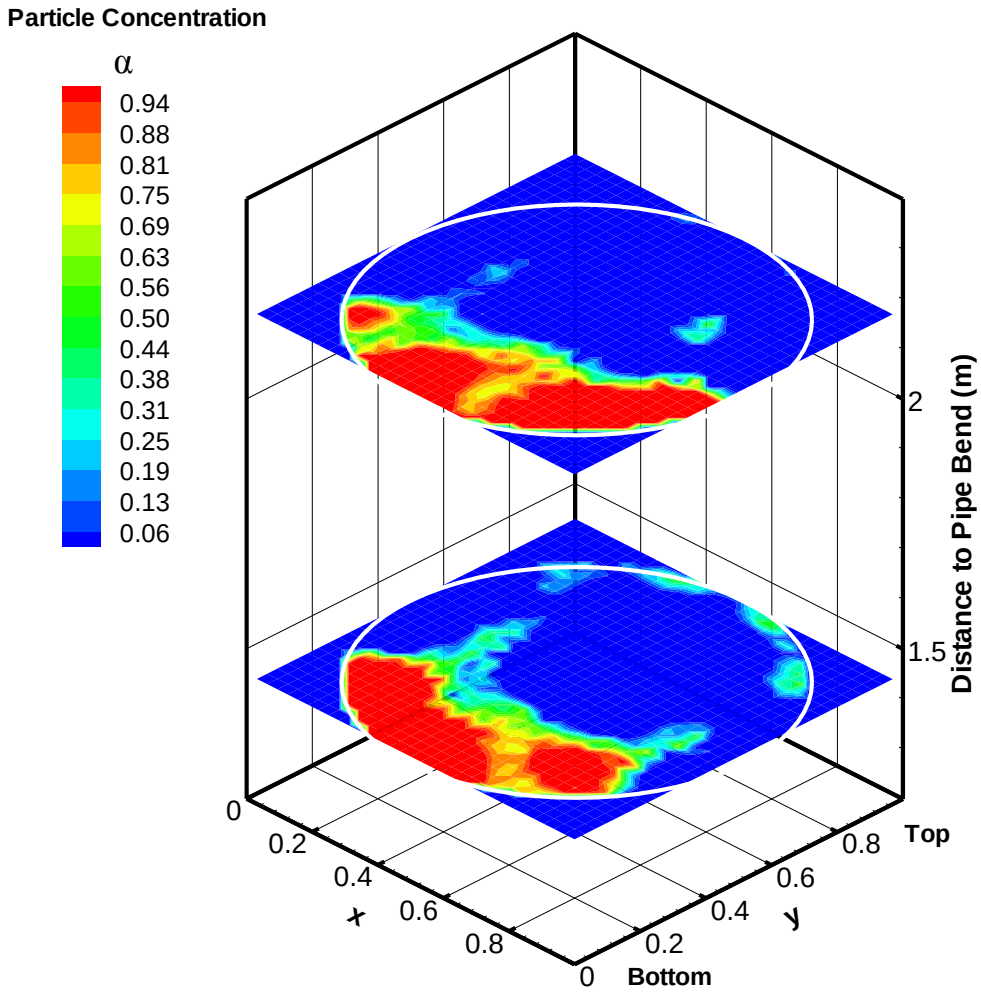

Figure 4.8 Images of particle concentration (α) at twin planes captured by ECT for the reverse flow (air flowrate=1100L/min, air superficial velocity 14.6m/s).

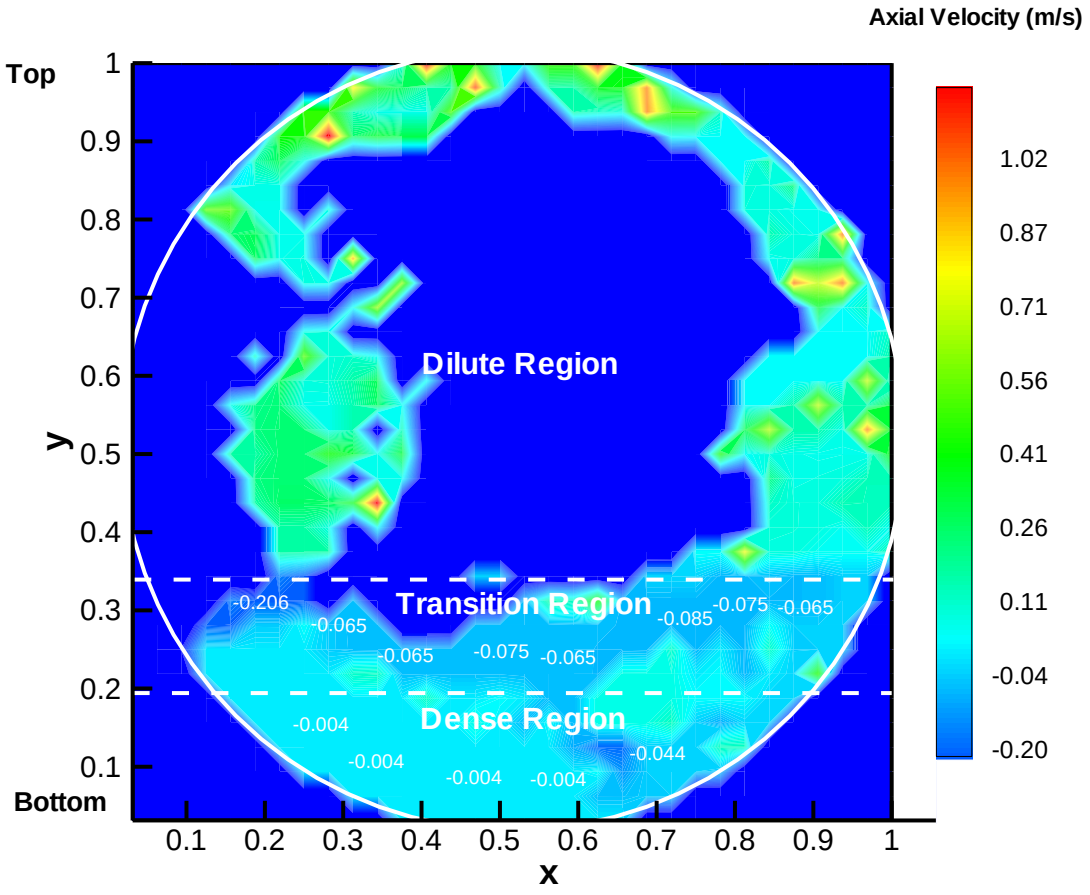

Figure 4.9 Particle axial velocity on pipe cross-section correlated from ECT data for the reverse flow pattern (air flowrate=1100L/min, air superficial velocity 14.6m/s).

The limitation of the cross-correlation method is that it is difficult to get exact values when data are same on two correlation planes, because the principle of correlation is based on variation of the data on two planes. For the dense region, the concentrations of particles measured by two ECT sensors are at the maximum values continuously. As a result, the velocities in this section are obtained from the images captured by a high-speed video camera, as shown in Figure 4.10. It can be seen that most of granules are accumulated at the bottom of the pipe, but a small amount is transported in the core region and at the top of the pipe. This is consistent with the solid fraction profile shown in Figure 4.8. In the dense region, particles at the bottom of pipe seem almost stationary and the velocity obtained is only about -0.0020 ± 0.00072m/s. The path traced by the particle is not shown as it is not easily interpolated between the two images. In the transition region, some particles close to the core of the pipe are active and referred to as transition particles. This is probably due to the shearing effects between the dilute and dense regions. The locations of the particle labeled with the symbol A in the three images indicate that it did not move ahead. Instead it seemed to have jumped over some particles in a direction opposite to the air flow. The average velocity is -0.05 ± 0.02m/s. However, in the dilute region, particles such as that labeled as B moved ahead with the average velocity of 0.62 ± 0.26m/s.

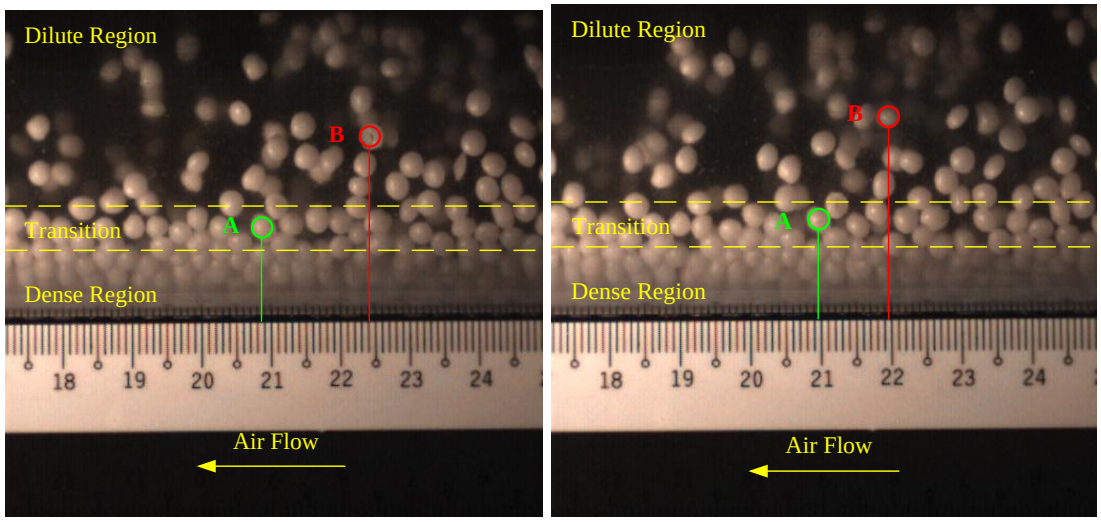

(a)

(b)

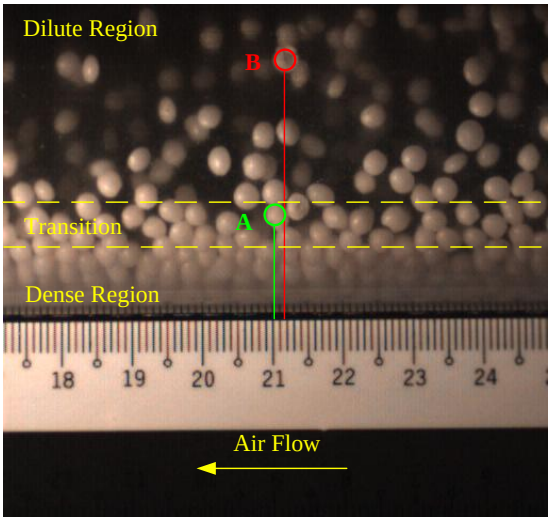

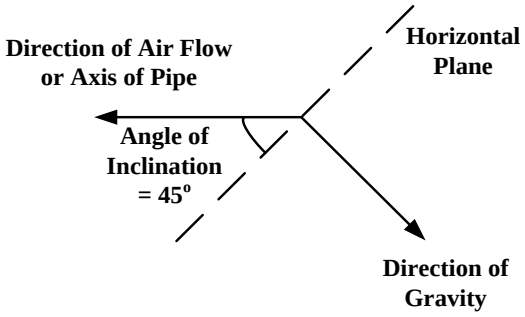

(c)

Figure 4.10 Image of particles transport for the reverse flow captured by high-speed video camera (time difference between two successive pictures=0.036s, air flowrate=1100L/min, air superficial velocity 14.6m/s).

Correspondingly, the normalized particle velocity profiles obtained from both ECT and PIV and presented in Figure 4.11 demonstrate that three regions exist in the solid phase. Positive velocities in the dilute region are generally forward flow. In contrast, in the dense and transition region, negative velocities indicate reverse flow. In particular, the change in velocity profile within the transition region revealed that reverse flow is significant in this zone. Figure 4.11 also shows that lateral velocities are much weaker in the dilute region as compared to axial velocities and hence can be neglected. However, in the transition and dense regions, the magnitudes of lateral and axial velocities are observed to be comparable. These findings further verify the three levels of lateral velocities observed from ECT data.

Arrows in the vector plot of Figure 4.12 are pointing towards two completely opposite directions. This finding demonstrates that some particles are floating in the dilute region and moving forward but some particles, especially those in the transition region, exhibit a backflow behavior. From the magnified zone, particles in the transition and dense regions also gave rise to some wave structures in the transverse direction.

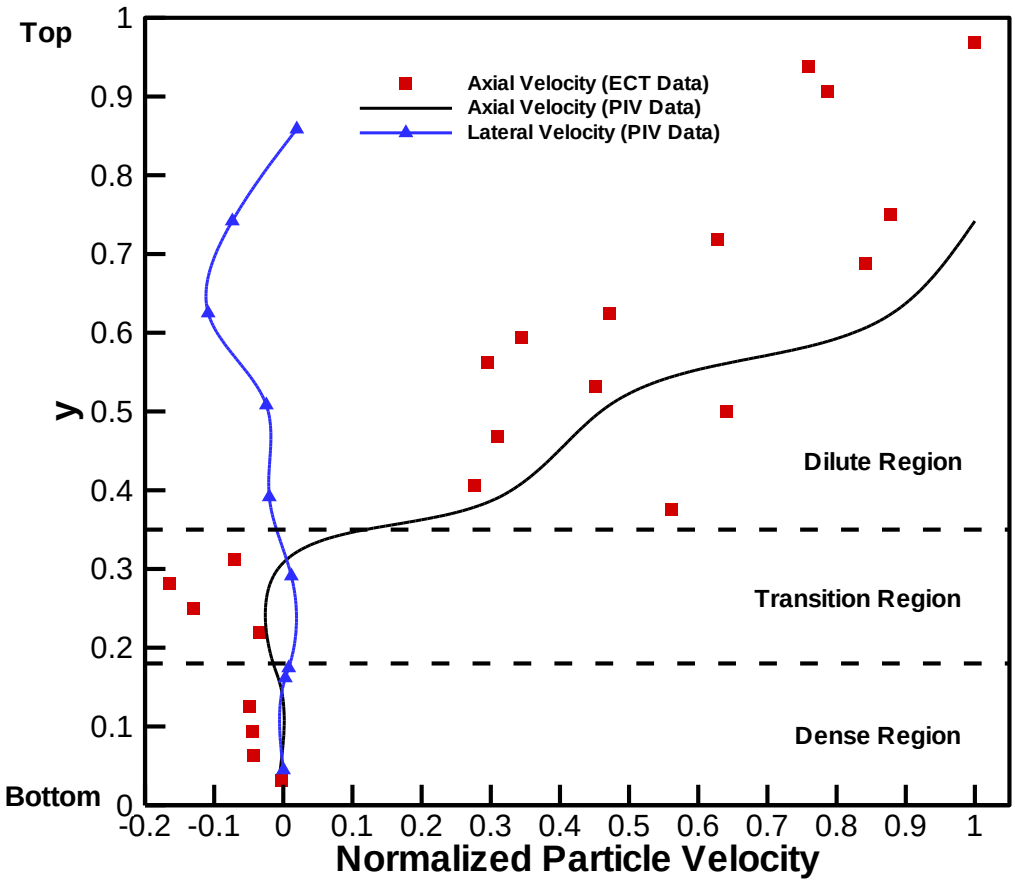

Figure 4.11 Diametrical distribution of particle axial velocity for the reverse flow (air flowrate=1100L/min, air superficial velocity 14.6m/s).

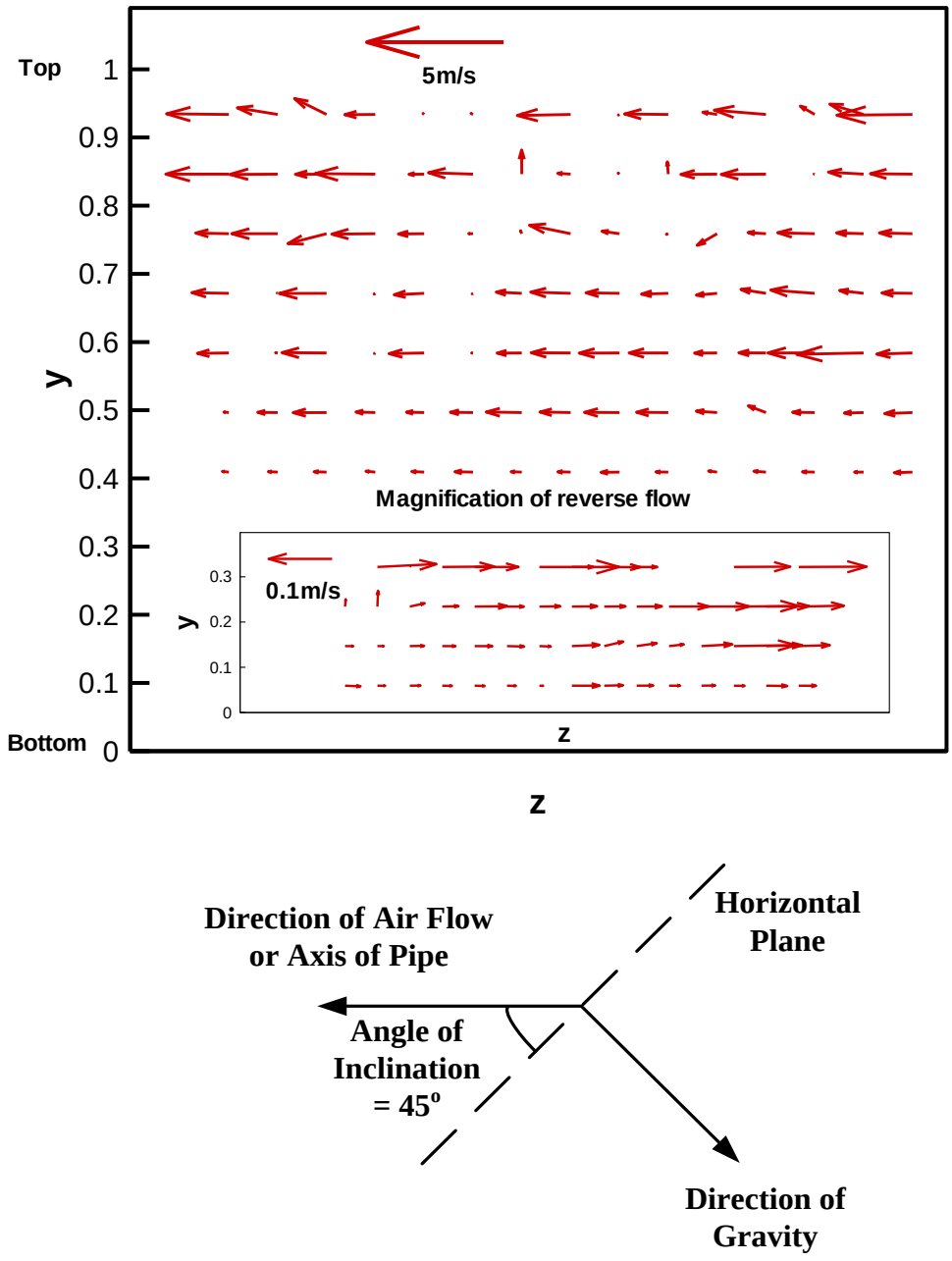

Figure 4.12 Velocity vectors for the reverse flow pattern from PIV measurements (air flowrate=1100L/min, air superficial velocity 14.6m/s).

4.1.3 Half-ring flow pattern

When the airflow rate is further reduced to 1000L/min, particles deposit at the bottom of the pipe and are stagnant initially. Later, particles concentrated on the pipe wall and gradually formed an annulus structure while those at the bottom continued to remain stagnant as shown in Figure 4.13. The thickness of this ring is roughly one layer of particles, and it seems the solid concentration at the top of the pipe is smaller than that at the bottom due to the action of gravity.

Figure 4.14 shows that velocity is zero at the bottom and relatively high at the top of the pipe wall, presenting an incomplete ring structure in the pipe cross-section. Correspondingly, the lateral velocities calculated according to Equation (4.9) for the dense and dilute regions are of magnitudes 10^{-4} m/s and 10^{-3} m/s, respectively. This shows that lateral motion is not negligible in the dense region while transverse motion becomes dominant in the dense region.

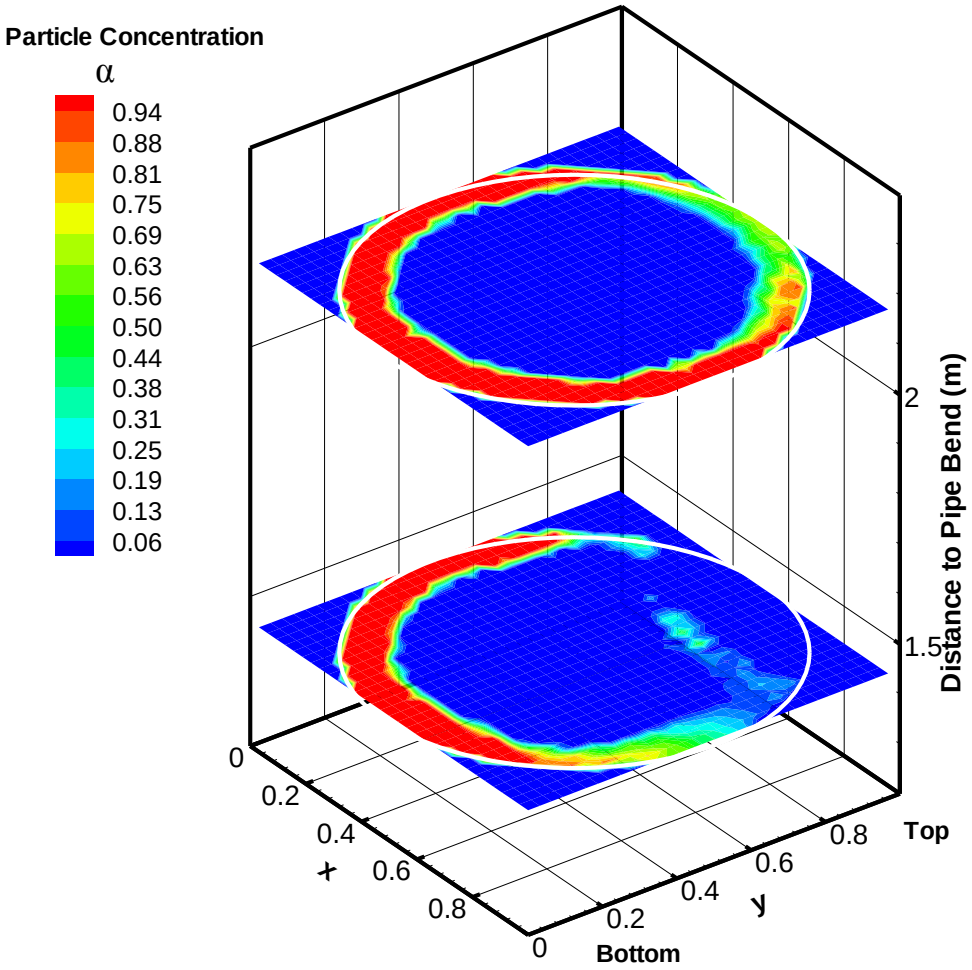

Figure 4.13 Images of particle concentration (α) at twin planes captured by ECT for the half-ring flow (air flowrate=1000L/min, air superficial velocity 13.3m/s).

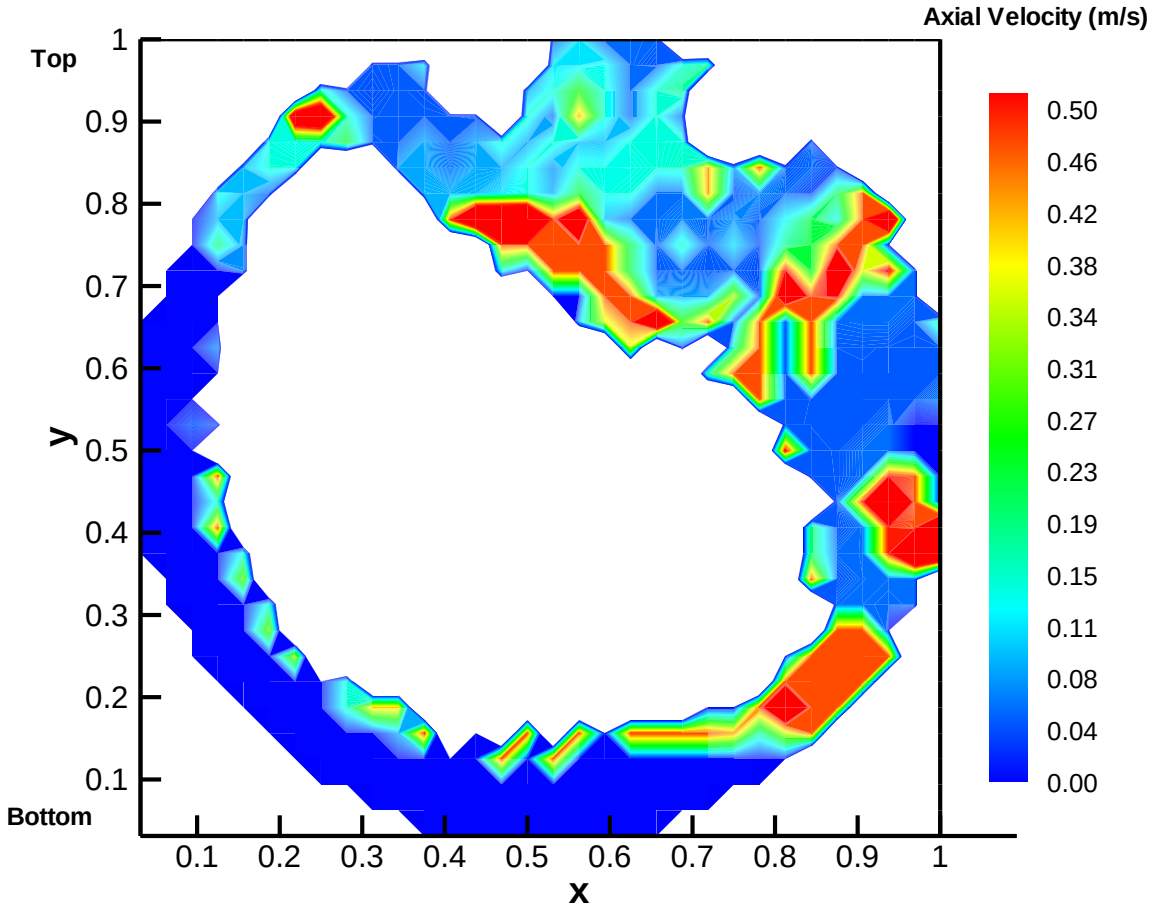

Figure 4.14 Particle axial velocity on pipe cross-section correlated from ECT data for the half-ring flow pattern (air flowrate=1000L/min, air superficial velocity 13.3m/s).

Figure 4.15 shows that there is half-ring formation around the pipe wall. The ring of particles seemed to be suspended in the air or moving with lateral velocities. From the interspaces among the particles adhered on the pipe, it is observed that a small quantity of particles in the pipe core still moved ahead in the dilute region, and the average velocity is estimated as 0.23 ± 0.06m/s using the previous method (particle B only moved a short distance during a time interval of 0.048s). On the other hand, in the dense region, some particles settled on the bottom of the pipe, for instance, particle A appears almost motionless in the three frames.

Due to the peculiar nature of the half-ring flow pattern, normalized particle velocity distributions near the pipe surface and in the core region of the pipe are presented separately in Figure 4.16. This is shown in the sketch map of the pipe cross-section (Figure 4.1 (c)), where both types of data are obtained from the correlation result from ECT measurements. From the surface velocity profile, it may be seen that the corresponding calculated velocity data points fall on the zero axes demonstrating the stagnant ring flow, except that some positive values near the top indicate a small amount of forward flow in this area. As for the inner core region, combined with the measurement from high-speed video camera, the velocities at the bottom of the pipe are zero because of the stagnant ring structure in the dense region. Some peak values indicated forward motion of a few particles in the dilute core region. Furthermore, a hollow core area around the center of the pipe is observed, emphasizing the existence of the half-ring structure. However, it may be noted at this point that velocity measurements using the PIV is difficult for this particular type of flow pattern due to blockage of the laser sheet from the system by particles adhered on the pipe walls.

In order to validate the reliability of the various methods applied for velocity measurements in this study, the values of axial velocity for the three flow patterns measured by the three different methods are listed in Table 4.1. The velocities in the dense regions are fairly similar, but in the dilute regions, data obtained via ECT and PIV seemed to contain a larger amount of noise and so a wider range of values may be observed.

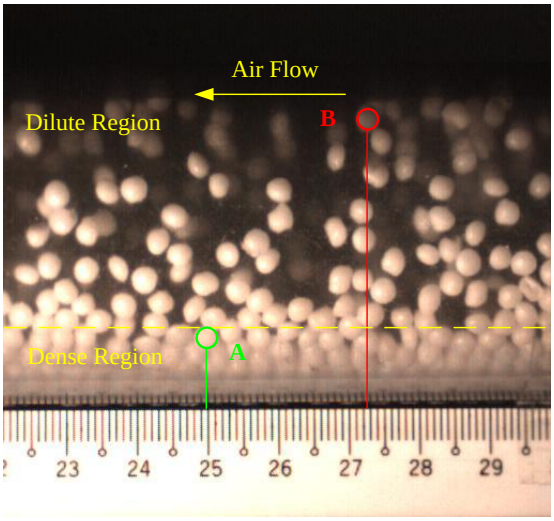

(a)

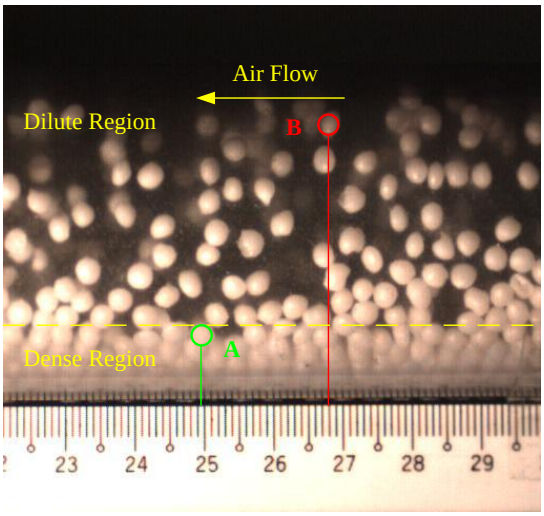

(b)

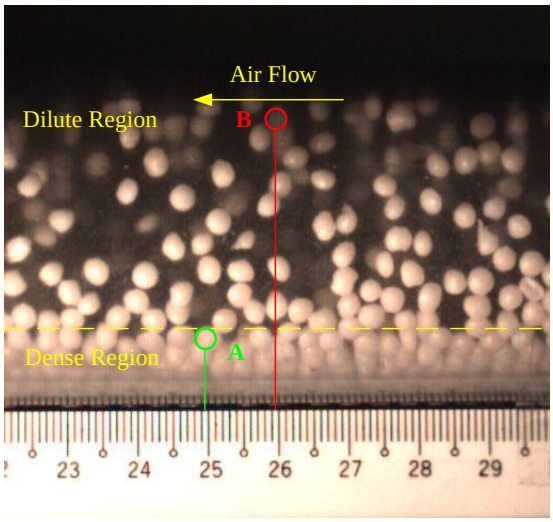

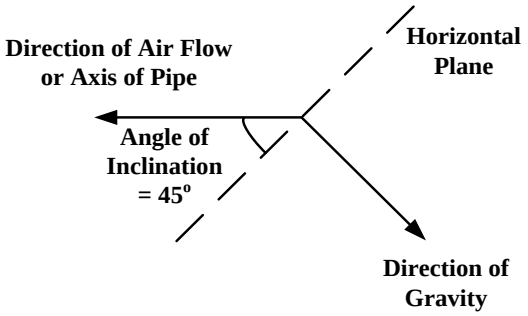

(c)

Figure 4.15 Image of particles transport for the half-ring flow pattern captured by high-speed video camera (time difference between two successive pictures=0.048s, air flowrate=1000L/min, air superficial velocity 13.3m/s).

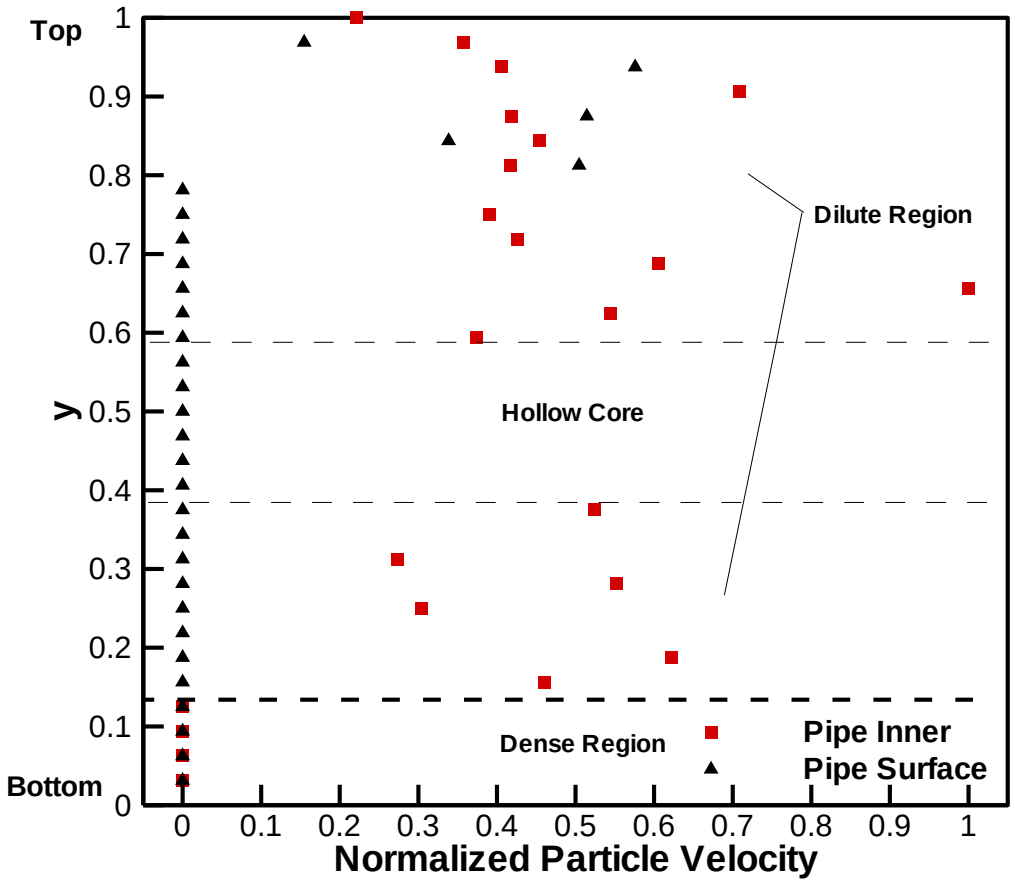

Figure 4.16 Diametrical distribution of particle axial velocity for the half-ring flow pattern (air flowrate=1000L/min, air superficial velocity 13.3m/s).

Table 4.1 Comparison of axial particle velocities by different experimental methods.

Flow pattern & air flowrate (L/min)		Flow region	Particle velocity (m/s) ECT	PIV	High-speed camera
Disperse	1600	Average	3.3×10^{-1}~1.6	1.1~3.9	1.2~2.0
Reverse	1100	Dilute	0.7×10^{-1}~3.9×10^{-1}	3.8×10^{-1}~9.0×10^{-1}	3.6×10^{-1}~8.8×10^{-1}
		Transition	-8.3×10^{-2}~0.9×10^{-2}	-3.4×10^{-2}~-1.2×10^{-2}	-7.7×10^{-2}~-3.1×10^{-2}
		Dense	-22×10^{-3}~-5.6×10^{-3}	-4.4×10^{-3}~0.6×10^{-3}	-2.7×10^{-3}~-1.3×10^{-3}
Half-ring	1000	Dilute	0.4×10^{-1}~2.6×10^{-1}	N.A.[a]	1.7×10^{-1}~2.9×10^{-1}
		Dense	0	N.A.[a]	0

[a] Velocity measured by PIV is not applicable, because laser sheet is blocked by the annular structure of particles on pipe wall.

4.1.4 Particle transverse motion from ECT results

The lateral velocities were calculated according to Equation (4.9) from ECT data and were summarized in Figure 4.17. For the purpose of consistency, lateral velocities were normalized with respect to the maximum value of axial velocity observed in the corresponding flow pattern within the pipe cross section. It is observed that the lateral velocity for both dispersed flow and reverse flow are near the zero axes. This implies that axial motion is predominant for these two flow pattern. Such phenomenon is consistent with the results shown in Figures 4.6 and 4.11. As for the half-ring flow pattern, although the trend of transverse motion seems disordered from the observation in the experiment, the values of lateral velocities are very close to that of axial velocities in amplitude. This may be attributed to the fact that particles did not travel axially due to the composite action of decreasing axial forces and increasing transverse forces exerted.

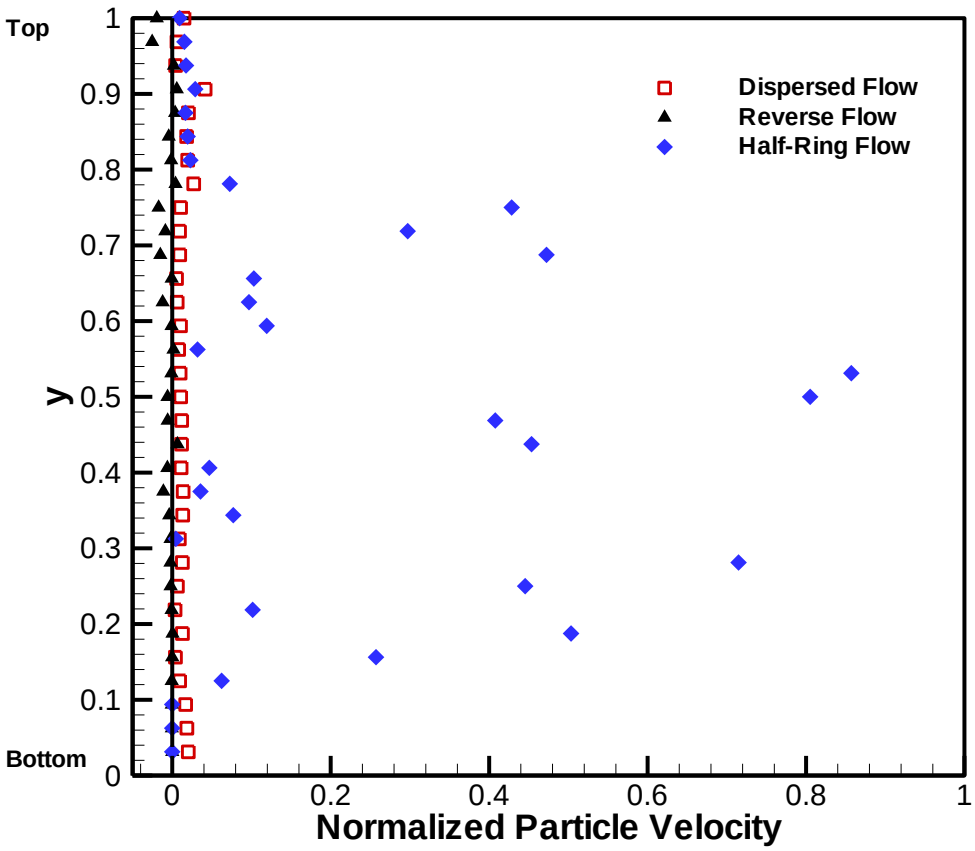

Figure 4.17 Diametrical distribution of particle lateral velocity for three flow patterns

4.2 Electrostatic and dynamic analysis for three flow patterns

In general, electrostatic effects are responsible for many anomalous behaviors in granular flow systems. It is believed that the formation of the various flow patterns described above in pneumatic conveying through inclined pipes is related to electrostatic charge generation resulting from friction, collision or rolling between particles and the pipe walls during the conveying process. In order to investigate the relationship between electrostatic effects and flow behaviors, the electrostatic charge generation characteristics for each of the above flow patterns will be discussed in the following sections.

4.2.1 Electrostatic characters for three flow patterns

In Chapter 3, electrostatic characteristics for three flow patterns have been studied by measuring the induced current on the pipe wall using an electrometer, when granular PP were transported in horizontal and vertical pneumatic conveying pipes (made of PVC). Accordingly, the charge accumulated on the pipe wall can be calculated from Equation (3.1).

Recently, Yao et al. (2006b) proposed the concepts of electrostatic equilibrium and averaged current:

$$\bar{I} = \frac{1}{T}\int_0^T I \cdot dt \tag{4.10}$$

In their opinion, averaged current fluctuated before reaching a constant value over a

period of time, namely the charging time, T_c. The periods where fluctuations occur and a steady value is reached are referred to as the charging and electrostatic equilibrium states respectively. Once the state of electrostatic equilibrium is reached, the amount of charge residing on particles and pipe wall would remain more or less constant with time. The procedure of exploring whether the average current achieves electrostatic equilibrium has been specified by Yao et al. (2006b). An equilibrium state was deemed to have been attained when the ratio of variation in average current to the average current at the final steady state was less than 10%. The charging process for three flow patterns is described in Figure 4.18 where significant fluctuations in the current were observed until the charging time, T_c was reached. The amount of charge accumulated on the pipe wall when equilibrium is reached are calculated for each of the three flow patterns according to Equation (3.1) by substituting T with the charging time and the results are listed in Table 4.2.

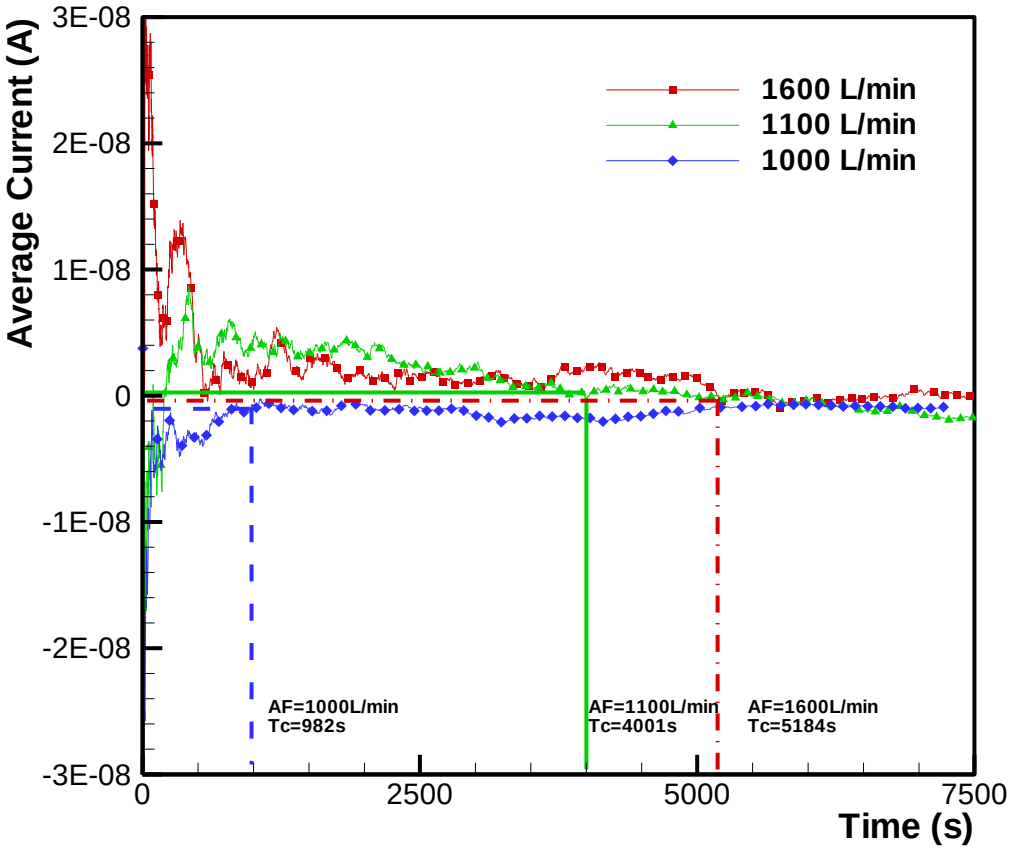

Figure 4.18 Averaged current on pipe wall for three flow patterns (AF: air flowrate; Tc: charging time).

4.2.2 Simplified electrostatic field

The electrostatic analysis in a simplified electrostatic field is shown in Figure 4.19. The schematic of electrostatic field is selected to describe as two dimensional transverse section of pipe wall in accord with the numerical work. In comparison with the characteristic length scale of the pipe, the particle is sufficiently small such that charges on the pipe wall may be taken to be uniformly distributed. The charges on the wall are assumed to be infinitesimal point charges, *dq*, and every particle is taken as a point charge, *Q* (assumption 1). By integrating the point charges over the entire wall, the electric field intensity due to charged pipe wall may be represented as follows:

$$\vec{E} = \int \frac{1}{4\pi\varepsilon_0} \cdot \frac{dq}{r^2} = \frac{\lambda}{2\pi\varepsilon_0 l} \tag{4.11}$$

here, ε_0 is permittivity constant ($8.85\times10^{-12}\mathrm{C}^2/(\mathrm{N}\cdot\mathrm{m}^2)$ in vacuum); q is the total equilibrium charge on pipe wall obtained from integration of induced current by Equation (3.1); λ is the linear charge density along pipe wall, which is defined as equilibrium charge on the pipe divided by the length of induced current measurement; r is the distance from point charge on the pipe, dq, to object point charge, Q; l is the vertical distance from pipe wall to object point charge. The detailed derivation is shown in an appendix.

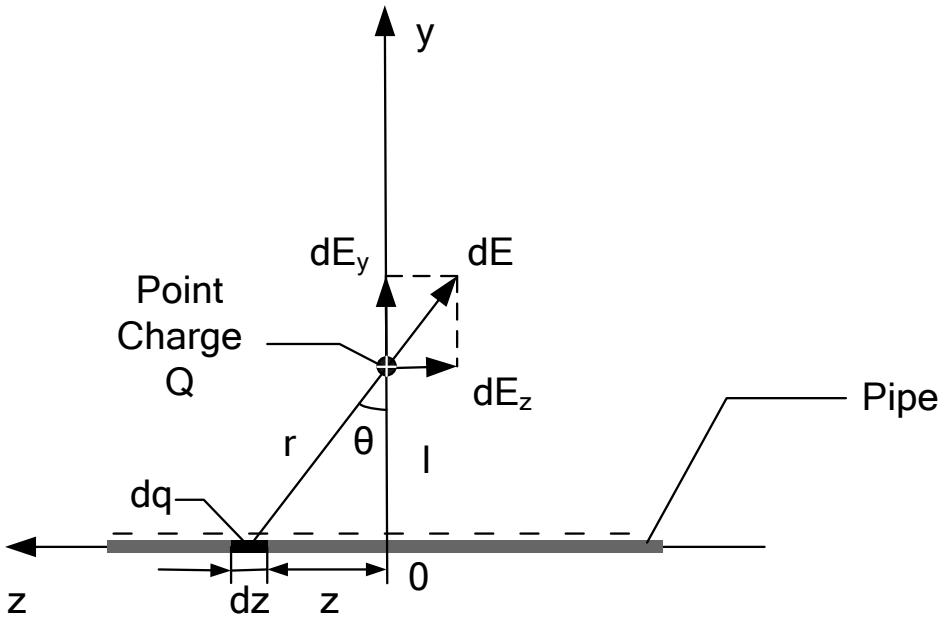

Figure 4.19 Schematic of simplified electrostatic field in the transverse section of pipe wall.

4.2.3 Dynamic analysis for single particle on pipe wall

In the above model for dynamic force analysis, electrostatic interactions between particles were not taken into consideration (assumption 2). This assumption has been verified in a previous experimental study (Yao et al. 2006b) where the electrostatic forces exerted on each particle by other particles due to the pipe wall were found to be less than 0.1% and could be neglected. A CFD-DEM work (Lim et al. 2006) also predicted that the average electrostatic force acting on each particle in similar systems was only 10^{-9}N and thus confirmed that electrostatic effects due to charged particles are negligible as compared with other types of forces. Evidence for this claim is that particle agglomeration is seldom observed in the present operation. On the contrary, clustering is prevalent for fine powders. This might be because of the fact that the electrostatic interactions among fine particles are significant due to the small size and weight.

Summarizing the above, the major forces acting on each particle therefore include the following components besides gravity, $\vec{G}_p$:

(i) Aerodynamic drag force, $\vec{F}_D$ (Sommerfeld, 2003):

$$\vec{F}_D = \frac{\pi \rho_g D_p^2}{8} c_D \cdot (\vec{u}_g - \vec{u}_p) \cdot \left| \vec{u}_g - \vec{u}_p \right| \tag{4.12}$$

where, ρ_g is gas density; D_p is particle diameter; c_D is the drag coefficient;

$$c_D = \frac{24}{\mathrm{Re}_p}(1 + 0.15\,\mathrm{Re}_p^{0.687}) \qquad \mathrm{Re_p} \le 1000 \tag{4.13}$$

$$c_D = 0.44 \qquad \text{Re}_p > 1000 \tag{4.14}$$

$$\text{Re}_p = \frac{\rho_g D_p \left| \vec{u}_g - \vec{u}_p \right|}{\mu_g} \tag{4.15}$$

where, μ_g is gas viscosity, and $\vec{u}_g$, $\vec{u}_p$ are the translational velocity vectors of gas and particle, respectively. For gas velocity distribution along pipe diameter, it observes 1/7 power law (Salmana et al. 2005):

$$\vec{u}_g = 1.22\vec{u}_{g,a}(\frac{l}{R})^{1/7} \tag{4.16}$$

here, $\vec{u}_{g,a}$ is the average gas velocity.

(ii) Electrostatic force is assumed to be mainly contributed by the lower pipe wall in this simplified model, $\vec{F}_E$:

$$\vec{F}_E = \vec{E} \cdot Q \tag{4.17}$$

where, Q is the electrical charge on each particle and can be obtained from multiplying charge-mass ratio (charge density) by mass of a single particle.

(iii) Friction between particle and pipe wall: the product of normal force and coefficient of friction, which is estimated to be about 0.56 from an internal angle of friction experiment (Chapter 5).

Table 4.2 displays the comparison of forces on a single particle for three flow patterns, where the particle velocity shown is the averaged value obtained from a high-speed video camera. For the dispersed flow pattern, the magnitude of the electrostatic force on average is only 10^{-6}N and thus can be neglected; whereas aerodynamic drag force

calculated is more than 4 times and 300 times that of gravity and electrostatic force respectively, showing that the primary driving force is indeed the drag force, which is also responsible for transporting particles upwards.

For the reverse flow pattern, the aerodynamic drag force in the dilute region was more than 10^{-4}N. This is still the dominant force as compared to gravity and electrostatic forces. This implies that particles would also move upwards in this region. In the dense region, aerodynamic drag force decreased to the same range as gravity and could not provide enough driving force to transport particles upwards; so that particles are likely to slide downwards due to the pull of gravity. However, the extents of electrostatic force and associated friction were high (~10^{-3}N). It is probable that the electrostatic force causes particles to stick to the pipe wall and friction limits the reverse speed to near zero. However, in the transition region, the magnitudes of the three kinds of forces were almost in the same ranges, indicating that particles should move either upward or downward. Some particles may be attracted to approach the dense region by electrostatic force. These particles are close to but not touching the pipe wall and flow reversely; but the reverse velocities in this region were greater than that of the bottom particles due to the absence of friction for such suspended particles. Therefore, in this region, the track of particle motion was more wave-like as shown in Figure 4.1 (b). On the other hand, some particles may still move ahead, but may collide with particles moving in the opposite direction thus resulting in such particles turning around. In general, the results appear to confirm that the reverse flow pattern is most significant in the transition region. In addition, the formation of a transition zone may be interpreted to indicate the presence of shearing instabilities at the interface between the dilute and dense regions. According to the report by Goldfarb et

al. (2002) a transition formed at the interface between a steady and a wavy state by two shearing granular flows in their experiment of two streams of identical grains flowing on an inclined chute downstream of a splitter plate.

As for half-ring flow pattern, the ratio of the three types of forces and the observations in the two regions were both similar to those of the reverse flow pattern. As such, the details of the analysis would not be repeated here. Furthermore, particle velocity was much lower because of a smaller amount of air flow rate in the dilute region and particles tended to remain stationary and form a ring structure on the pipe wall in the dense region and part of the dilute region, probably due to the force balance described previously thus the ring structure here was relatively stable during the entire transport process.

Table 4.2 Comparison of forces on single particle for three flow patterns.

Flow Pattern	Disperse	Reverse			Half-ring	
Air flowrate (L/min)	1600	1100			1000	
Air superficial velocity (m/s)	21.2	14.6			13.3	
Flow regions	Average	Dilute	Transition	Dense	Dilute	Dense
Particle velocity [b] (m/s)	1.6	6.2×10^{-1}	-5.4×10^{-2}	-2.0×10^{-3}	2.3×10^{-1}	0
Equilibrium charge on pipe [c] (C)	-3.8×10^{-8}	-1.0×10^{-6}			-7.1×10^{-7}	
Charge per particle [d] (C)	1.6×10^{-11}	2.6×10^{-11}			3.0×10^{-11}	
Gravity (N)	1.3×10^{-4}	1.3×10^{-4}			1.3×10^{-4}	
Drag force [e] (N)	6.2×10^{-4}	5.0×10^{-4}	4.1×10^{-4}	2.5×10^{-4}	4.3×10^{-4}	2.1×10^{-4}
Electrostatic force [f] (N)	1.8×10^{-6}	8.0×10^{-5}	2.3×10^{-4}	1.2×10^{-3}	6.5×10^{-5}	9.3×10^{-4}
Friction on the bottom of pipe(N)	N.A.	N.A.	N.A.	6.9×10^{-4}	N.A.	5.7×10^{-4}
F_D:G_p:F_E	345:71:1	6.2:1.6:1	3.1:1:1.8	2.0:1:9.1	6.6:1.9:1	1.6:1:7.4

[b] Particle velocity ($\vec{up}$) is the averaged value and obtained from high-speed camera.

[c] Equilibrium charge on pipe (q) is calculated from Equation (3.1), where T is charging time T_c.

[d] Charge per particle (Q) is obtained from multiplying charge density by mass of a single particle.

[e] Drag force ($\vec{F}_D$) is calculated from Equation (4.12), where c_D is 0.44.

[f] Electrostatic force ($\vec{F}_E$) is calculated from Equation (4.17).

In addition, a further experiment was carried out in order to clarify the reason why ring or half ring structure formed. This measurement is modified from the induced current test and shown in Figure 4.20 (a), where the test section is divided into two parts and the experimental data can be obtained from the top of the pipe and the bottom of the pipe respectively. The results of average currents calculated from Equation (4.10) were shown in Figure 4.20 (b), in which equilibrium times i.e. charging times (T_c) can be read as fairly similar values for two cases. Consequently, the induced currents were integrated with time to obtain the charge on pipe wall (Figure 4.20 (c)) according to Equation (3.1). It is observed that wall charge at the top of pipe is greater than that at the bottom of pipe during the entire experiment as well as at the moment of equilibrium time. Therefore, the magnitude of electrostatic force on the top of pipe is high to 10^{-3}N, thus such value would be large enough to overcome the gravity and attract particles to stick on the upper part of pipe wall. The attraction of particles to the pipe wall was primarily brought into effect by the friction on the pipe, which is opposite to the direction of particle movement, as analyzed before. Suppose that particle touched the top of the pipe wall, the absence of friction would not make the particle stick on the pipe wall. On the other hand, the friction on the side of the pipe wall prevented the particle from falling down. Therefore, it was hardly observed a completed ring structure.

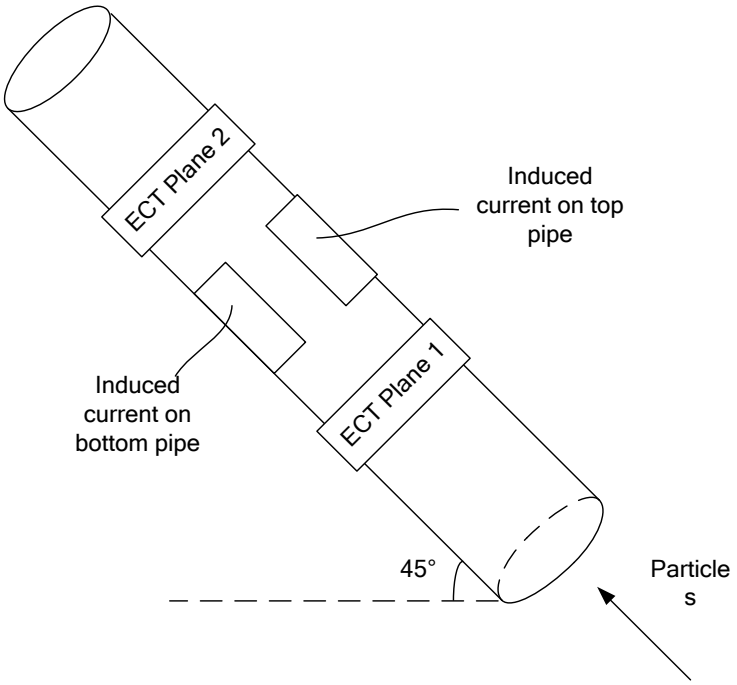

(a)

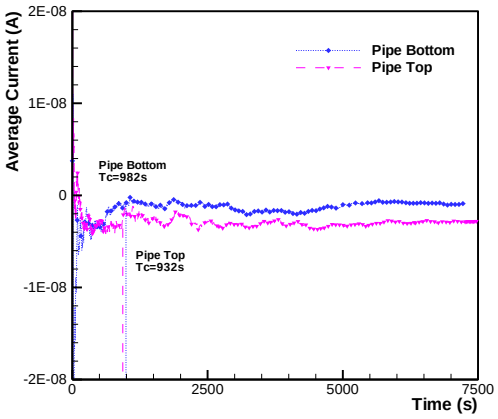

(b)

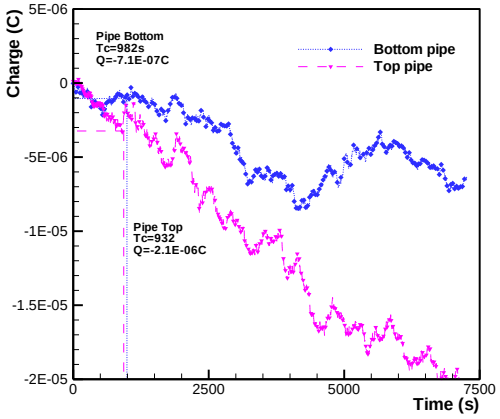

(c)

Figure 4.20 Comparison of electrostatic characters on the bottom of the pipe and the top of the pipe for the half-ring flow pattern (air flowrate=1000L/min, air superficial velocity 13.3m/s): (a) Induced current measurement section; (b) Averaged current on pipe wall; (c) Wall charge from integration of the induced current.

4.2.4 Validation of control experiments

The unique feature of the reverse flow phenomena, especially the velocity difference between the transition and dense region, is attributed to electrostatic effect as analyzed before. Thus, it is anticipated that particles on the bottom of the pipe would slide downwards with higher speed and thus the transition region would disappear, when electric force was reduced. In order to verify this postulation, control experiments, which isolate the electrostatic effect on a system by holding constant all variables but the one under observation, were carried out. A commercially available antistatic agent, Larostat-519 powder (Zhang et al. 1996), has been demonstrated to be a suitable means to reduce electrostatic effects effectively in a pneumatic conveying system (Yao et al. 2004). In this experiment, 0.5% (by weight) Larostat-519 powder was mixed with PP granules and other conditions were fixed to be the same as those for reverse flow. In comparison with previous cases where no such agent was used, the equilibrium charge on the pipe wall and on each particle obtained in the presence of the Larostat-519 powder was smaller by about 2 orders and 1 order of magnitude respectively, as shown in Table 4.3. Correspondingly, a drastic drop in electric force acting on each particle at the bottom of the pipe as well as frictional forces were observed. Under the same airflow rate (1100L/min), such small aerodynamic drag force cannot afford enough power to move particles upwards as mentioned in the last section. Consequently, particles on the bottom of the pipe slid downwards with higher velocities compared to the situation without antistatic agent, since the small electric force and associated friction would not restrict particles in this region. Furthermore, bottom particles would drive other particles in the dense region with almost the same velocities. Thus particles in the entire dense region flowed in the reverse direction.

This process was captured by high-speed video camera shown in Figure 4.21. The range of the dilute region in these three images is basically the same as that in Figure 4.10, but no obvious transition region is observed. This is because particles (A) on the bottom of the pipe and particle (B) at the interface of the dense and dilute regions are moving with almost the same speed (-0.25±0.078m/s).

Table 4.3 Electrostatic forces on single particle in the entire reverse area of inclined pneumatic conveying (air flowrate=1100L/min).

Particle	PP without Larostat-519	PP with Larostat-519
Particle velocity [b] (m/s)	-5.4×10^{-2}~-2.0×10^{-3}	-3.3×10^{-1}~-1.7×10^{-1}
Equilibrium charge on pipe [c] (C)	-1.0×10^{-6}	-5.2×10^{-8}
Charge per particle [d] (C)	2.6×10^{-11}	3.0×10^{-12}
Electrostatic force [e] (N)	2.3×10^{-4}~1.2×10^{-3}	1.3×10^{-6}~6.7×10^{-6}
Friction on the bottom of pipe [f] (N)	6.9×10^{-4}	5.35×10^{-5}
F_e/G_p	1.8~9	0.01~0.05

[b] Particle velocity ($\vec{u}_p$) is the averaged value and obtained from high-speed camera.

[c] Equilibrium charge on pipe (q) is calculated from Equation (3.1), where T is charging time T_c.

[d] Charge per particle (Q) is obtained from multiplying charge density by mass of a single particle.

[e] Drag force ($\vec{F}_D$) is calculated from Equation (4.12), where c_D is 0.44.

[f] Electrostatic force ($\vec{F}_E$) is calculated from Equation (4.17).

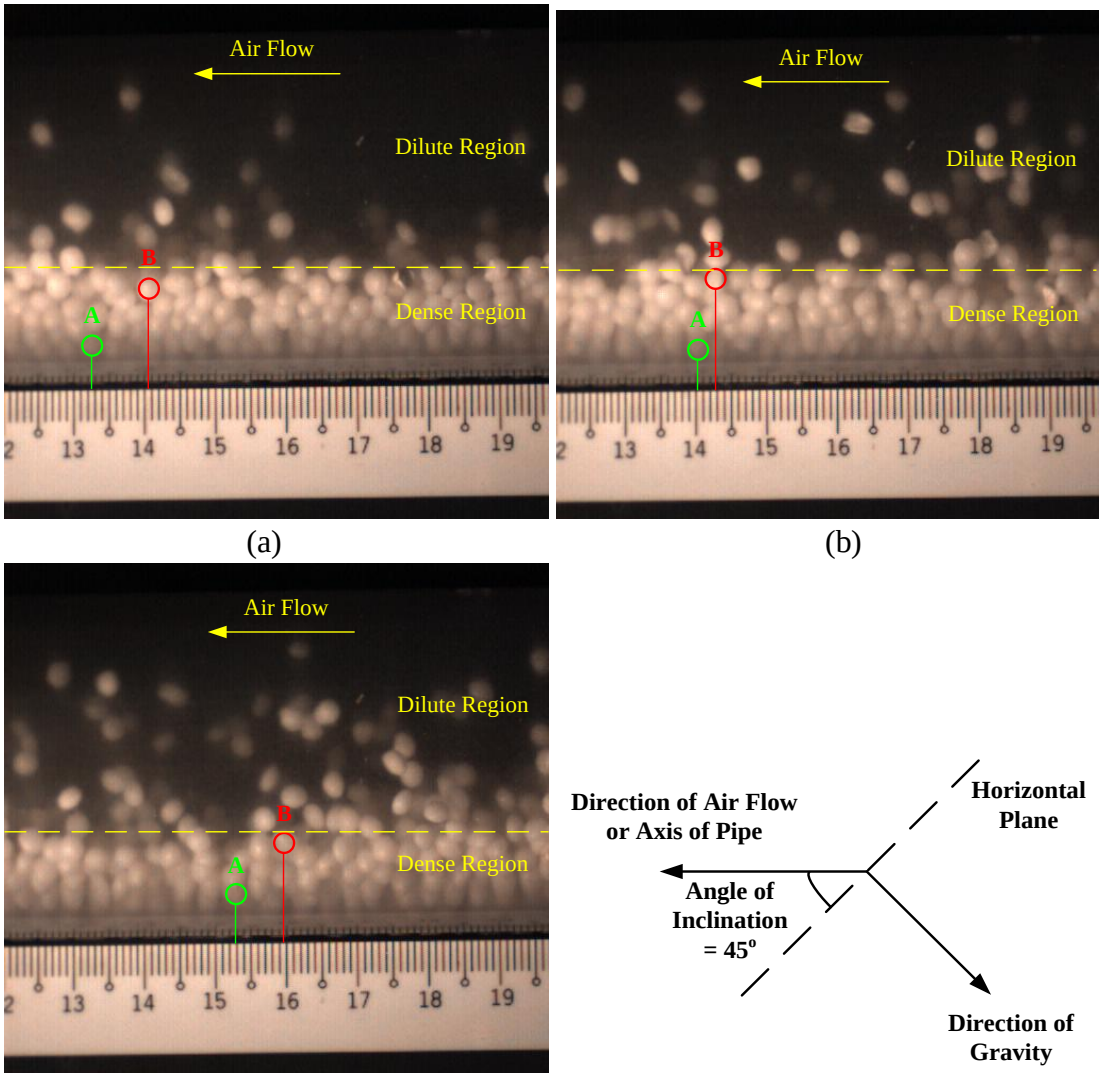

Figure 4.21 Image of particle transport for the flow pattern of PP with anti-static agent (Larostat-519 powders) captured by high-speed video camera (time difference between two successive pictures=0.088s, air flowrate=1100L/min, air superficial velocity 14.6m/s).

Furthermore, during the experimental process of reverse flow pattern without the influence of electrostatic achieved by adding the anti-static agent, it was found that particles did not slide downwards in a smooth and steady manner. Instead, from the observation made in the present study, the speed of the reversing particles showed periodic fluctuations and solids moved downwards in alternating pulses of high and low concentration as shown in Figure 4.1 (d). The slow motion captured by high-speed video camera presented this phenomenon in detail: first of all, a stream of solids flowed down at a relatively high speed from downstream to upstream along the conveying pipe; then, the reverse speed of some particles decreased; these particles blocked the ones flowing back from downstream and accumulated on the upstream side of the pipe wall making the solids stream intermittent; this continued until friction between the particles and the wall or among the particles was unable to support the gravity of the group of particles. The process was then repeated.

In conclusion, the behavior of solids motion in the dense region exhibits a pulsating type of movement. Such flow pattern can be identified by the pressure fluctuations in the conveying of solids (Dhodapkar and Klinzing, 1993). Therefore, an additional measurement was carried out to obtain the pressure data using two pressure transducers (Gems 2200BGA1002A3UA, Basingstoke, England) at locations 0.85 m and 1.85 m from the bend respectively as labeled 16 and 17 in Figure 2.3. The pressure data were acquired simultaneously for 100s with the sampling rate set at 100Hz. Figure 4.22 shows the results of the normalized signal from the two pressure transducers against time (4s). It is observed that two pressure waveforms from the two sensors are out of phase with each other with each signal having a regular period of around 1s. The time lag (Δt) between the two waves indicated the time taken for one

cluster of particles to slide from test point 1 to test point 2. The average Δt was obtained statistically as 0.5 ± 0.3s. The corresponding time lag between two particle concentration waves measured by two sets of ECT sensors was also observed to be similar in magnitude (Figure 4.22 (b). The power spectral densities for both waves were obtained by a fast Fourier Transform of the pressure and concentration data so as to have a more quantitative comparison of the dominant frequencies for both waveforms. Figures 4.22 (c) and (d) show that both power spectral density profiles exhibit a dominant peak at approximately 1 Hz. This is also consistent with the fluctuation period of 1 s as observed from Figures 4.22 (a) and (b).

Another experiment was performed for comparison and confirmation purpose by mixing antistatic agent into particles at a fixed airflow rate of 1000L/min. It was then observed that the ring flow pattern disappeared as shown in Figure 4.23.

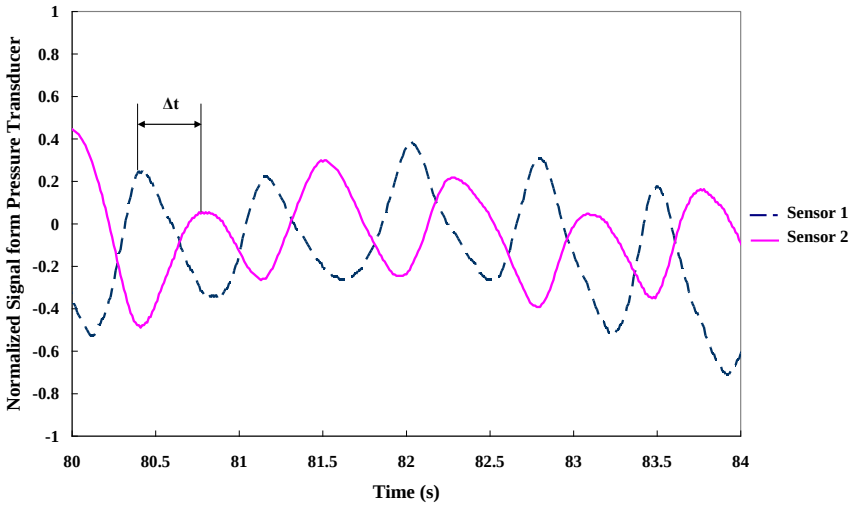

(a)

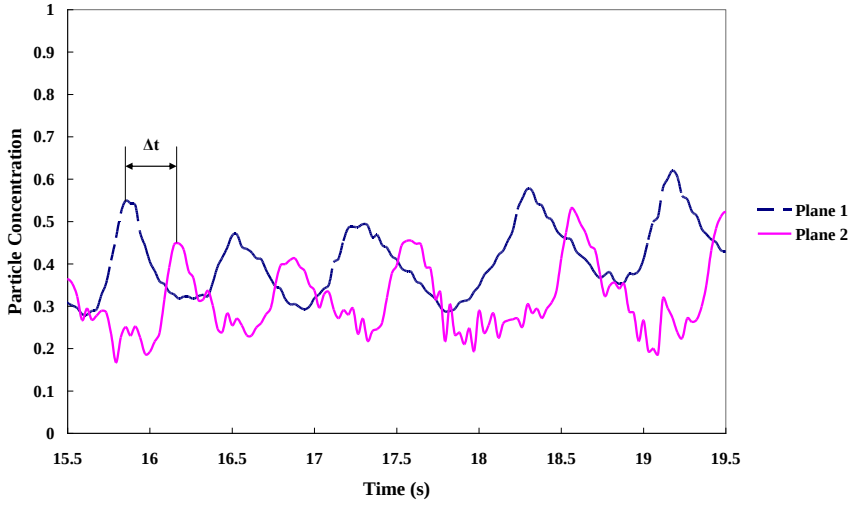

(b)

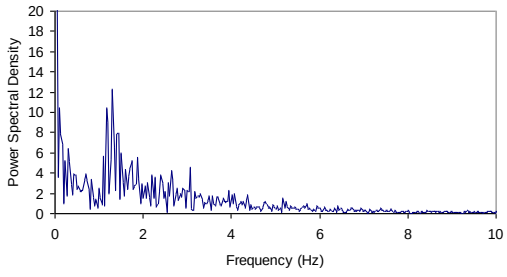

(c)

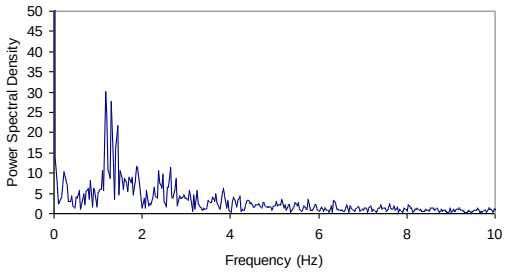

(d)

Figure 4.22 Results of reverse flow pattern with pulsating wave (air flowrate=1100L/min, air superficial velocity 14.6m/s): (a) Normalized signal from two pressure transducers against time (4s); (b) Particle concentration (α)captured from two ECT planes against time (4s); (c) Power spectral density of ECT data in plane 1; (d) Power spectral density of ECT data in plane 2.

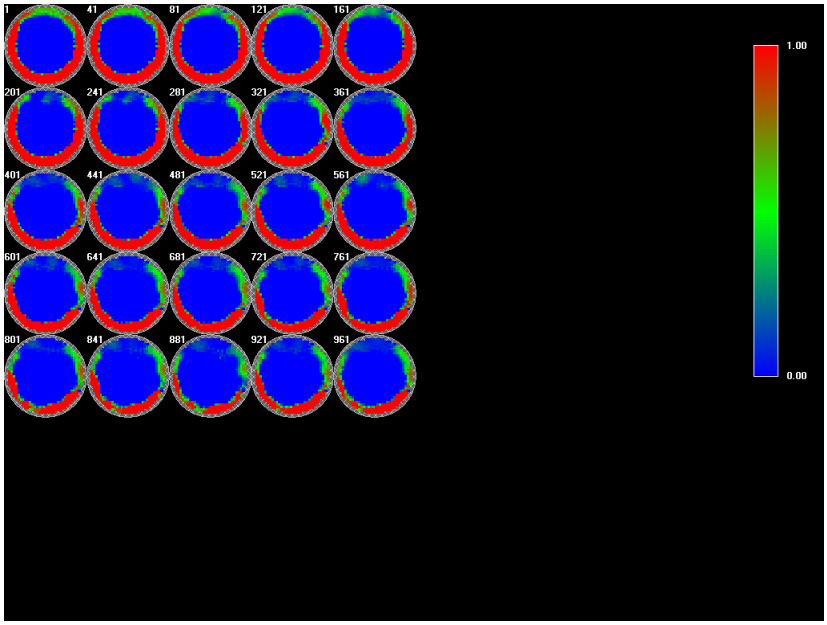

(a)

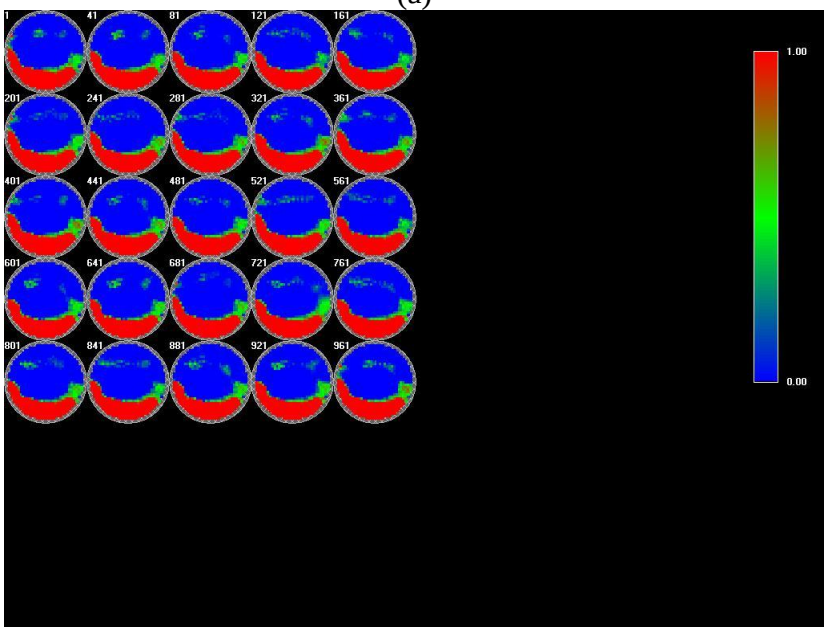

(b)

Figure 4.23 ECT images of particle concentration (α) at plane 2 when air flowrate is 1000L/min, air superficial velocity 13.3m/s: (a) Without anti-static agent; (b) With anti-static agent (Larostat-519 powder).

4.3 Concluding remarks

The concentration distribution of polypropylene particles transported in a 45 ° inclined pneumatic conveying pipe was measured using ECT. By applying the best-correlated pixel method, the characteristics of velocities and directions of particle motions in three different flow patterns were described and compared with results of PIV and high-speed video camera measurements. It is concluded that when airflow rate is high, the whole solid phase is dilute and particles are dispersed over the entire cross-section of the pipe with high velocity especially in the pipe center. In contrast at low airflow rates, most of the solid particles are deposited at the bottom of the pipe and some of them are transported in the upper part of the pipeline, forming the dense and dilute regions respectively; the corresponding velocity distribution shows the presence of reverse flow in a transition region between these two regions. When airflow rate is decreased further, a half-ring flow structure is formed and the majority of particles adhered to the pipe wall. The major forces acting on single particles were analyzed for the three flow patterns, including the drag force, electrostatic force, gravity and friction. For the dispersed flow pattern, the dilute region of reverse flow pattern and half-ring flow pattern, aerodynamic drag force was the major driving force transporting particles upwards. For the dense region of reverse flow pattern and half-ring flow pattern, the electrostatic force predominated and attracted particles onto the pipe wall. For the transition region of reverse flow, three major forces were in the same ranges and caused particles to be in a suspended state. In this region, particles would be drawn by the gravitational force to flow downwards. Thus, the electrostatic force was essential for the occurrence of three regions in reverse flow and this was

also validated by the control experiments.

Chapter 5. Granular attrition and its effect on electrostatics in pneumatic conveying systems

Particle attrition is a common phenomenon in many industries. It can result in loss of expensive materials and environmental pollution; however, it is also helpful towards the removal of impermeable components on the surface of reacting particles. Some attrition is inevitable and has been reported in a wide range of processes and industries (Bemrose and Bridgwater, 1987). The rotary valve is widely used in particulate conveying systems (Wypych et al., 2001). However, the conditions under which particles are damaged in such a valve are not well understood. In an earlier study on charge generation in pneumatic conveying systems, it was found that when airflow rate was low, particles were not transported quickly and piled up in the valve feeder. Under the action of the blades of the rotary valve, particles would be extruded and attrited. As such, breakage of particles within a rotary valve is the main focus of the present work. This chapter aims to find the attrition characteristics of granular materials in a rotary valve. Physical properties of the granular materials before and after attrition are analyzed and flow behaviours of attrited granules in a pneumatic conveying system, including solid flow rate and abrasion of the pipe wall, are studied as well. This chapter also reports on the effect of particle attrition on electrostatics behaviour and shows the relationship between particle size and electrostatic charge generation characteristics.

5.1 Physical properties of particles and their variations by attrition

In this section, attrition effects on different materials and particle behaviours in pneumatic conveying systems is described and compared.

5.1.1 Particle size and shape

In the present study, intact and attrited particles are defined according to their size ranges shown in Table 5.1. Average size and standard deviation of four types of particles are also described respectively in Table 5.1. It is observed that intact particles have a narrow size distribution while attrited particles have a wider size distribution and all kinds of shapes, for both PVC and PP samples. Undoubtedly, the average size of particles is diminishing with the occurrence of attrition.

In order to study the dependence of particle attrition and flowability on particle shape, a "shape factor" given below is introduced to describe the granular shapes (Watano and Miyanami, 1995),

$$\phi = P^2 / 4\pi \cdot S \tag{5.1}$$

where S is the projected area and P is the perimeter of this projected area. The shape factors for the samples shown in Table 5.1 were calculated from the particle size/shape analyzer. It is seen that shape factors of attrited particles have a wide spreading. Yao et al. (2006a) demonstrated that the shape factors of particles are significantly more scattered for products from the lower-sized range and this implies that the shapes of these smaller granules are made up of complex combinations of different geometries. From the appearance of attrited particles shown in Figure 5.1, it is apparent that the mechanism of attrition in the rotary valve is breakage and not

abrasion. The latter will usually result in only minute losses in surfaces, edges and corners of particles and thus can be excluded. Besides, heat influence on change of particle shape is not obvious because experiments were operated in room temperature and the process temperature everywhere in the pneumatic conveying system is much lower than the heat deflection temperatures (HDT) of PP and PVC (Table 2.3).

Table 5.1 Physical properties of particle.

Particle	PVC		PP	
	Intact	Attrited	Intact	Attrited
Size range (mm)	3.35~4.2	1.18~3.35	2.8~3.35	1.18~2.8
Average size (mm)	4.06±0.11	2.28±0.52	3.01±0.13	2.45±0.29
Shape factor	1.179±0.101	1.773±0.664	1.099±0.201	1.368±0.616
Standardized flow time (s)	0.0103	0.0115	0.0070	0.0090
Internal friction angle (α)	31.2 °	35.8 °	29.2 °	33.7 °
Friction coefficient (tanα)	0.61	0.72	0.56	0.67

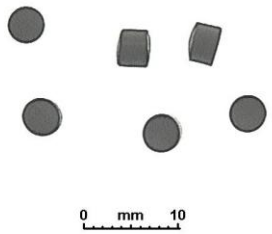

(a)

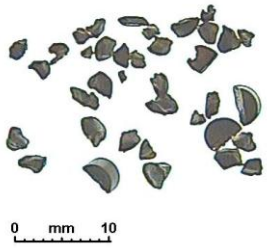

(b)

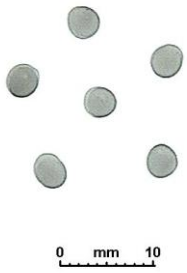

(c)

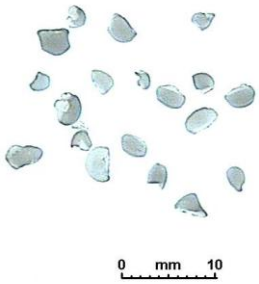

(d)

Figure 5.1 Pictures of particles: (a) Intact PVC samples (3.35mm~4.2mm); (b) Attrited PVC samples (1.18mm~3.35mm); (c) Intact PP samples (2.8mm~3.35 mm); (d) Attrited PP samples (1.18mm~2.8 mm).

5.1.2 Single particle compression test

It is known that breakage occurs when a material is stressed or compressed beyond its failure stress and single particle compression breakage strength varies with size and material properties. However, the relationship between compression test and attrition was seldom investigated. Willem and colleagues compared results from constant strain rate tests, controlled force tests and double spring compression tests where the breakage was acquired and studied in details according to force–displacement curves (Willem et al., 2003). Gorham and coworkers studied damage on PMMA spheres caused by impact and compression and observed a brittle–elastic manner on impact and plastic deformation in compression test (Gorham et al. 2003). Shipway and Hutchings presented a theoretical and experimental study of the fracture of single glass sphere between opposed platens by uniaxial compression, which is relevant to the breakage attrition of particles in granule transport, handling, processing and comminution (Shipway and Hutchings, 1993). The source of breakage of particles is mechanical action between particles and another body. In our experiments, it is the shearing actions of the blades in the rotary valve that leads to fragmentation of particles. The direction of contact, relative velocities and contact stresses between the particles and the blades, shapes of particles, and masses of samples are all important to determine the characteristics of breakage. Therefore, it is necessary to measure the relationship between load and strain of single particle.

Figure 5.2 shows the change in shape of particle before and after the compression experiment carried out according to the procedure described in Section 2.5.2. Both PVC cylinder and PP bead were compressed to the shape of a cake. The load-strain

graph is also shown in Figure 5.2 where strain, ε, is defined as the change in magnitude of a reference dimension, expressed as a ratio of axial quantitative change to the original axial height of one particle. The result of the compression test for intact particles is compared to that for attrited particles respectively for PVC and PP in Figure 5.2. Apparently, the curve for attrited particles appears gentler than that of intact ones, both for PP and PVC, showing that the maximum load that attrited particles can withstand decreases as the size of particle decreases. This seems to imply that once a particle is broken, it would be attrited much more easily even under a smaller applied stress. Antonyuk et al. (2005) demonstrated that the highest local tensile stress is generated at the crack release zones in the granules, such as pores and structural defects and the fracture initiates from this zone. Previously Willem et al. (2003) also reported that the breakage could occur at lower forces due to particular fatigue shown in fatigue curves where the percentage of broken particles were plotted as a function of the compression stress and the number of repeated cycles.

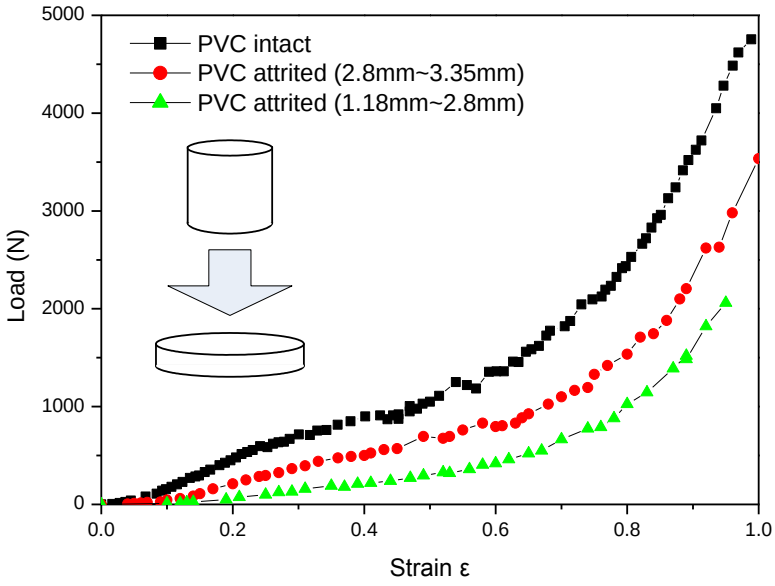

(a)

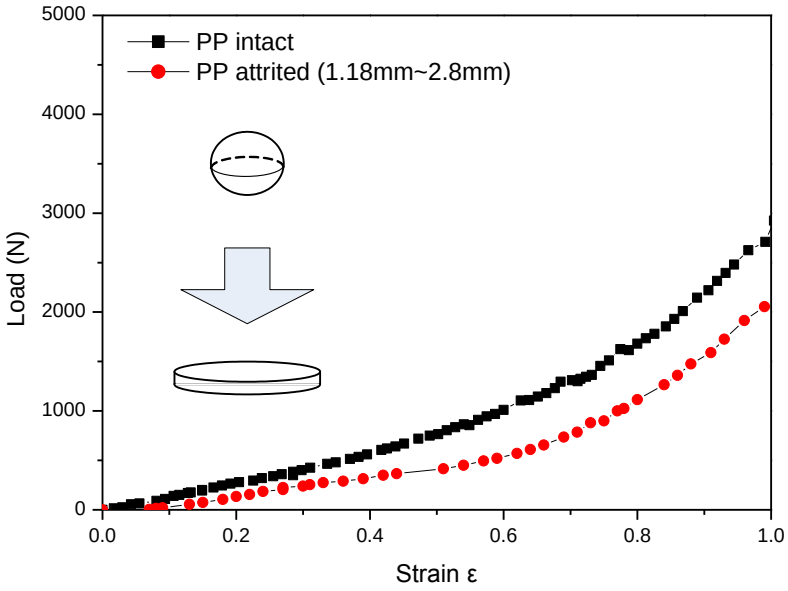

(b)

Figure 5.2 Single particle compression test: (a) PVC cylinder; (b) PP bead.

5.1.3 Granulate test and solid flow rate in pneumatic conveying systems

In pneumatic conveying systems, attrition may be related to the flowability of the impacting bodies. In our experiment, attrition is more likely to occur at low flowability because particles with poor flowability usually accumulate in the rotary valve and are then subjected to the shearing actions of the blades in the valve. In all granulate tests performed, the flow time was calculated according to Equation (5.2):

$$Flow \quad Time = \frac{measured \quad test \quad time \quad in \quad seconds}{weighed \quad sample \quad in \quad grams} \tag{5.2}$$

Flowability usually depends primarily on particle size, shape and bulk density. Table 5.1 shows that the flow time increased slightly after the occurrence of particle attrition. This may be due to a strong dependence of flow time on the shape of particles, as the observed widespread shape factor corresponds very well with the fact that attrited particles become much more irregular in shape than original particles. Many researchers (Teunou et al., 1999 and Fitzpatrick et al., 2004) have demonstrated that the flowability of particles reduced with decreasing granular size. Fitzpatrick et al. (2004) investigated 13 food powders and showed that flowability tended to reduce with decreasing particle size. They explained that as particle size decreased, particle surface area per unit mass increased, correspondingly, the greater surface cohesive forces led to more cohesive flow. They also found that the flowability was influenced by the combination of particle size and moisture content and varied only weakly with increasing densities. In our experiment, the particle density of PP is lower than that of PVC (Table 2.3). Upon comparing the two different kinds of particles, the flowability of PP beads is much better than that of PVC cylinders for both intact and attrited samples. However, this may be attributed more to the shape than density of particles.

It is noted that PP beads are ellipsoidal but PVC particles are cylindrical.

In the pneumatic conveying system, the flowability of particles would affect the solid flow rate. When airflow rate was fixed at 1600L/min, three different cases may arise according to the level of feed valve opening: 75%, 100% and flood-fed condition (valve removed from the inlet of rotary valve and replaced by a 75mm-ID pipe). Particles with poor flowability, such as PVC samples, would not move smoothly in the systems, and would tend to stick on the hopper and be locked in the rotary valve, even with a valve opening of up to 100%. They can be transported smoothly only in a flood-fed condition, for both intact and attrited samples, giving solid flow rates of 37.62 ± 4.76g/s and 37.49 ± 6.79g/s respectively. In contrast, PP samples would generate a strong electrostatic discharge, making the experiment dangerous in this case. Therefore, it was deemed more appropriate for experiments involving both intact and attrited PP to be performed at 75% feed valve opening with respective solid flow rates of 40.67 ± 3.29g/s and 40.05 ± 0.63g/s. These optimal operating conditions for both PP and PVC samples and the corresponding solid flow rates obtained are listed in Table 5.2. Therefore, it is demonstrated that the better the flowability of particles, the greater the solid flow rate. PP samples have better flowability than PVC samples, and intact particles show better flowability than attrited ones. The above observation is consistent with the flowability of particles measured in the granulate test.

Table 5.2 Comparison of solid flow rates.

Particle	PP		PVC	
	Intact	Attrited	Intact	Attrited
Solids feed valve	75% opening		Flood-fed	
Solid flow rate (g/s)	40.67 ±3.29	40.05 ±0.63	37.62 ±4.76	37.49 ±6.79

5.1.4 Shear strength test

Internal friction angle is a measure of granular friction between the particle layers. This parameter is important in designing pneumatic conveying systems as particles with higher internal friction angles can form larger granular piles. In this study, it would be used to characterize the flow behaviour of particles and differences between intact and attrited particles. This is because internal friction and cohesion are both surface interactions to resist powder flow (Fitzpatrick et al., 2004). From the experimental data obtained, Mohr's circles were plotted as shown in Figure 5.3. It represents the state of effective stress at failure; the diameter is defined by points, which represent the major and minor effective principal stress at failure respectively (BS1377, British Standards Institution). By drawing a tangent line to the Mohr's circles, the internal friction angle, β, of the four kinds of particles are obtained (Figure 5.3). The friction coefficients ($tan\beta$) of the granules are listed in Table 5.1. The smaller values of internal friction angle and friction coefficient of intact PP samples show that the flowability of PP granule is better than that of PVC, which agrees well with the granulate test result. This will also imply that PVC granules can form larger piles than PP granules. As for the attrition effect, it is observed that the internal friction angles increase after particle attrition, both for PP and PVC samples. This shows that friction among particles is enhanced by attrition, leading to the reduced flowability of attrited particles. For illustration purpose, all physical properties of particles, as well as their variation due to attrition, are summarized in Table 5.1.

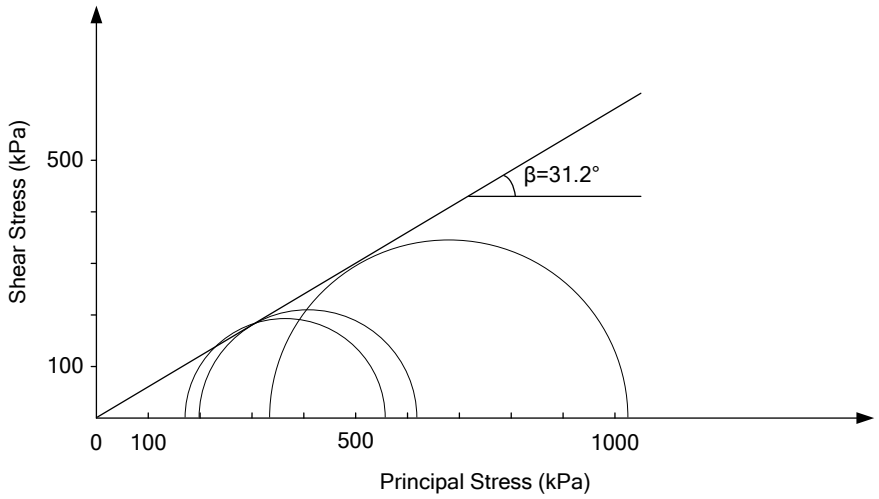
Shear Stress (kPa)
500
100
β=31.2°
0
100
500
1000
Principal Stress (kPa)

(a)

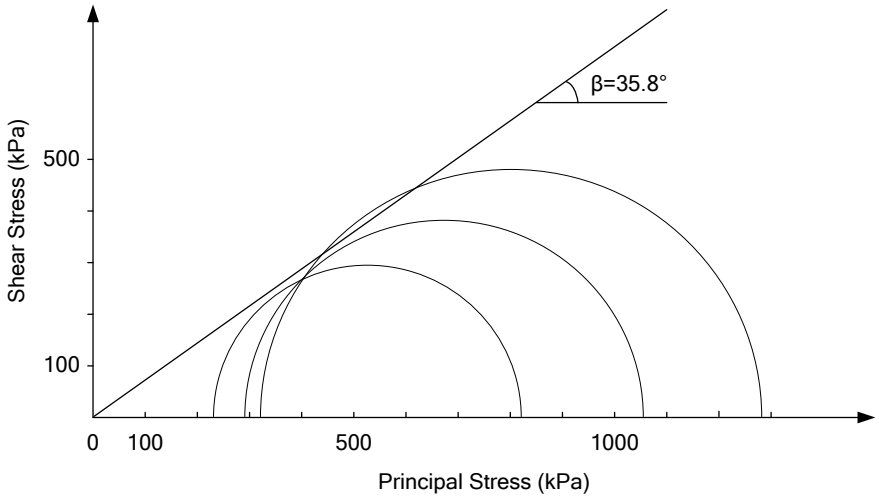
Shear Stress (kPa)
500
100
β=35.8°
0
100
500
1000
Principal Stress (kPa)

(b)

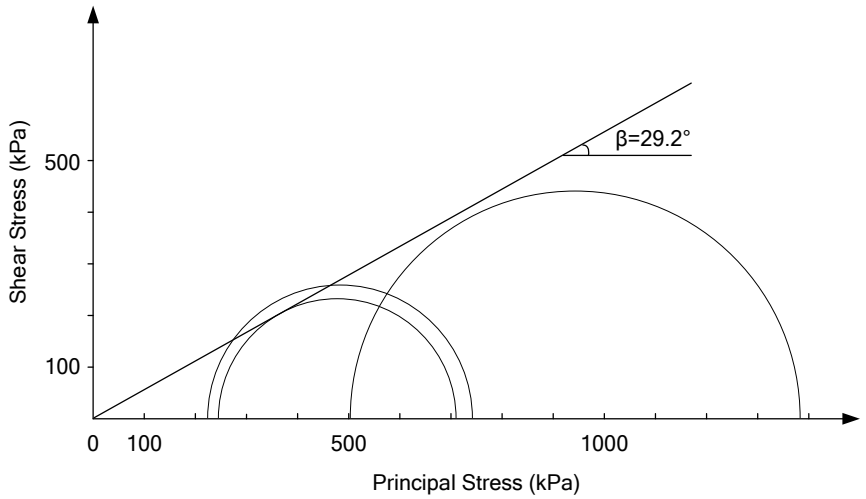

(c)

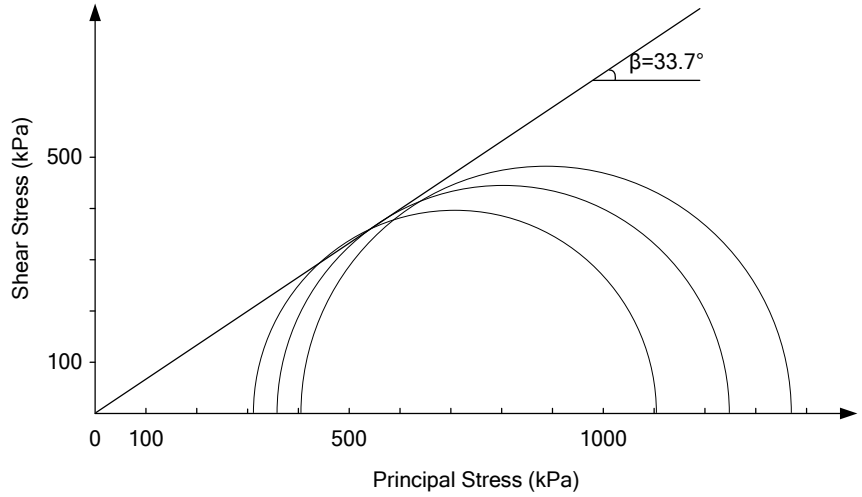

(d)

Figure 5.3 Mohr's Circle of specimens in shear strength test: (a) Intact PVC samples (3.35mm~4.2mm); (b) Attrited PVC samples (1.18mm~3.35mm); (c) Intact PP samples (2.8mm~3.35mm); (d) Attrited PP samples (1.18mm~2.8mm).

5.2 Particle attrition due to rotary valve in pneumatic conveying systems

As discussed in Section 5.1, changes in properties of granulate materials resulting from attrition are important. Particle sizes become smaller in the process of attrition due to abrasion of fine powders from larger particles and formation of larger fragments due to breakage. In the experiment of attrition solely in rotary valve, 939g PP and 745g PVC were put into the valve cavity (with the labeled height of 70cm in Figure 2.5 (a)) and were allowed to undergo attrition in the rotary valve for different time intervals. These particles were piled up in the valve cavity and the height of pile just touched the blades of valve. If the loading of particles was too low or too high, particles would not be in contact with the blades or would block the running of blades respectively and make the experiment dangerous. Similarly, in order to keep the experiment results consistent, the weight of particles was fixed in all tests of attrition due to rotary valve in the conveying system. In this part of the study, intact particles will first undergo breakage to form fragments and then abrasion to produce a finely dispersed product in the rotary valve. The rotary valve was operated either as a stand-alone device or as part of a pneumatic conveying system. Granular attrition normally occurs at the exit of the rotary valve in the former situation depicted as attrition II in Figure 2.5 (a), while in the latter, from the observations made in the present study, attrition may happen mainly at the entrance (shown as attrition I in Figure 2.5 (a)). When particles were flowing down from the hopper to the rotor pocket, they would first experience the extrusion by the rolling vanes at the entrance of valve. As particles were carried all the way to the exit of valve, air with high flow rate rapidly conveyed particles to the pipe system, thus particles accumulation and

attrition at the exit of valve could be minimized. In particular, the size of space between the vanes and casing wall at the entrance and exit varies from a maximum to a minimum during one cycle of rotation. When granules with poor flowability, such as PVC samples, are passed into the rotary valve, the accumulation of particles would result in severe attrition of the granular materials at these positions. Attrition is always accompanied with loud noises and violent shaking of the rotary valve, which plays an important role in causing granular attrition in a typical pneumatic conveying system. To some extent, granular attrition may also be brought about by direct impacts between the granules and vanes of the rotary valve or other granules (Konami et al., 2002).

5.2.1 Attrition solely in rotary valve

The PP or PVC samples after attrition can be divided into two or three sieve cuts. The particle size distribution after attrition in the rotary valve is presented in Figure 5.4. Here, mass fraction ($d\Phi$) is defined by the ratio of mass in one size range to the total mass of particulate samples. It is observed that the mass of both PVC and PP samples with the initial average size of intact particles decrease with time. In contrast, those of other sieve cuts increase slowly. Moreover, the speed of such variation for PVC samples is faster than that for PP samples. Thus, it seems that PVC is more attritable than PP due to lower flowability.

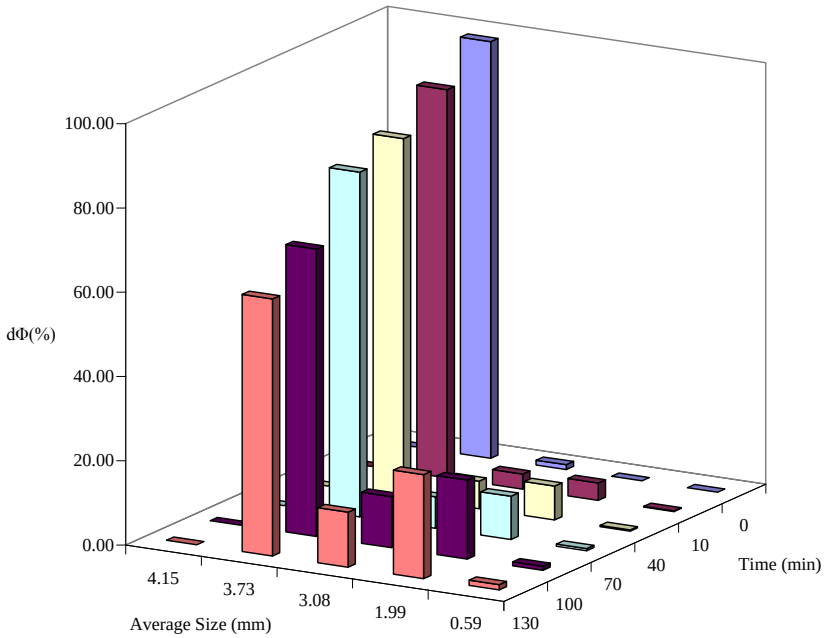

(a)

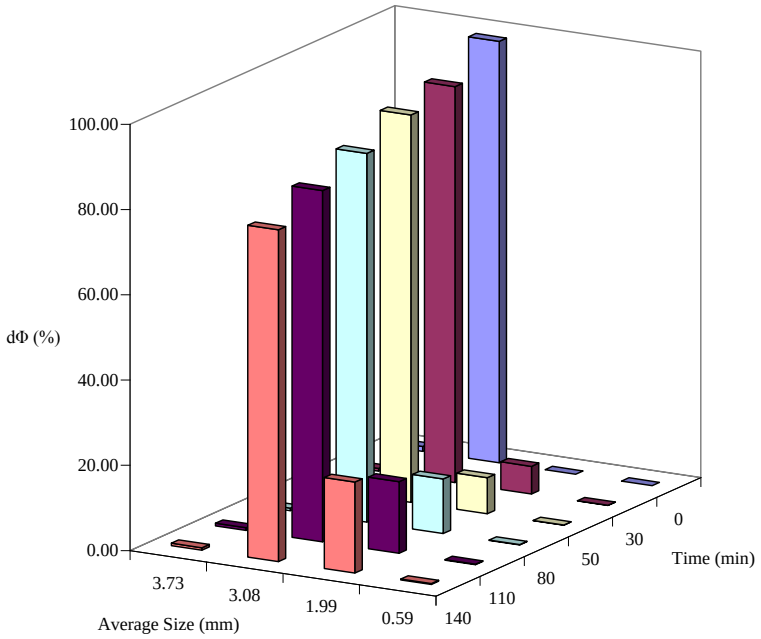

(b)

Figure 5.4 Particles size distribution solely in rotary valve: (a) PVC samples; (b) PP samples.

5.2.2 Attrition by rotary valve in pneumatic conveying systems

Figure 5.5 shows the size distribution resulting from attrition occurring in a pneumatic conveying system. The same trend with regards to decrease in amount of particles having the initial average size of intact particles and slow increase in that of particle fragments is observed for the PVC samples. Remarkably, the size distribution of particles after 1080min of attrition is very similar to that of particles after 360min. The quantities of particles with initial size decrease minimally from 63.0% to 61.4% during the period from the 360th min to the 1080th min, while those of broken particles with smaller size range basically remain the same in these 720min. It seems that 360min is the approximate time scale for the attrition process to be complete and a longer duration beyond this time has no obvious effect on the particle size distribution (Figure 5.5 (a)).

As for PP samples, the particle size distribution at different times exhibit minimal change as shown in Figure 5.5 (b). At the end of 360min, the percentage of intact PP particles is 83.7% while that of PVC particles is only 63.0%. Moreover, very little fine powders of PP (only 0.03%) are generated even after a long attrition time. It may thus be concluded that PP particles are more difficult to be attrited than PVC, as indicated previously in Section 5.2.1.

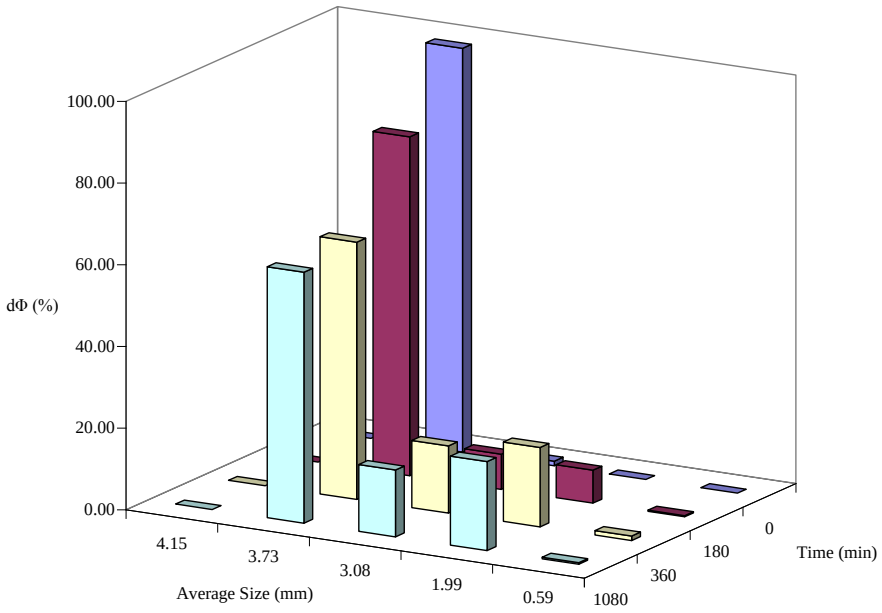

(a)

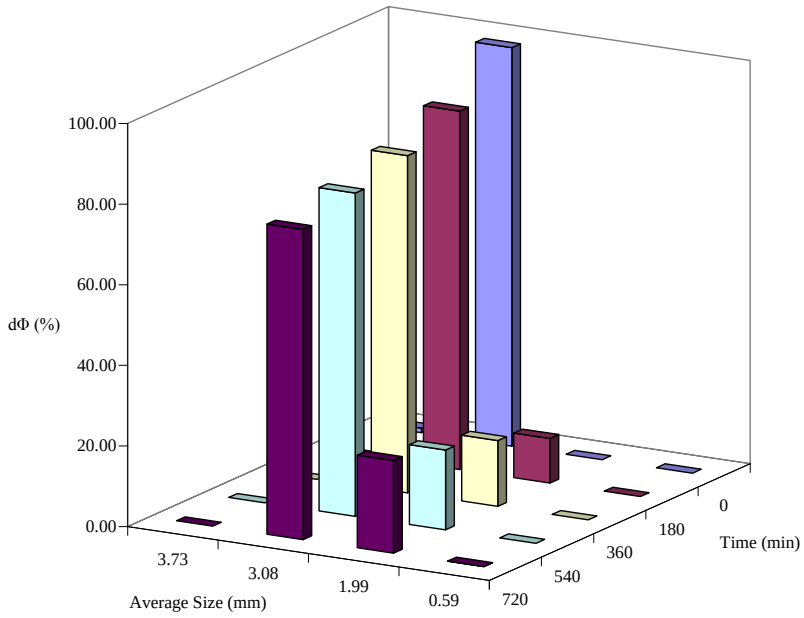

(b)

Figure 5.5 Particles size distribution in pneumatic conveying systems: Mass of samples: PVC-745g, PP-939g; Airflow rate: 1600L/min; Air superficial velocity 21.2m/s; Flood-fed solids. (a) PVC samples; (b) PP samples.

Compared to Figure 5.4, the resulting size distribution after attrition in a pneumatic conveying system in Figure 5.5 is quite similar to that in a rotary valve operating alone. In the former, both PVC and PP particles pile up in the rotary valve for only one third of time in each circulation through the system. The effective time for particle attrition by the rotary valve is calculated to be around 60min in each 180min operation and the remaining time (120min) is the duration of particle transport in systems. That is the reason why similar particle size distributions are obtained despite longer attrition times in the latter. The above reasoning demonstrates that the attrition process in pneumatic conveying system is mostly attributed to rotary valve rather than conveying pipe.

When granules enter the pocket between the two vanes of the running rotary valve, a granular pile is built up (Figure 5.6). Once the granular pile reaches a certain height, granular attrition occurs between the vanes and casing wall at the entrance of the rotary valve. Many researchers have studied such problems involving granular pile (Komatsu et al., 2001) and associated conditions (Mueth, 2000). The angle of repose of such granular piles is determined by several factors, such as particle size (Carstensen and Chan, 1976), sliding friction coefficient and rolling friction coefficient (Zhou et al., 2001) etc. Sliding or rolling friction coefficients are affected by the shape and type of material of particles, so that these would also affect indirectly the attrition process. Granular materials with low flowability usually have a large angle of repose and form tall heaps. When this occurs in a rotary valve, the granular material would undergo severe attrition. On the other hand, granular materials with high flowability, or correspondingly low angle of repose, would be transported along with the moving vanes of the rotary valve and so avoid attrition. In

the present study, both granulate and shear strength tests showed that PP samples had better flowabilities than PVC samples. Thus, the flowability of granular materials is likely to be the primary reason for the higher attritability of PVC than PP. This is in spite of the fact that the former has higher particle hardness (PVC: R113, PP: R90).

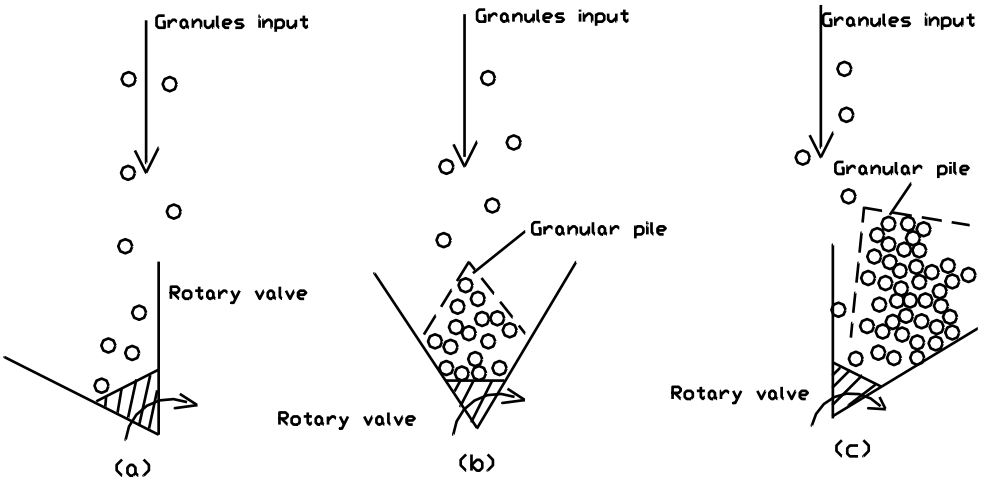

Figure 5.6 Shape of granular piles in the rotary valve pocket: (a) Initial state; (b) Intermediate state; (c) Final state.

5.2.3 Gwyn power law approach

It has been found that a convenient way to describe the size distribution of the product is written as a Schuhmann function (Schuhmann, 1940):

$$W = W_T \left(\frac{\mathrm{D_p}}{\mathrm{D_{pT}}} \right)^G \tag{5.3}$$

Here, D_p is the particle diameter, D_{pT} is the initial particle diameter and G is an exponent characterizing the size distribution. Size analysis is performed by sieving with the initial material having a narrow size distribution and held on a sieve of size D_{pT}. W is the mass of the attrited sample that has a size less than D_p and W_T is the mass of the attrited sample having a size less than $D_{p\,T}$.

Gwyn proposed a means of describing attrition and stated that the attrition of initially monodispersed particles could be described empirically by (Gwyn, 1969):

$$\mathrm{X} = Kt^m \tag{5.4}$$

where X is fraction of the initial feed that has undergone attrition at time t and m is an empirical constant; K is another constant, which he argued is a function of initial particle size. Based on Equation (5.4), the fractional degradation of the initial feed size fraction (X) is defined by the ratio of W_T to the mass of the material at the start of the experiment. In the rotary valve experiments the relationship between X and time t is found to be characterized by the Gwyn function (Figure 5.7) and the averaged values of the Gwyn parameters are summarized in Table 5.3. In this case, a linear relationship is found between lnX and lnt. In general, the Gwyn formulation is more successful in describing attrition. It may be concluded that K represents the severity of attrition and the initial attritability of a material, while m deals with the change in

material with time (Neil and Bridgwater, 1999). The values of *m* for the same particles are not very uniform between attrition occurring solely in a rotary valve and that in the pneumatic conveying system. This may be attributed to variations in experimental conditions, including airflow rates and solid flow rates. Combined with the analysis of size distribution, it is seen that PVC particles degrade more rapidly than PP particles and PP particles are substantially more resistant to attrition. Besides, it is found that the Gwyn functions were more reliable for the former two cases. Attrition would lead to the loss of fine powders worn from particles when particles were conveyed in the system. Such loss would result in the calculation deviation for *X*, thus the data points in Figure 5.7 (b) seem scatter than that in Figure 5.7 (a).

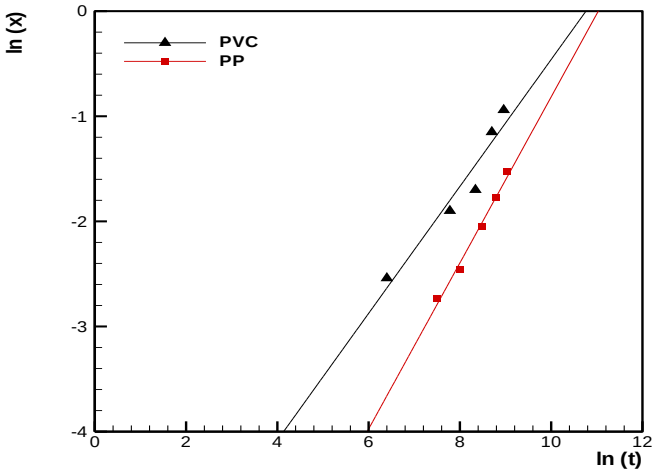

(a)

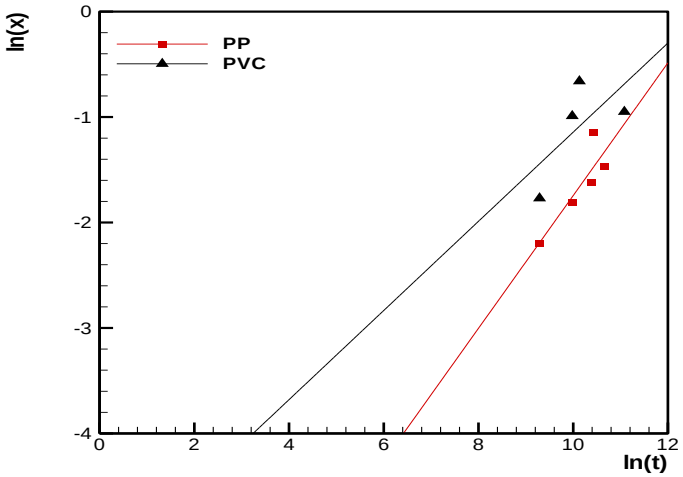

(b)

Figure 5.7 Gwyn plot from rotary valve attrition (t in second): (a) Attrition solely in rotary valve; (b) Attrition in pneumatic conveying systems: Mass of samples: PVC-745g, PP-939g; Airflow rate: 1600L/min; Air superficial velocity 21.2m/s; Flood-fed solids.

Table 5.3 Summary of parameters from Gwyn function.

Attrition	Sample Material	Parameters from Gwyn function	
		m (-)	$K/10^{-3}$ (s^{-m})
Solely in rotary valve	PVC	0.60	1.52
	PP	0.79	0.17
In pneumatic conveying systems	PVC	0.42	4.63
	PP	0.63	0.32

5.3 Effect of particle attrition on pneumatic conveying systems

Attrition has a number of different effects, the importance of which should be judged using the appropriate technical criteria in the following sections.

5.3.1 Effect of particle attrition on electrostatic characteristics

In the present study, attempts have also been made to analyze the induced current for the four kinds of particles described above. The induced current of PP samples detected at the horizontal pipe is illustrated in Figure 5.8. It can be seen that the induced current fluctuates with time and is a composite value resulting from a balance between the electrostatic charge on the particle surface and the pipe wall. Figure 5.8 (a, b) shows that the magnitude of the induced current decreases with decreasing particle size. Furthermore, in order to eliminate the fluctuation caused by negative and positive values, induced currents, *I*, were integrated with time according to Equation (3.1) to obtain the charge *q*. Figure 5.8 (c) shows that the charge *q* increases linearly with time up to 10000s. It is observed that the rate of charge accumulation on the pipe wall caused by intact PP particles is larger than that by attrited particles.

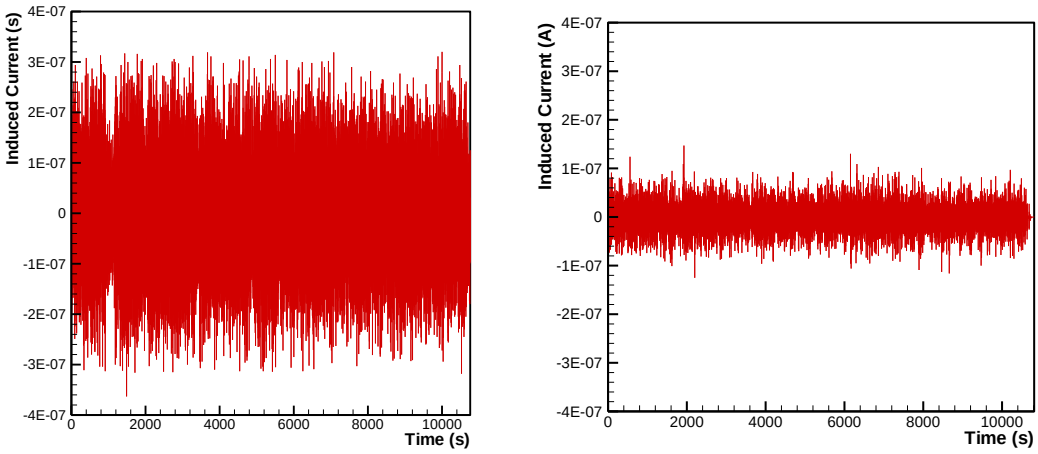

(a)

(b)

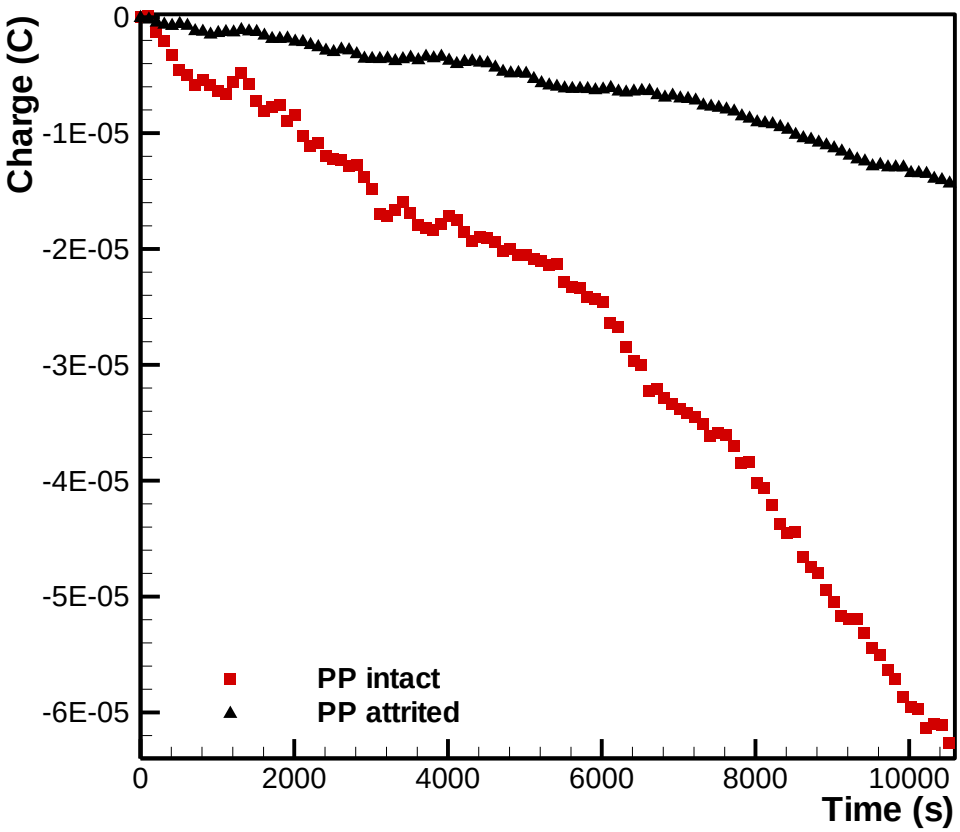

(c)

Figure 5.8 Induced currents of PP samples generated on pipe wall: Mass of samples: 939g; Airflow rate: 1600L/min; Air superficial velocity 21.2m/s; Solids feed valve: 75% opening. (a) Intact samples (2.8mm~3.35 mm); (b) Attrited samples (1.18mm~2.8mm); (c) Charges obtained by integration of induced currents.

The induced currents for intact and attrited PVC samples in the horizontal pipe segment were similarly measured using the electrometer. Figure 5.9 shows that the amplitude of fluctuations in the induced current decreases with decreasing particle size: the fluctuation observed with intact samples is about $\pm 1.8 \times 10^{-7}$A (Figure 5.9 (a)) while that with attrited particles is about $\pm 0.8 \times 10^{-7}$A (Figure 5.9 (b)). This can also be deduced from variations of the total accumulated charge on the pipe wall obtained by time integration of the data presented in Figure 5.9 (a, b). Figure 5.9 (c) shows that the rate of charge accumulation is larger for larger particles and vice versa. It is observed that the curves for both intact and attrited PVC samples exhibit fluctuations between positive and negative values. This may be due to the particles and pipe wall being made of the same material, PVC (polyvinyl chloride), resulting in charges of either positive or negative polarities being induced on the surface of the particles and pipe wall. Furthermore, due to the fact that PVC is prone to attrition, the particles were broken in the rotary valve during the experiment and this might have led to more complex electrostatic charge generation characteristics.

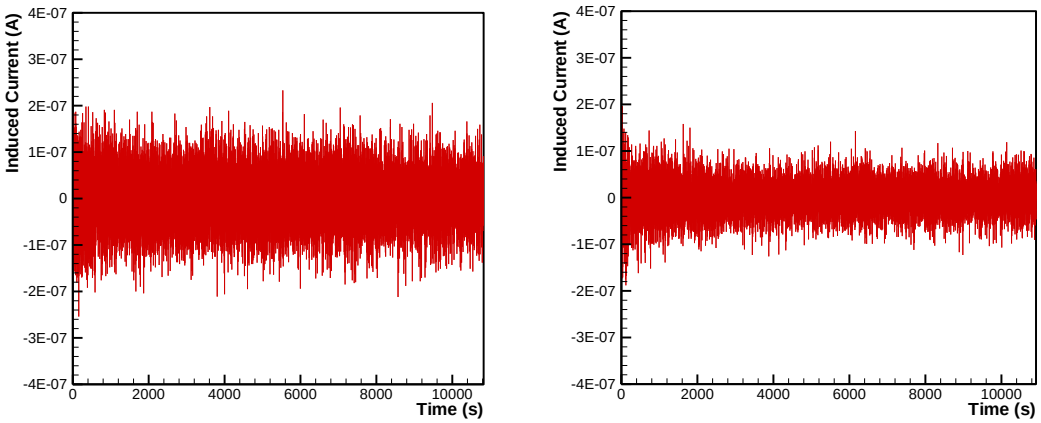

(a) (b)

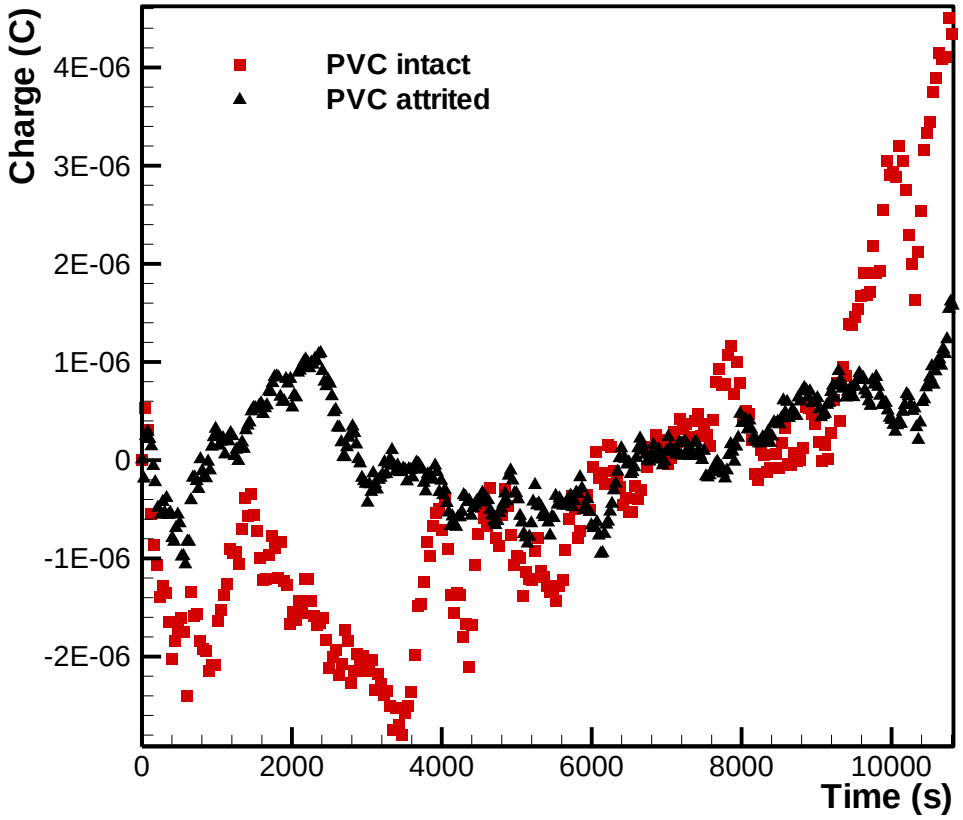

(c)

Figure 5.9 Induced currents of PVC samples generated on pipe wall: Mass of samples: 745g; Airflow rate: 1600L/min; Air superficial velocity 21.2m/s; Flood-fed solids. (a) Intact samples (3.35mm~4.2mm); (b) Attrited samples (1.8mm~3.35mm); (c) Charges obtained by integration of induced currents.

The variation of particle charge density, obtained from Faraday cage, with respect to time for PP and PVC samples is illustrated in Figure 5.10. It can be seen that particle charge densities of attrited PP are larger than that of intact ones. Similarly, the charge density of attrited PVC samples is also greater than that of intact particles. Notably, the charge density of PVC samples is negative and will be further analyzed in Section 5.3.3. In the conveying system, electrostatic charge is generated from the collision, rolling and sliding between particles and pipe wall. Consequently, the degree of particle-wall interaction would determine the rate of charge generation. For a given quantity of particles, the numbers of attrited particles were apparently more than those of intact ones; as a result, the enhanced chance of particle-wall interactions lead to the increase of charge on particles. Choi and Fletcher (1998) demonstrated that the contribution of small particles to particle space charge is more important than that of large particles. In their formulation, particle charge density depended on the total surface area of particles which was higher for small particles.

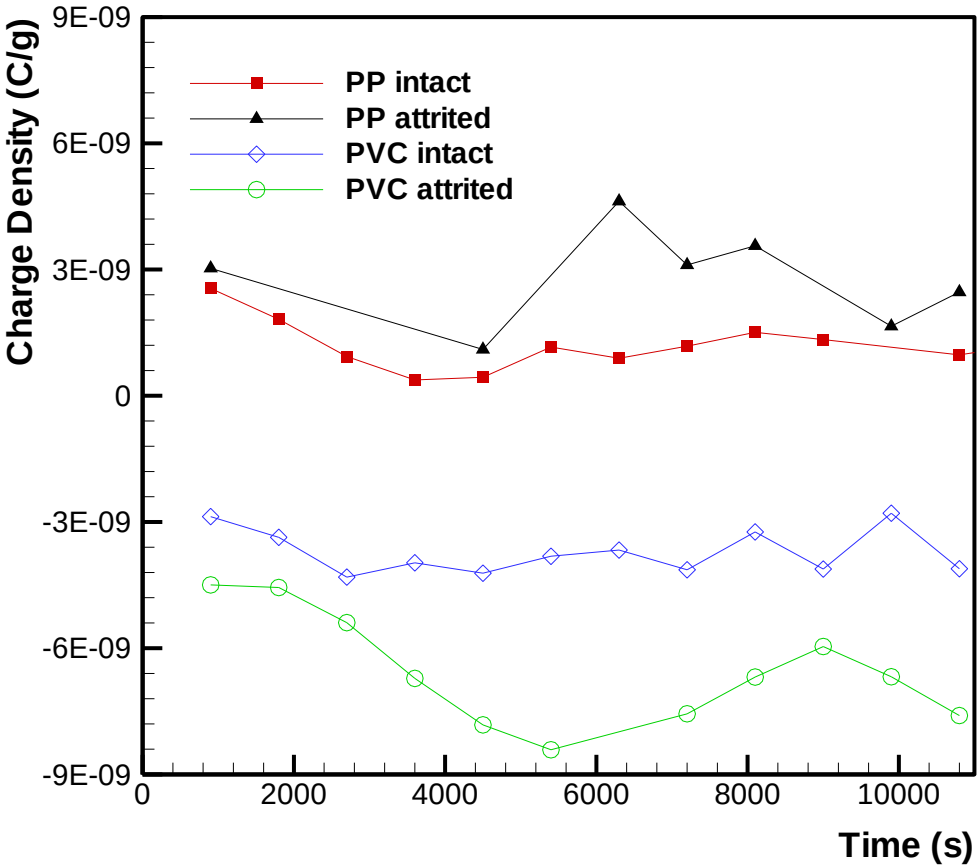

Figure 5.10 Comparison of four kinds of particles charge density: Mass of samples: PP-939 g, PVC-745 g; Airflow rate: 1600 L/min; Air superficial velocity 21.2m/s; Solids feed valve: PP-75% opening, PVC-flood-fed.

The above-mentioned phenomena seem inconsistent with the characteristics of charge generation on the pipe wall, which decreases with decreasing particle size. In order to resolve this contradiction, further experiments were carried out, in which valve 14 (Figure 2.4) was shut down to allow particles to be conveyed once through the system only. Figure 5.11 shows the resulting integral of induced current in such a single-pass operation, where the curved sections of the graph correspond to times when particles were moving through the system and the straight sections to times when all particles have stopped. It is easily observed from the two curves that a larger quantity of charge is generated by attrited samples than by intact ones. By a linear fitting of the data obtained, the slopes of the curve provide the average values of the induced current, -5×10^{-9}A and -3×10^{-8}A for intact and attrited samples respectively (Figure 5.11 (a)). Similarly, Figure 5.11 (b) shows that the average values of induced current are 5×10^{-9}A and 8×10^{-9}A for intact and attrited PVC samples respectively. The charge generation characteristics of the four types of particles are now consistent with the previous observation (Figure 5.10) that decrease in particle sizes during attrition corresponds with an increase in amount of charge generated.

This observation may be explained by a comparison of solid flow rates. It is shown in the previous granulate test that intact particles have much better flowability than attrited particles, regardless of the type of particles. Our previous work (Yao et al. 2004) demonstrated that the equivalent current should be consistent with the measured current on the pipe wall as shown in Equation (3.2).

Although attrited particles have larger charge densities than intact particles, a smaller solid flow rate of the former would possibly lead to a corresponding smaller

equivalent current I_c (product of charge density, Q_p and solid flow rate, SF) for attrited particles than intact particles. Similarly, the current on the pipe wall generated by attrited particles are weaker than that generated by intact particles. However, since there is little charge accumulation on the granules in a single-pass type of operation, solid flow rate does not show a strong effect on the equivalent current. Because measurements were performed at the very beginning of the experiment (i.e. after good discharge of the whole system), the results would not be influenced by the initial residual charge in the system. Therefore, induced current in a single-pass operation with intact samples is smaller than that with attrited ones as described in Figure 5.11.

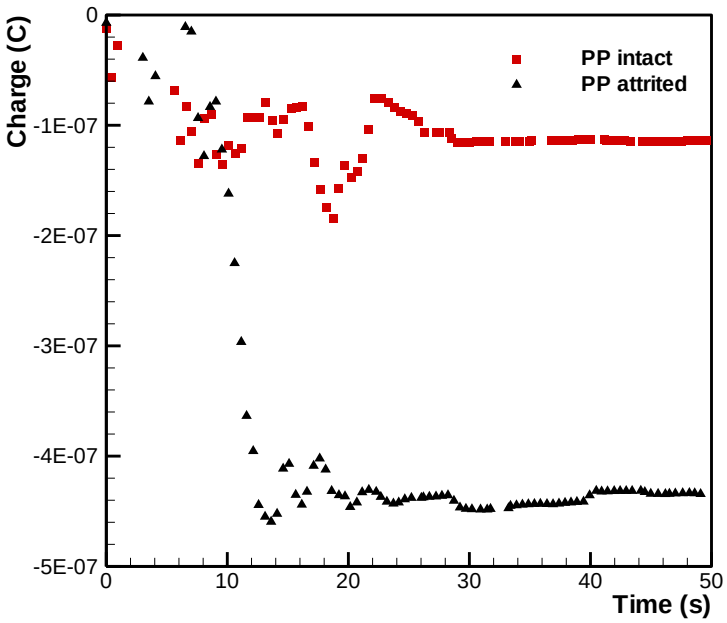

(a)

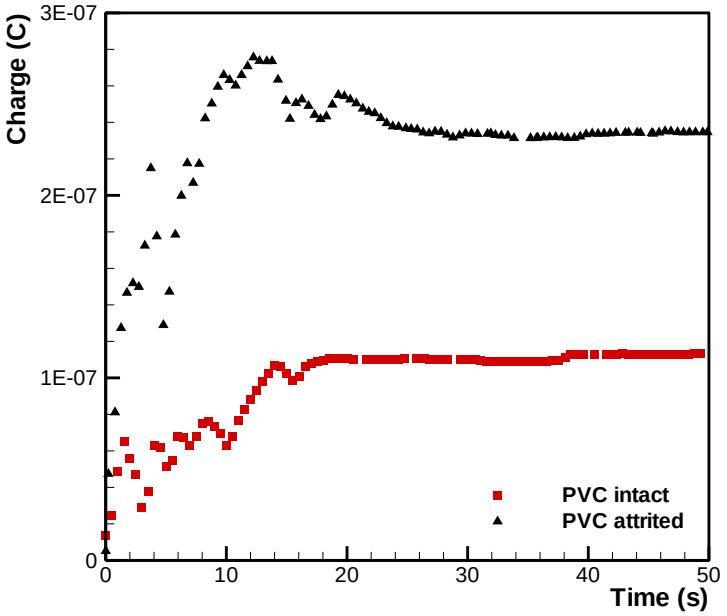

(b)

Figure 5.11 Integral of induced current in a single pass operation: Mass of samples: PP-939g, PVC-745g; Airflow rate: 1600L/min; Air superficial velocity 21.2m/s; Solids feed valve: PP-75% opening, PVC-flood-fed. (a) PP samples; (b) PVC samples.

5.3.2 Interrelationship between electrostatics characteristics and particle flowability

From the above-mentioned analysis, electrostatics affects solid flow rate greatly. During the course of each experiment, solid flow rates of all types of particles decreased gradually. Due to the effect of charge accumulation on particles and pipe wall, particles tend to stick on the pipe wall and the hopper especially and this in turn results in poor flowability of particles. Considering the material of particles, it is observed that the speed of reduction in solid flow rates for PP samples (Figure 5.12 (a)) is faster than that for PVC samples (Figure 5.12 (b)), which can be explained by higher charge generation by PP samples (section). Comparing intact particles to attrited particles, it is obvious that the former moved more rapidly than the latter during the entire operation, which is in accordance with the result of granulate test. However, despite the higher charge density of attrited particles, the time dependency of the flow rate of attrited particles seems to be the same as intact ones. The loop of single-pass operation for testing solid flow rate is shown as 5-6-……-14 in Figure 2.4, thus particles did not pass through the hopper (labeled 4 in Figure 2.4) and the effect of hopper on particle flow ability was isolated. However, as the granulate test shown, the flow ability of particles was affected more significantly by the hopper than by the conveying pipes. The major driving force in pipe is aerodynamic drag force, although some charged particles adhered to the pipe wall, the air can still force the particles to move ahead. Given the particle velocity was slightly reduced, the effect was not obvious. However, fully charged particles would stick on the wall of hopper and then the solid flow rate would reduce drastically. The clearer is the degree of such drop in solid flow rate when more charges were generated on the particle. In principle, the decrease in gradients of the curve for attrited particles would be higher than the

corresponding intact particles. Nevertheless, such prediction was not clearly observed in Figure 5.12 due to the limitation of solid flow rate measurements accuracy.

On the other hand, the flowability of particles has a crucial influence on electrostatic charge generation characteristics, especially for PVC samples conveyed through the system with 100% solids feed valve opening. Intact PVC particles with cylindrical shape and larger size were locked in the rotary valve with little motion through the conveying system. This manifested as several 250s thin gaps in the plot of induced current against time (Figure 5.13 (a)). With the attrited PVC samples, plenty of fine powders tend to stick on the feed hopper, causing discontinuity in the flow of particles through the system. Due to poor flowability this is more apparent for attrited particles and shows up as 3 obvious breaks in Figure 5.13 (b). Furthermore, the range of the induced current data becomes narrower gradually, indicating possible interactions between electrostatics and flowability. A larger amount of electrostatic charges accumulated on pipe wall leads to poorer flowability while at the same time, a smaller flowability will also result in smaller induced currents as demonstrated by Equation (3.2). In contrast to Figure 5.13, PVC granules move smoothly and continuously in a flood-fed condition, and the resulting induced current with good flowability of the particles was displayed previously in Figure 5.9 (a, b).

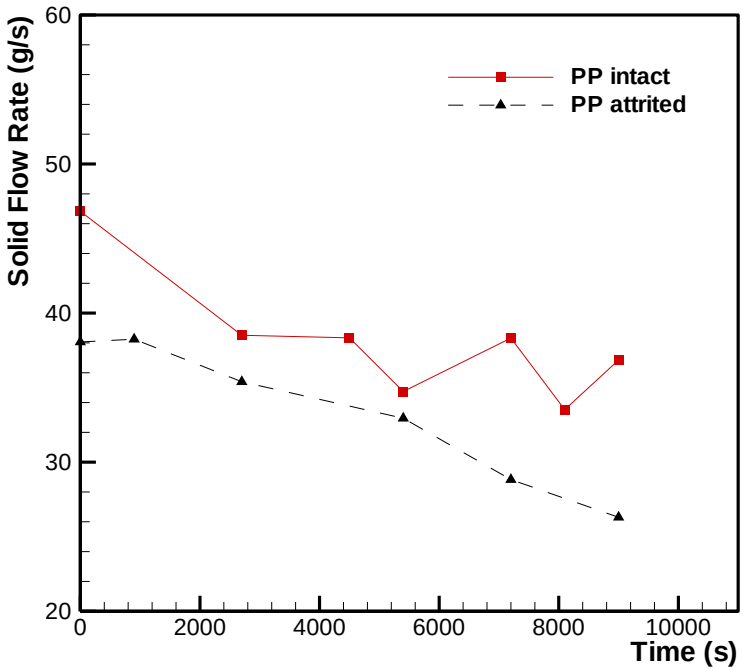

(a)

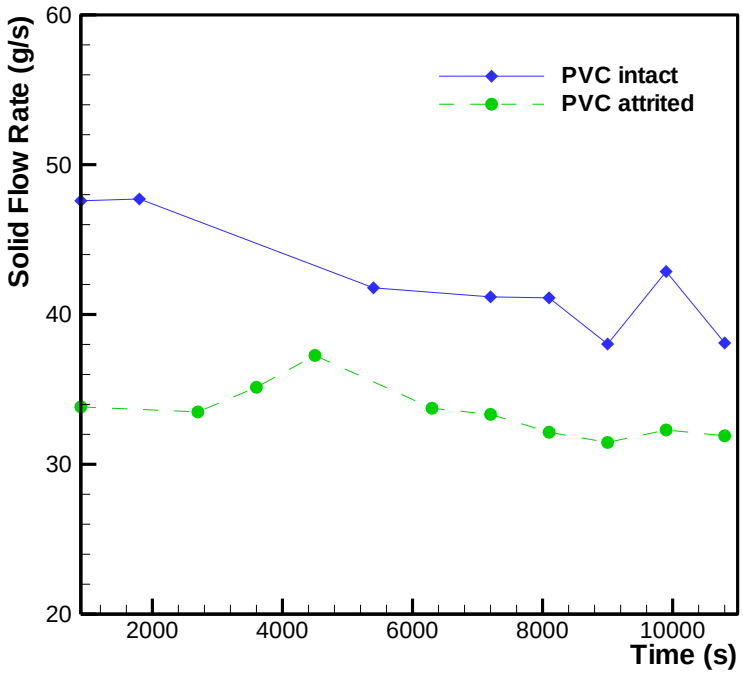

(b)

Figure 5.12 Effect of electrostatics on solid flow rate in pneumatic conveying systems: Mass of samples: PP-939g, PVC-745g; Airflow rate: 1600L/min, Air superficial velocity 21.2m/s; Solids feed valve PP-75% opening, PVC-flood-fed. (a) PP samples; (b) PVC samples.

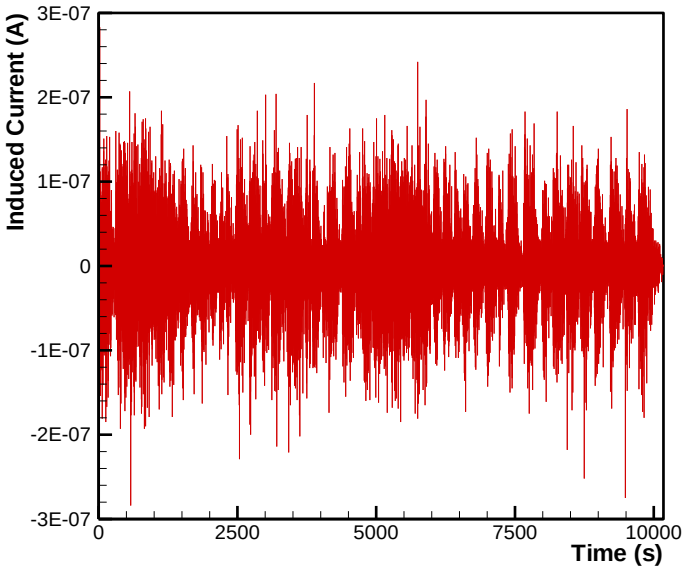

(a)

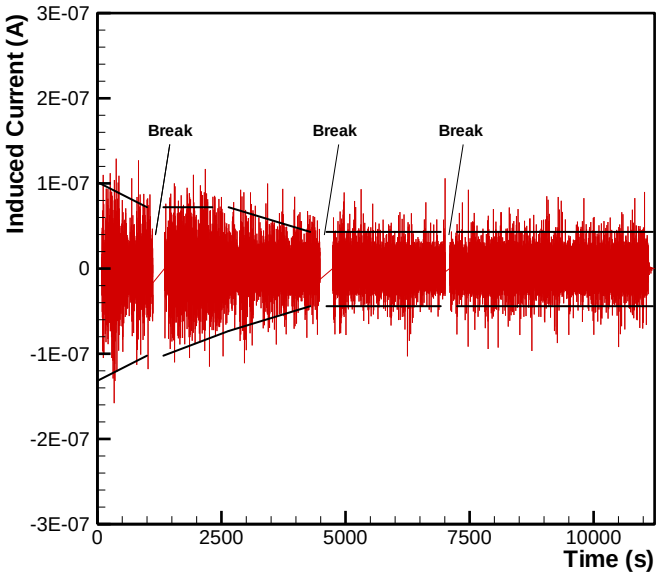

(b)

Figure 5.13 Induced current of PVC samples generated on pipe wall for small solid flow rate: Mass of samples: 745g; Air flow rate: 1600L/min; Air superficial velocity 21.2m/s; Solids feed valve: 100% opening. (a) Intact samples (3.35mm~4.2mm); (b) Attrited samples (1.18mm~3.35mm).

5.3.3 Particle material effect on electrostatics

From the above analysis, the most obvious distinction in the electrostatic behaviour between PP samples and PVC samples is the charge polarity on particles. The charge of PP particles is positive and that of PVC particles is negative for both intact and attrited samples, as shown in Figure 5.10. When two different materials are brought into contact (collide, roll or slide) then separate, electron is able to transfer between these two materials. The relative polarity of the charge acquired due to friction between two materials depends on their respective sequence in a triboelectric series (Diaz and Felix-Navarro, 2004). According to this series, PVC pipe is negatively charged by PP particles. However, for two identical materials, PVC granules and PVC pipe, particles can acquire either net positive or negative charges because of the similar material properties between the particles and the pipe wall. Based on the experimental data obtained in this study, there is a higher tendency for negative charges to be generated on the PVC particles than on the pipe wall.

One other difference in electrostatic behaviour between PP and PVC samples, in addition to the charge polarity, is the quantity of charge generated. As may be predicted from the triboelectric series, the potential difference between PP granules and PVC pipe should be higher than that between PVC granules and PVC pipe. In order to have a fair basis for comparison of the electrostatic charge generation characteristics of PP and PVC samples, the experiment was carried out in a flood-fed condition. Figure 5.14 shows the comparison between the induced current obtained from PP and PVC samples. With intact PP samples, the amplitude of the induced current is about $\pm 3.0 \times 10^{-7}$A. It may reach a high value of 7.0×10^{-7}A, with discharges

observed as sparks across the conveying pipe and indicated as peaks in Figure 5.14 (a). In contrast, for intact PVC particles, the range of induced current is only about $\pm 1.8 \times 10^{-7}$A, and no sparking was observed during the experiments (Figure 5.14 (b)). The above-mentioned phenonmenon is also observed with attrited samples in the system. The average value of induced current of PP samples is almost 3 times that of PVC samples. However, sparking was observed less frequently as shown in Figure 5.14 (c) and (d).

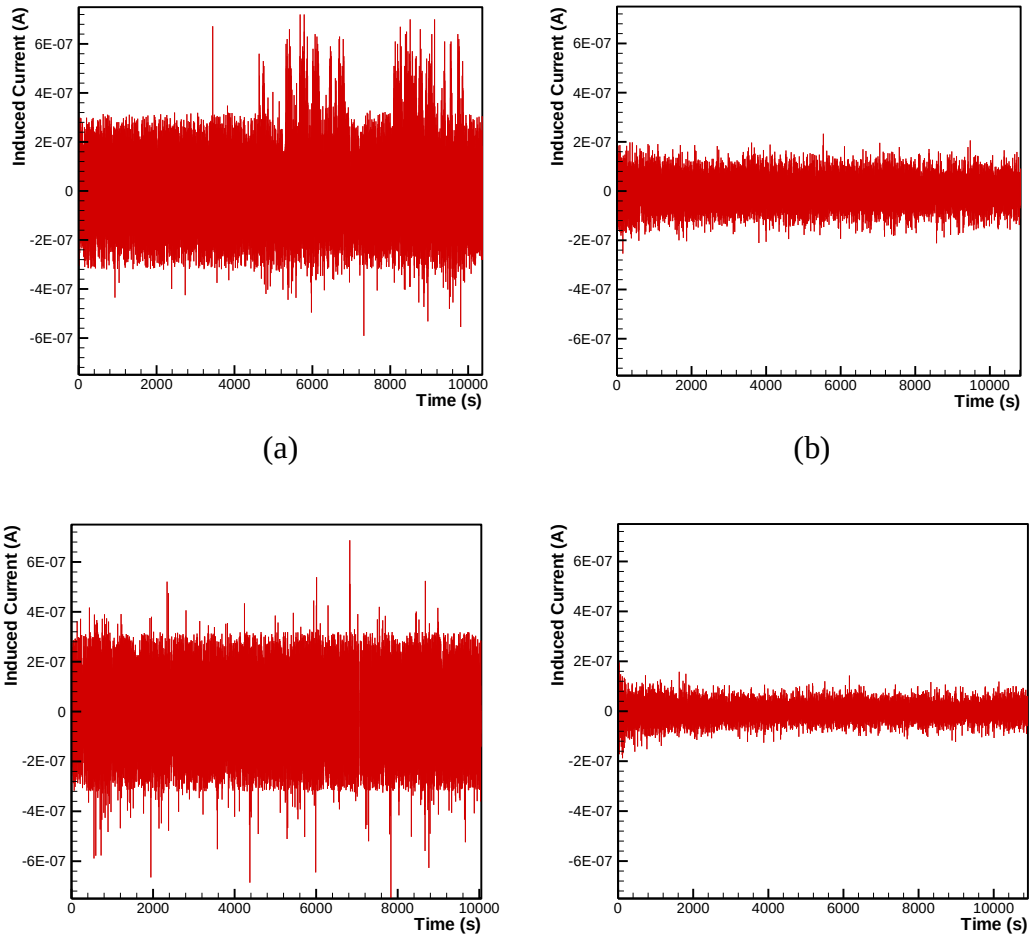

Figure 5.14 Comparison of induced current between PP samples and PVC samples generated on pipe wall: Mass of samples: PP-939g, PVC-745g; Airflow rate: 1600L/min; Air superficial velocity 21.2m/s; Flood-fed solids. (a) PP intact (2.8mm~3.35mm); (b) PVC intact (3.35mm~4.2mm); (c) PP attrited (1.18mm~2.8mm); (d) PVC attrited (1.18mm~3.35mm).

5.3.4 Effect of particle attrition on pipe wall abrasion and electrostatic charge generation mechanism

Friction between particles and wall generates electrostatic charge through a process known as tribocharging. The mechanism of tribo-electrification of granular flow in horizontal pneumatic conveying was studied in Chapter 3. Furthermore, friction between the particles and pipe wall would also lead to pipe abrasion. Pipe wall abrasion can be observed even with the naked eyes as roughness on the surface of the film. In order to characterize the extent of mechanical interaction between the particles and the inner surface of a pipe with a polymer film during a typical conveying process, the film was examined using a scanning electron microscope (SEM). Figure 5.15 shows SEM pictures (magnified 1000 times) of the fresh film surface and the film after being attrited by PP particles for 3h. It is evident that the quality of the film surface deteriorates quickly during usage indicating strong sliding effects and frictional forces between particles and the pipe wall. Compared with the original (Figure 5.15 (a)), films placed at different pipe sections were eroded to different extents. The film at the pipe bend was observed to contain a few holes (Figure 5.15 (b)), so it is deduced that most of the particles impacted the film with a sharp angle (Yao et al., 2000; Fan et al., 2002). In contrast, several gorges were seen on the films at the vertical and horizontal pipe sections (Figure 5.15 (c) and (d)), thus we may conclude that the most possible interaction between particles and pipe wall at both vertical and horizontal sections was sliding. Therefore, the mechanisms of charge generation were collision between particles at the bend section and friction between particles and wall at the vertical or horizontal pipe sections.

In order to describe the degree of pipe wall abrasion, an abrasion ratio is defined as the mass difference of the film before and after the experiment divided by the mass of the original film. Further detailed comparison of abrasion ratio is illustrated in Figure 5.16. In Figure 5.16, it is observed that the abrasion ratios in the three pipe sections are increased from horizontal to vertical orientation of the pipe and to the bend section for all four types of particles used. In particular, abrasion is especially significant at the bend section. It is expected that particles impact against the pipe bend with high velocities and large forces and so may cause significant breakage at this point in the system.

Furthermore, the abrasion resulting from attrited PP samples is more severe than that of intact PP samples (Figure 5.16 (a)). In this case, the shape of particles is the determining factor. Comparing with the smooth surface of intact PP particles, PP fragments have irregular edges and tough corners (Figure 5.1), which would damage the pipe wall seriously. The contacting pattern between particles and wall is also modified as attrition takes place. Intact PP particles have an ellipsoidal shape and contact the wall in a point-to-face manner while attrited particles with several smaller planes do so in a face-to-face manner. Therefore, the latter seems to have a larger contact area than the former, which may also result in higher charge generation by attrited particles (Figure 5.10).

In contrast to PP samples, from Figure 5.16 (b), the effect of wall abrasion by attrited PVC particles is weaker than that by intact ones. The reason is that abrasion due to PVC samples is mainly caused by the firm edges of the cylindrical particles but the fine powders produced from these intact particles during attrition lack such physical

features and so bring weaker damage to the pipe wall. Furthermore, the particle number density (Smeltzer et al., 1982) of attrited particles is higher than that of intact ones even under the same experimental conditions. This may also cause attrited particles to bring about higher charge generation (Figure 5.10) than intact ones.

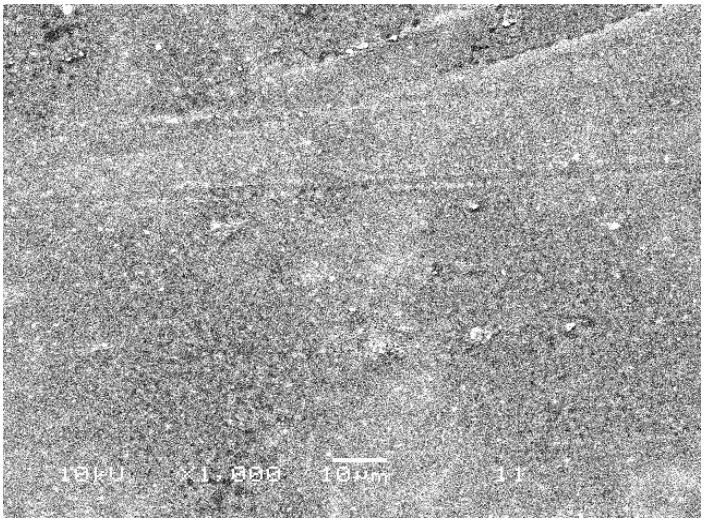

(a)

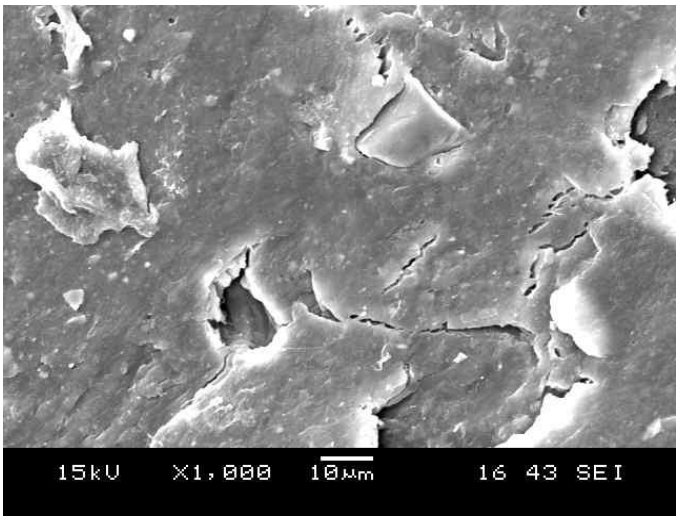

(b)

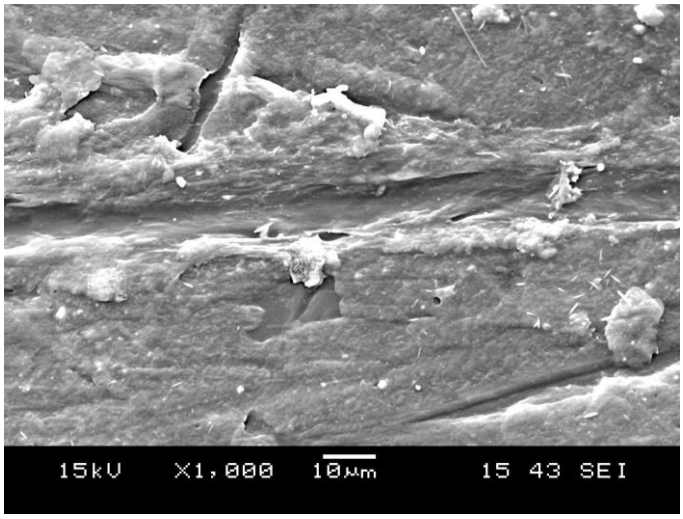

(c)

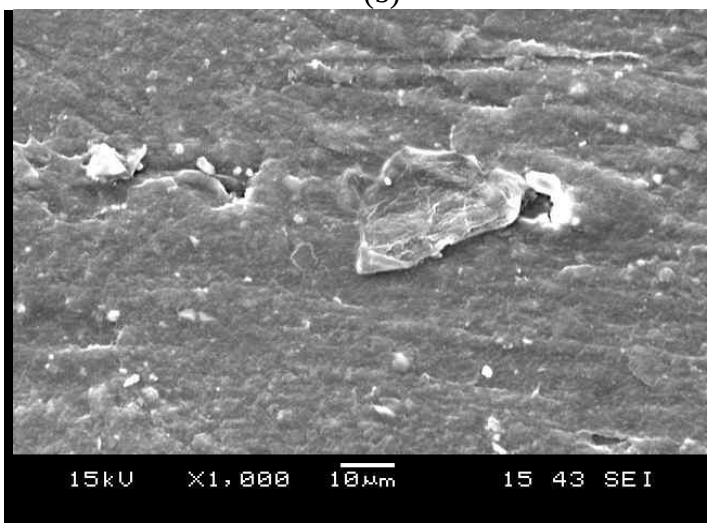

(d)

Figure 5.15 Scanning electron micrographs of polymer film attrited by PP: Air flow rate: 1600 L/min; Air superficial velocity 21.2m/s; Solids feed valve: 75% opening; Operation time: 3h. (a) Fresh film; (b) Abrasion film in bend; (c) Vertical abrasion film; (d) Horizontal abrasion film.

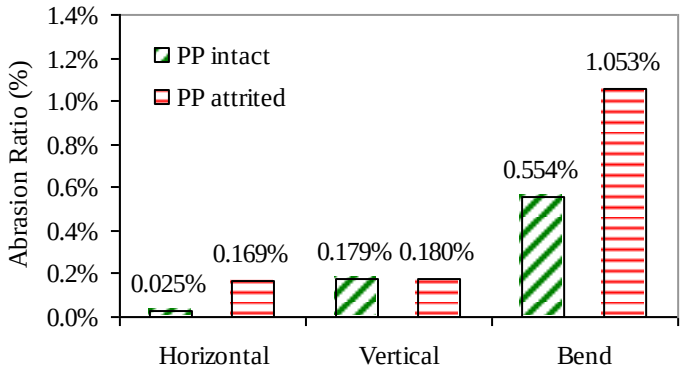

(a)

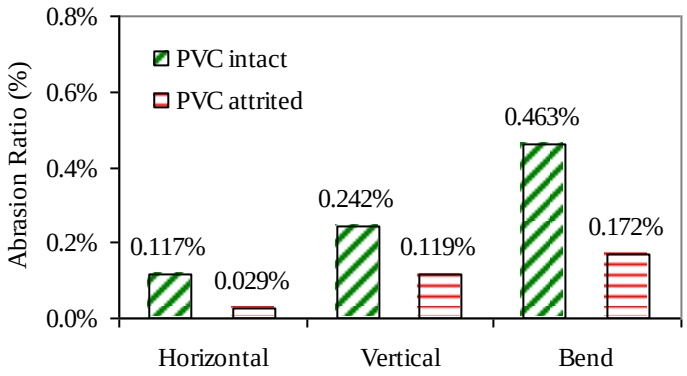

(b)

Figure 5.16 Comparison of abrasion ratio at three different pipe sections: Mass of particle: PP-939g, PVC-745g; Airflow rate: 1600L/min; Air superficial velocity 21.2m/s; Solid feed valve: PP-75% opening, PVC-flood-fed; Operation time: 3h. (a) PP samples; (b) PVC samples.

5.4 Concluding remarks

The process of particle attrition in a rotary valve feeder was studied; the physical properties of the granular material used and their variations due to the effects of attrition were studied in relation to the behaviours of particles in a pneumatic conveying system. The parameters investigated included particle size distribution, pipe wall abrasion and electrostatic charge generation characteristics. The main findings are as following. First, the ability of particles to endure compressive stresses after attrition is decreased, the flowability becomes poorer and the internal friction among particles is increased. This was seen for both PVC and PP samples. Second, in attrition in a pneumatic conveying system, both PVC and PP display the same general time variation of particle size distribution as that occurring in a rotary valve. A longer attrition time in the conveying system leads to almost the same size distribution as that obtained in the rotary valve with a shorter attrition time. The relationship between fractional degradation, X, and time, t, may be adequately described with the Gwyn function. Third, for both PVC and PP samples, the induced current decreases with decreasing particle size, but the charge density shows a reverse trend due to the effects of particle flowability. Due to the charge accumulation, solid flow rates decrease gradually with time for four kinds of particles, and in turn the low flowability leads to diminishing induced current on pipe wall. PVC and PP samples show opposite charge polarities and the quantity of charge generated by PP samples is much larger than that by PVC samples under similar experimental conditions. Forth, it is found that inter-particles or particle-wall friction and impact can induced the occurrence of charge generation, as well as pipe wall abrasion. Pipe wall abrasion by both PP and

PVC samples is greater in a vertical pipe and is most significant at a bend. However, the abrasion resulting from attrited PP samples is more severe than that of intact ones but converse behaviour is observed for PVC samples.

Chapter 6. Hazard of electrostatic generation in pneumatic conveying system

Electrical Capacitance Tomography (ECT) was found to be a useful, non-invasive tool for online monitoring of pneumatic conveying operations. In the present work, we propose to continue to apply the ECT technique to the measurement of pneumatic transport of granular material and study the electrostatic effects on ECT measurement. Furthermore, it is widely known that powder or dust particles can be ignited during pneumatic transportation, and hence lead to hazardous explosions. Cases of dust explosions have been reported to increase every year. Consequently, there is a high industrial demand for better understanding and assessing on such explosion hazards. In order to operate powder handling processes safely, there is definitely a potential importance in the study of the sparking mechanism in pneumatic conveying systems. In practical working systems, spark discharge is often observed at a pipe bend while brush discharge occurs less frequently at the horizontal pipe section. The induced current generated at the pipe wall can be measured with the techniques mentioned in previous chapters. In this chapter, its relation with hydrodynamic parameters (such as air flow rate) and with granule related parameters (such as solid flow rate, particle material and particle size) of the system would be investigated. The influence of environmental factors such as ambient relative humidity on spark generation would also be taken into account.

6.1 Sensitivity of ECT measurements due to the electrostatic charge effect

6.1.1 Theoretical analysis of electrostatic effect on ECT measurements

For a 12-sensor ECT system, a total of 66 (12×(12-1)/2) capacitance ($\vec{C}$ (66, 1)) measurements can be obtained for each cycle of measurements (Dyakowski et al. 2000). These capacitances are determined by the solids distribution over the cross-section of the conveying pipe, which is divided into 32×32 "pixels".

In a charge/discharge cycle, for instance, between electrode 1 and electrode 2, switch S_1 is first closed to connect to a known voltage U (Figure 6.1) to charge the system capacitance C_{s12}. Once the charging process is completed, S_1 is opened and S_2 is closed to discharge the stored energy from C_{s12} to the sensor C_{12} (the detecting electrode). Hence the charge is redistributed to develop voltage U_0, which can be measured. Therefore, according to the charge conservation law, total charge Q_T is:

$$Q_T = C_{s12}U = C_{s12}U_0 + C_{12}U_0 \tag{6.1}$$

And the unknown capacitance C_{12} can be obtained, as shown in Equation (6.2):

$$C_{12} = Q_T / U_0 - C_{s12} \tag{6.2}$$

However, in such a switched capacitor configuration, the effects of electrostatics at capacitor C_{12} were not considered. In a previous work (Zhu et al. 2004b), it was found that perturbations in the capacitance signal were due to charge accumulation. In pneumatic conveying of solids through a dielectric pipe, electrostatic charges are generated through particle-wall collisions. Charged particles not only affect the flow behavior but also affect the ECT measurements (Zhu et al. 2004b), so an additional electrostatic term has to be considered on the LHS of Equation (6.1):

$$Q_T + C_{12}U_s = C_{s12}U_0^{'} + C_{12}U_0^{'} \tag{6.3}$$

where, U_s is the potential difference between the electrodes 1 and 2, taking into account electrostatic charges accumulated on the pipe wall; U_0' is the measured voltage value. Therefore, U_0' replaces U_0 in Equation (6.2) and the unknown capacitance C_{12}' is calculated:

$$C_{12}^{'} = (Q_T - C_{s12}U_0^{'})/(U_0^{'} - U_s) \tag{6.4}$$

Ideally, electrostatic charges are distributed uniformly, thus $Us=U_1-U_2=0$ (U_1 and U_2 are potential on electrode 1 and 2 respectively due to the electrostatic charge), i.e. the term arising due to electrostatics can be eliminated, as shown in Figure 6.2 (a). If $U_0'=U_0$ and $C_{12}'=C_{12}$, the measured values are the reflection of the true values. Therefore, the switch capacitor configuration equations demonstrate that if the electric charge is distributed evenly, the effects of electrostatics can be eliminated.

However, in most of cases, the static charge generation is not uniformly distributed, such as due to gravity or pipe-curvature that one side of the pipe has much more particle impacts compared to the other side. For non-uniform charge distribution, $Us=U_1-U_2\neq 0$, as shown in Figure 6.2 (b), so that the electrostatics term cannot be neglected. Thus, $U_0'\neq U_0$ and correspondingly, $C_{12}'\neq C_{12}$, C_{12}' is a pseudo value of the unknown capacitance which cannot be corrected unless the electrostatics term can be measured independently. Similarly, 66 measured capacitance values $\vec{C}'$ would bring great errors in this case. Hence, capacitances measured through ECT sensors would be contributed from the solids permittivity distributions, electrostatic charges accumulated at the wall and carried by flowing particles. The disturbances in the capacitance measurements bring in the error in the permittivity calculated from ECT measurements. Therefore, the solids distribution would be not authentic and bring the

errors for the measurement.

In the current work, the conveying pipe used was made of plastic, implying that the electrostatic charges generated on the pipe wall could not be distributed uniformly over the entire pipe surface and supposedly their effects cannot be neglected. In order to verify whether electrostatic charge distributes on the pipe wall uniformly or not, a special induced current measurement was performed on the inclined segment as shown in Section 4.2.3 and enlarged in Figure 4.20 (a). The test section is divided into two parts and the experimental data can be obtained from the top and bottom of the pipe respectively. Induced currents were integrated with respect to time to obtain the cumulative a mount of charge on the pipe wall as shown in Figure 4.20 (c). It is observed that wall charge at the top of the pipe is greater than that at the bottom of the pipe. Therefore, according to the theory of the switch capacitor configuration as mentioned in Section 6.1.1, electrostatic charge would bring the influence to the ECT measurement.

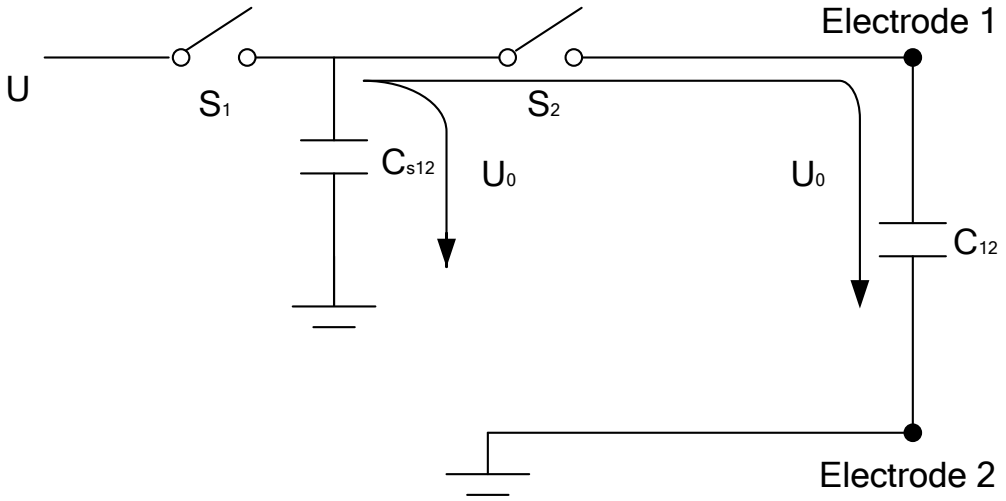

Figure 6.1 Switch capacitor configuration

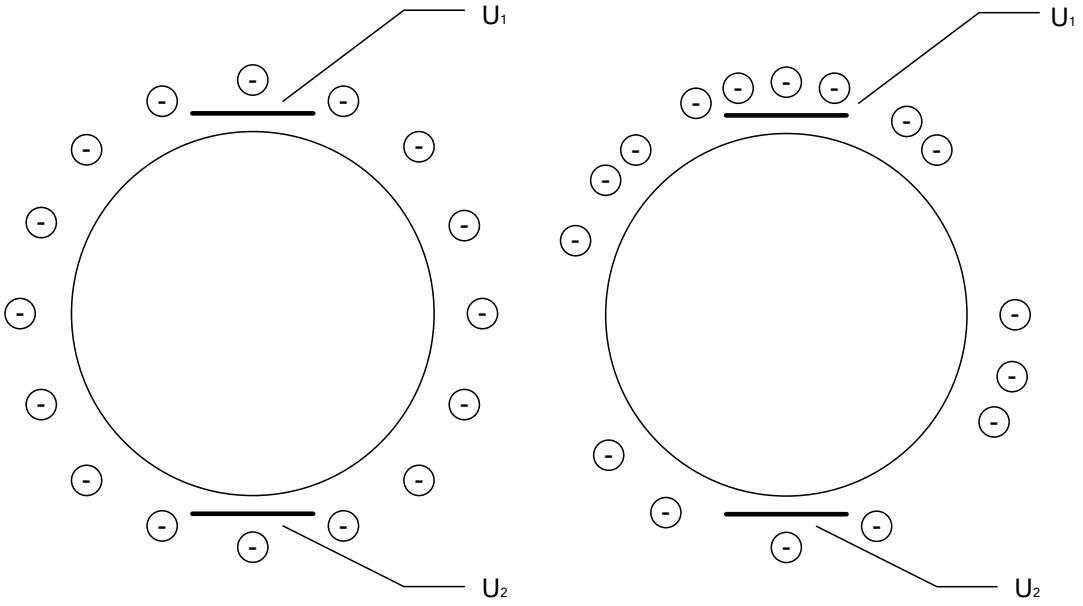

(a) (b)

Figure 6.2 Spatial electrostatic charge distributions over a cross-section of conveying pipe: (a) Uniform charge distribution; (b) Non-uniform charge distribution.

6.1.2 Sensitivity of ECT measurement due to the electrostatic charge effect

The electrostatic effect on ECT measurement in pneumatic conveying systems was confirmed by Zhu et al. (2004b), who first observed that the particle electrostatic charges may affect the measurement accuracy of ECT. In their study, the ECT measurements for the gas-solid operation are performed after supplying the solids into the conveying pipe for a finite period of time. Subsequently, the residual field perturbations around pipe walls due to the charge accumulation were recorded by temporarily (around 30s) cutting off the solids supply while leaving the air flow intact. Once the measurement was performed the solids supply was immediately resumed for the next time step and the recordings were repeated.

In the current experiment, electrostatic charge generated from the pneumatic conveying system was introduced into the separate ECT measurement section on a non-conductive pipe. Figure 6.3 shows the result of ECT measurements with electrostatic charge transferred from the pneumatic conveying system. The values on ordinate display the relative change of solid concentration (*RC*), which is defined as the ratio of solid concentration change normalized by the initial solid concentration, as shown in Equation (6.5):

$$\mathrm{RC} = \frac{(\alpha_t - \alpha_0)}{\alpha_0} \tag{6.5}$$

where, α_t is solid concentration at instant time and α_0 is solid concentration at initial time.

A blank test was carried out first, i.e. use ECT to obtain the particle concentration

distribution without electrostatic charges. It is observed that the curve of blank test is very close to zero showing that the data obtained from ECT should be considered steady and credible without introducing electrostatic charge. However, when charge was transferred to the test segment from different parts of the pneumatic conveying system, the associated curves of relative change show fluctuations around the zero electrostatic case. The values of relative change resulted from the charge generated on the horizontal pipe are more than 1%, while the data from vertical pipe and 90 ° bend present sharp variation, reaching a value of -14%. Especially for the change from 90 ° bend, such variation is irreversible. As for the comparison from different pipe bends (Figure 6.3 (b)), it is obvious that the relative changes brought up by 135 ° (up to -2%) bend are smaller than that brought up by 90 ° bend (up to -14%) during the experiment. Therefore, electrostatic charge generated from 90 ° bend affects the ECT measurements most significantly. In addition, the electrostatic charge can be introduced to either top or bottom of the pipe segment and the comparison of these results is depicted in Figure 6.3 (c). When charge was conducted to the bottom of the pipe, the relative change is as high as 4%, but there is no sudden change of this value. On all accounts, electrostatic charge interrupts the measurements of ECT. The concentration readings of still particles show obvious differences upon the introduction of charge to the pipe segment.

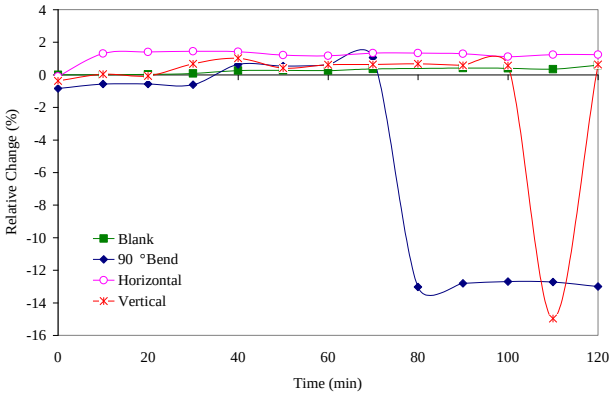

(a)

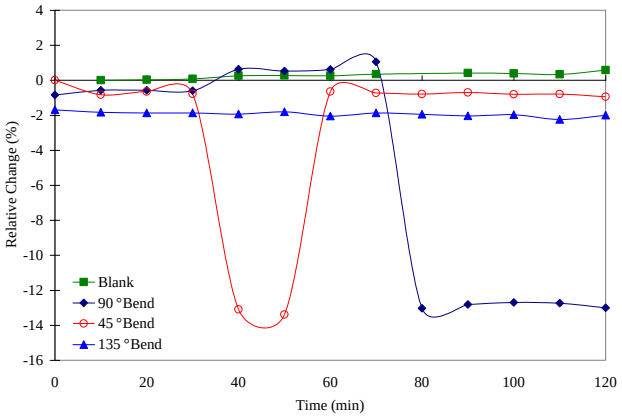

(b)

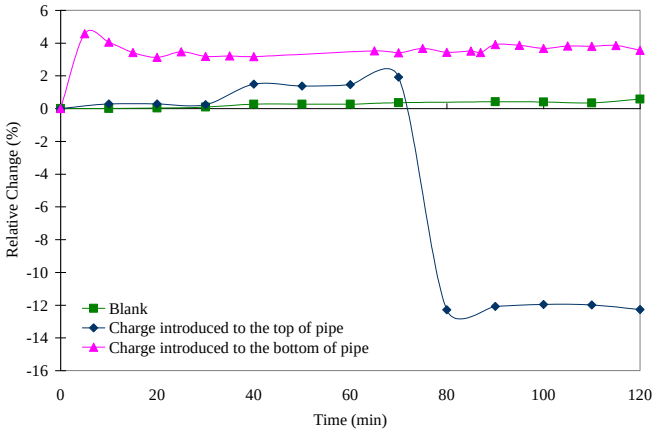

(c)

Figure 6.3 Sensitivity of ECT readings due to the electrostatic charge transferred from pneumatic conveying system: (a) Comparison of relative change aroused from charge generated by different parts of pipe; (b) Comparison of relative change aroused from charge generated by different bend of pipe; (c) Comparison of relative change aroused from charge introduced into top and bottom of the pipe segment

In order to detail the rapid change from 90° bend, four ECT images at various time were capture and illustrated in Figure 6.4. Figure 6.4 (a) shows ECT image of blank test, i.e. no charge was transferred to the test segment, in which four pictures are completely the same at four different moments during the time window of 120min. In contrast, in Figure 6.4 (b), it is observed that the first two images captured in 0min and 40min were almost the same as the initial state, but after 80min, the images varied largely due to the charge influence, which is corresponding to the value of -13% in Figure 6.3.

Moreover, the spark might be triggered by the strong electrostatics generated by the friction between PP samples and pipe wall. It would carry the risk of damaging the online systems. An example for spark phenomena is given below by performing the following ECT solid fraction measurements: Figure 6.5 illustrates the drastic difference in ECT images when spark is observed in the conveying pipeline. It is clear from this figure that under the case electrostatic field is close to electric breakdown potential (3×10^{6}V/m for the given facility, Yao et al. 2006b), the ECT readings are erroneous and full of artefacts due to uneven charge distribution discussed previously.

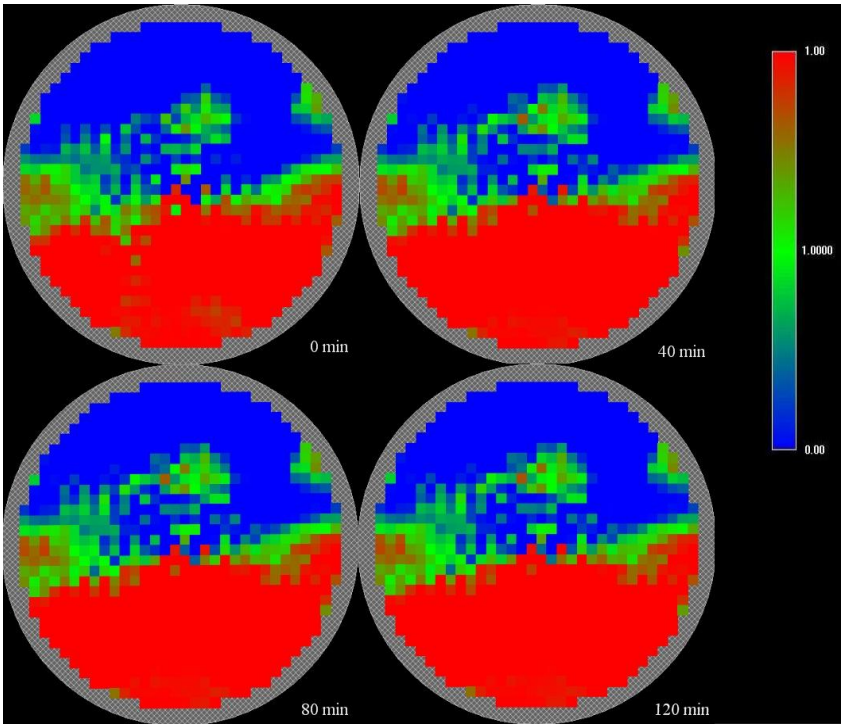

(a)

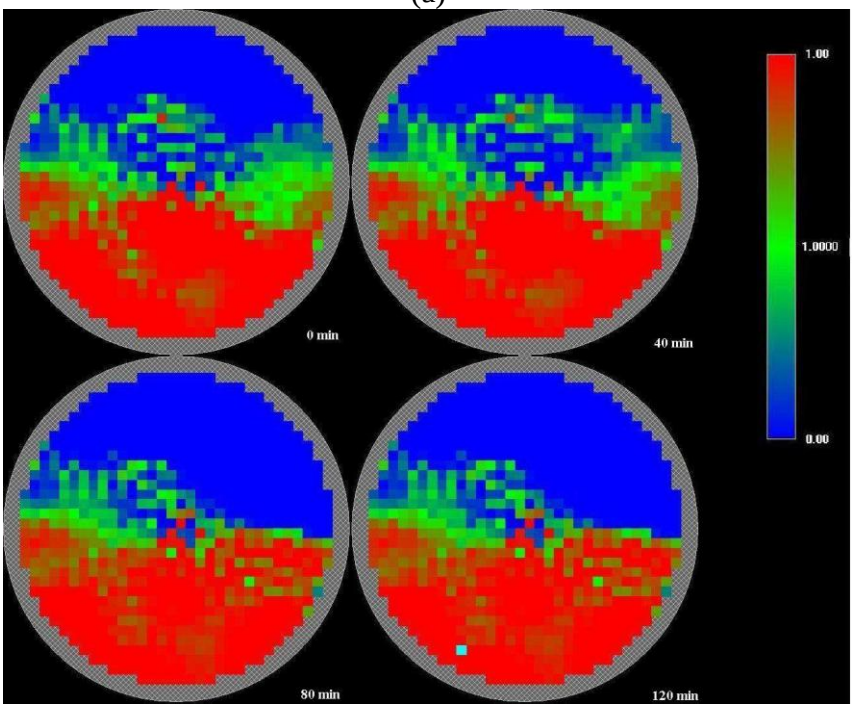

(b)

Figure 6.4 ECT images of test segment influenced by electrostatic charge: (a) Blank test; (b) Charge transferred from 90 °bend of pneumatic conveying pipe.

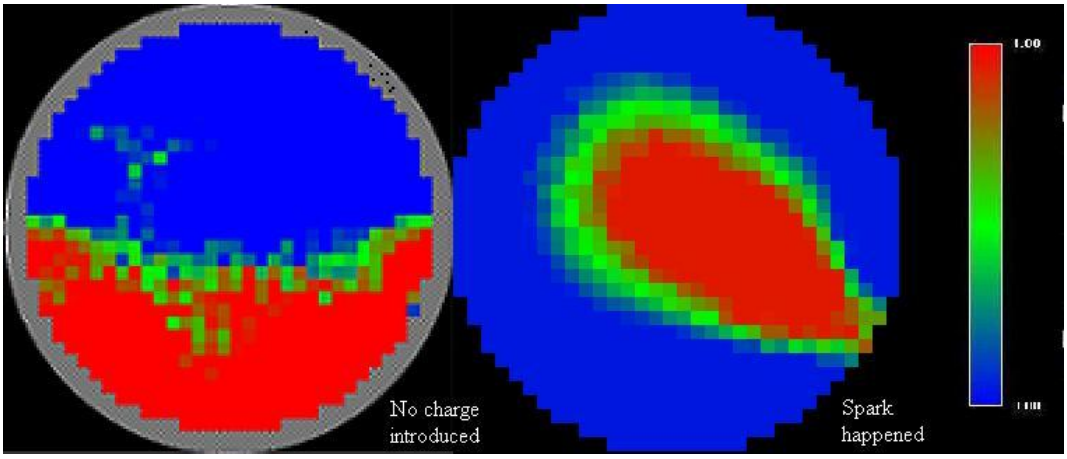

(a) (b)

Figure 6.5 Sensitivity of ECT images due to electrostatic sparks: (a) No spark; (b) With spark.

6.2 Spark generation due to the strong electrostatics

In Section 6.1.2, it was recognized that spark occurrence added serious damage to online instruments. In this section, it is attempted to record the induced current using an electrometer near the bend at the horizontal pipe. In previous electrostatic experiments, when solid feed valve was removed from rotary air lock (flood-fed condition), the solid flow rate was observed to increase significantly. Correspondingly, after particles were transported in the system for some time period, spark was seen as a sudden release of electric charges. Usually, spark generation can be explained as the following: firstly, the high electric field enables the electron to move from the valence band to the conduction band overcoming the energy band gap (>6eV for insulator); secondly, the free electrons move at high velocity with impact ionisation process to form the breakdown current. When the electric charge accumulated on the pipe wall, creating the high potential on the pipe, exceeding the electric breakdown field of the air, the electric charge (i.e. free electrons) would move to the conductor or ground nearby abruptly. During the discharge, the charge energy accumulated in the previous step would release as the light, heat and sound, i.e. the spark observed in the experiment. By observation, the spark generally occurs at the bend of pipe, due to much stronger charge generated at this point.

6.2.1 Electrostatic character of spark phenomena

When PP samples were conveyed in the system for around 1700s, the induced current was observed to increase suddenly from the normal value to -6×10^{-7} A as shown in Figure 6.6 (a). At the same time, a bolt of lightning flashed across the conveying pipe

with a tremendous cracking sound. When the flash appeared in the detection point of induced current, the induced current changes its polarity and increased sharply from negative value to positive value of about 6×10^{-7} A as shown at the instantaneous time of 1800s in Figure 6.6 (a). The accumulation of charge estimated by the integration of induced currents also shows abrupt variations, as shown by the turning points A and C in Figure 6.6 (a). The slope of charge curve around the turning points changes from negative to positive and thus confirms the variation of polarity in induced currents. Qualitatively, consistent variation is also reflected on another experiment of particle charge density (measured by Faraday cage) which fluctuates between negative and positive values (Figure 6.6 (b)).

The reason may be due to the fact that the friction between particles and pipe wall generates too many charges within a short period of time, such that the electrostatic charge accumulates to reach the saturation value and any additional accumulation is released spontaneously as a flash. Based on the triboelectric series (Diaz and Felix-Navarro, 2004), the electric current produced by PP samples upon rubbing on the PVC pipe wall should be negative and the flow direction of electron is from the pipe wall to the ground via electrometer. However, after the spark releasing of charge from the pipe wall, the amount of electron reduces abruptly from pipe. The pipe wall charge changes its polarity as little or no charge recombination is made in contact with positive-charged particles. Therefore, the current polarity varies from negative to positive and the negative charge would make the compensation ceaselessly, until the balance was recovered as shown by the phase AB in Figure 6.6 (a). If the charge is strong enough such that the maximum value on electrometer is exceeded, the data recording would be interrupted. After restarting the electrometer, the value of induced

current recovers to the normal value in the instant time of 6000s, as point B shown in Figure 6.6 (a), and then the former process repeats (6000s~10000s). The above description shows that the instrument may be damaged by extremely strong electrostatic charge.

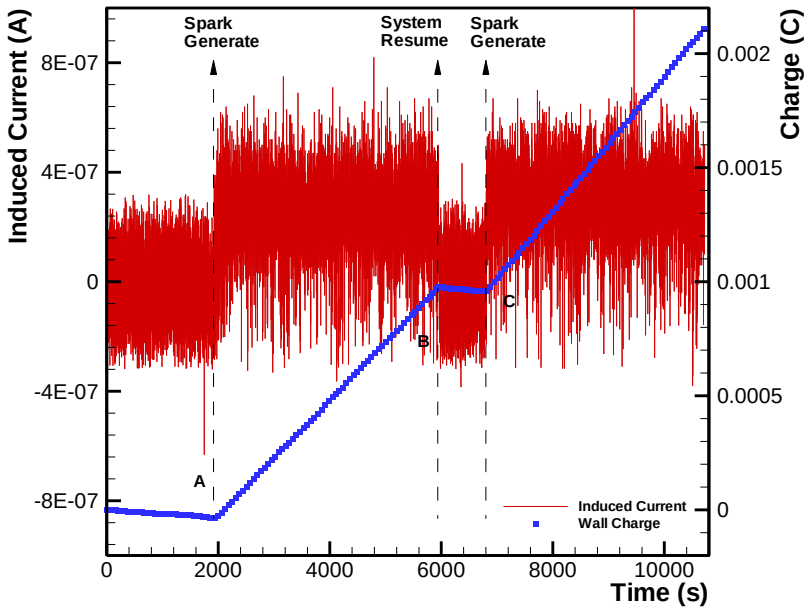

(a)

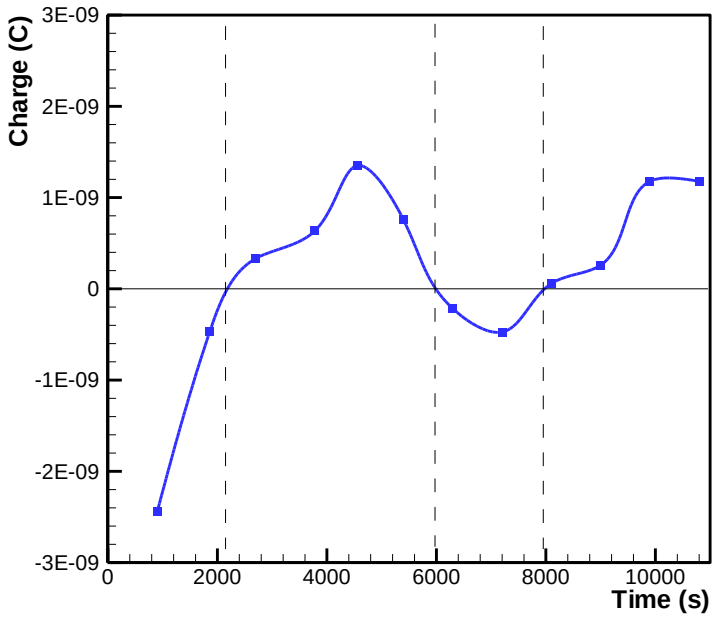

(b)

Figure 6.6 Electrostatic characters of spark phenomena for PP samples (air flowrate=1600L/min, air superficial velocity 21.2m/s, solid flow rate=45.67±3.29g/s, flood-fed condition, ambient RH=60%): (a) Induced current on pipe wall and wall charge calculated by the integration of induced current; (b) Particle charge density.

6.2.2 Factors affecting on the spark phenomena

Figure 6.7 can be compared directly with Figure 6.6 (a) for evaluating the effect of solid flow rate on spark phenomena. In this experiment, solid flow rate is the most crucial factor. Only in the flood-fed condition (solid feed valve was removed) and solid flow rate being increased to more than 5g/s can the spark phenomena be observed, as shown in Figure 6.6 (a). Furthermore, the range of induced current in the lower solid flow rate regime is less significant (around $\pm 2.5 \times 10^{-7}$A in Figure 6.7) than that in the high solid flow rate regime, thus the electric charge is not strong enough to initiate the spark.

Figure 6.8 presents particle size effect on the spark phenomena. When small PP samples were conveyed in the systems, spark was also generated. However, the electrostatics was not as strong as that generated by PP with large size range. Spark can be seen only a few times, and the corresponding electrostatic charge is not strong enough to cause polarity change. In contrast, the samples with large particle size tends to generate electrostatic charges with high positive values as shown by the peak values in Figure 6.8 (a) and cause the system to break down as the value decreased from 8×10^{-7}A to 3×10^{-7}A. Such phenomena are also attributed to solid flow rates. As analyzed in Chapter 5, particles with small size have poor flowability, as well as the low solid flow rates.

Figure 6.9 displays induced current comparison between PP and PVC samples. PP samples have much stronger electrostatics than PVC samples. This causes the measurement system to breakdown as shown by the gap A indicated in Figure 6.9 (a).

The finding is consistent with the results in Section 5.3.3 that the quantity of charge generated on PVC pipe wall by PP samples is much larger than that by PVC samples due to the high discrepancy between PP and PVC in triboelectric series (Diaz and Felix-Navarro, 2004). Furthermore, when PVC samples were transported through the pipe, no generation of spark was observed and the amplitude of induced current was only about $\pm 1.8 \times 10^{-7}$ A in the similar experiment condition. The reason can still be related to solid flow rate, which is much smaller for PVC samples than that for PP samples with better flowability, as demonstrated in Chapter 5.

The effect of ambient air humidity on the spark phenomena is shown in Figure 6.10. The humidity in the pipe system has been fixed at 5%, but it is difficult to control the ambient air humidity due to the limit of current experiment. The ambient RH means the RH of the ambient air surrounding the test rig. In current experiment, the spark phenomena were always found outside the conveying pipe not inside the pipe line; therefore, it is meaningful to study the influence by the ambient RH on the electrostatics. In general, the spark can be observed when ambient RH (relative humidity) was around 60%. In contrast, when ambient RH was about 95%, spark phenomenon was seldom observed. There are few spike peak values ($\pm 6 \times 10^{-7}$A) of induced current in Figure 6.10 (a), while such values represent more than 2/3 of the entire operation time in Figure 6.8 (a). Furthermore, it is more obvious in Figure 6.10 (b) for the integration of induced current over a period of 2000s, where wall charge in the ambient environment with high RH is found to be much smaller than that in the atmosphere of low RH. This finding can certainly explain the non-occurrence of spark when RH is very high. The reason may be that the opportunity of contact between electron and water vapor increases, resulting the formation of inactive ion and the

raise of breakdown potential; therefore, the difficulty of spark generation increases in high ambient air humidity.

Finally, the experimental results are summarized in Table 6.1 to highlight the conditions observed for spark generation in the given pneumatic conveying system.

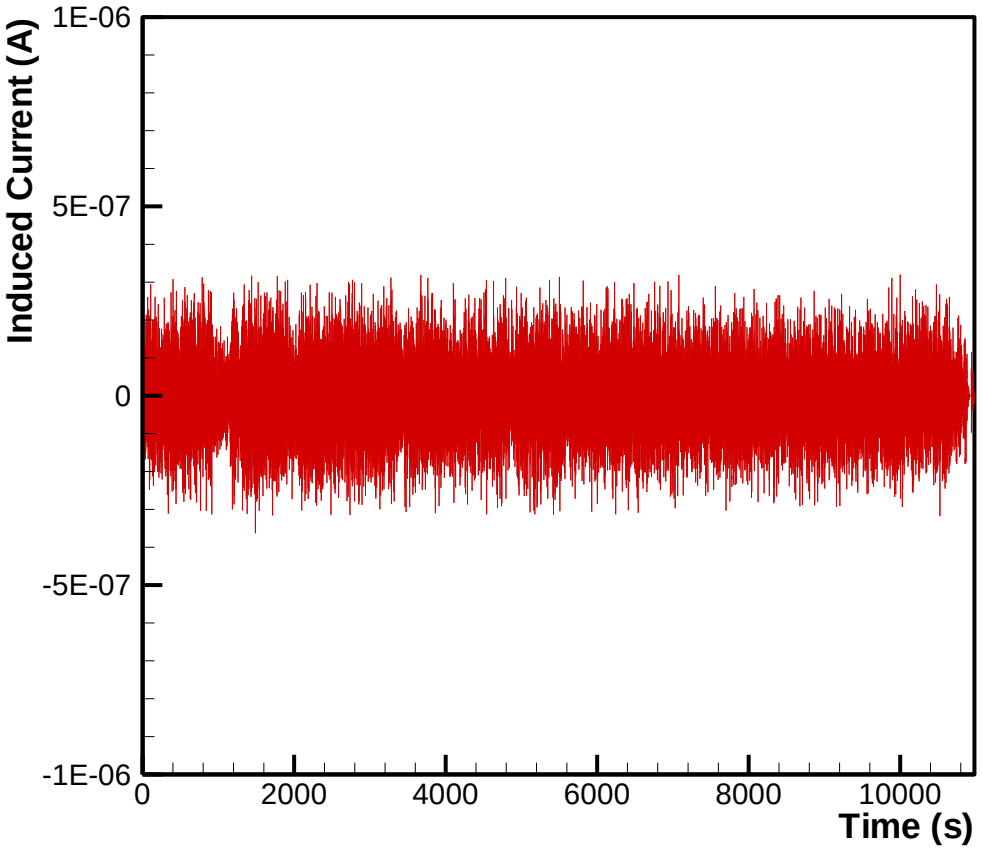

Figure 6.7 Comparison of induced current with Figure 6.6 (a) for PP samples (air flowrate=1600L/min, air superficial velocity 21.2m/s, solid flow rate=40.67±3.29g/s, solid feed valve opening=75%).

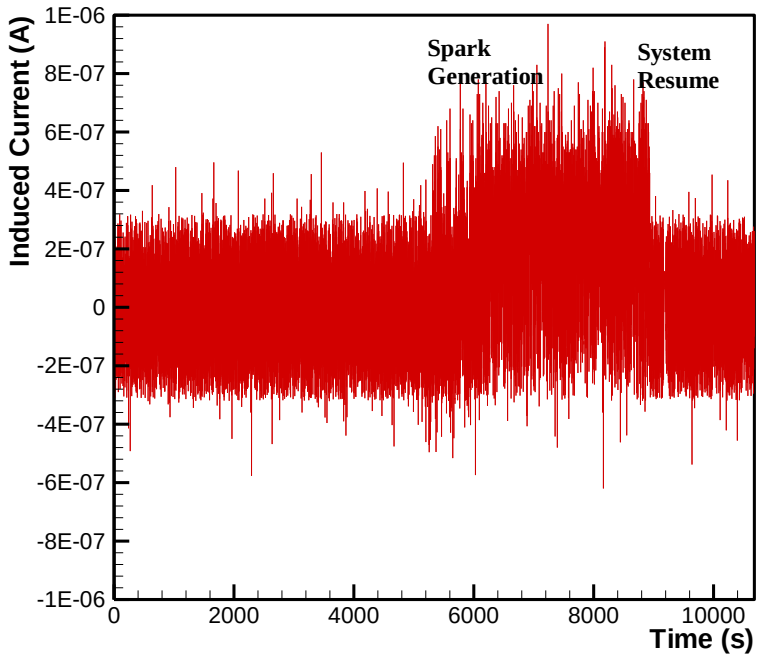

(a)

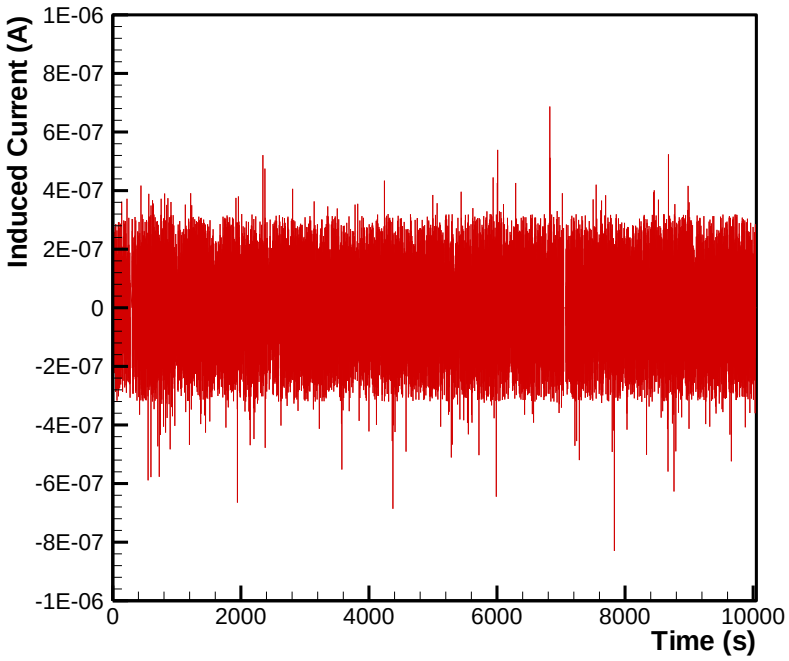

(b)

Figure 6.8 Comparison of induced current generated by PP samples with different size ranges (air flowrate=1600L/min, air superficial velocity 21.2m/s, flood-fed condition): (a) Size range of 2.8mm~3.35mm; (b) Size range of 1.18mm~2.8mm.

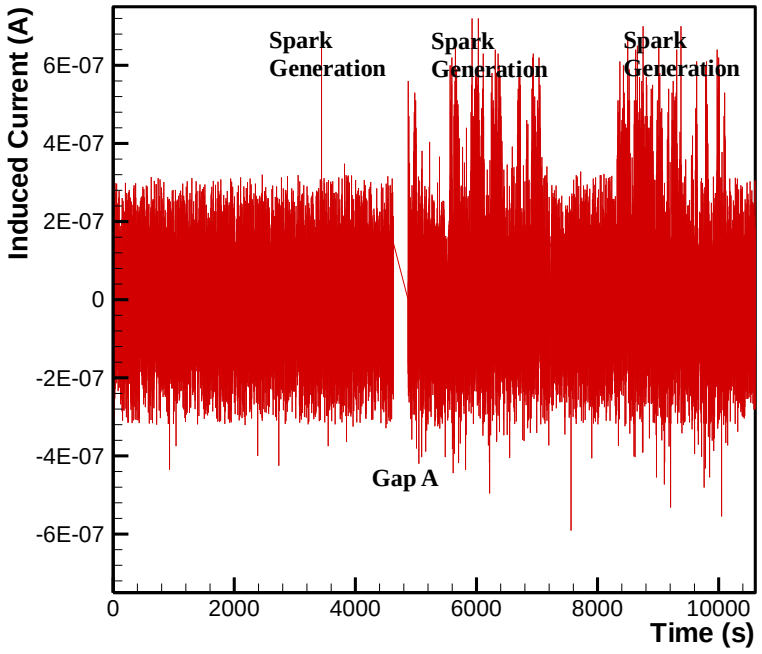

(a)

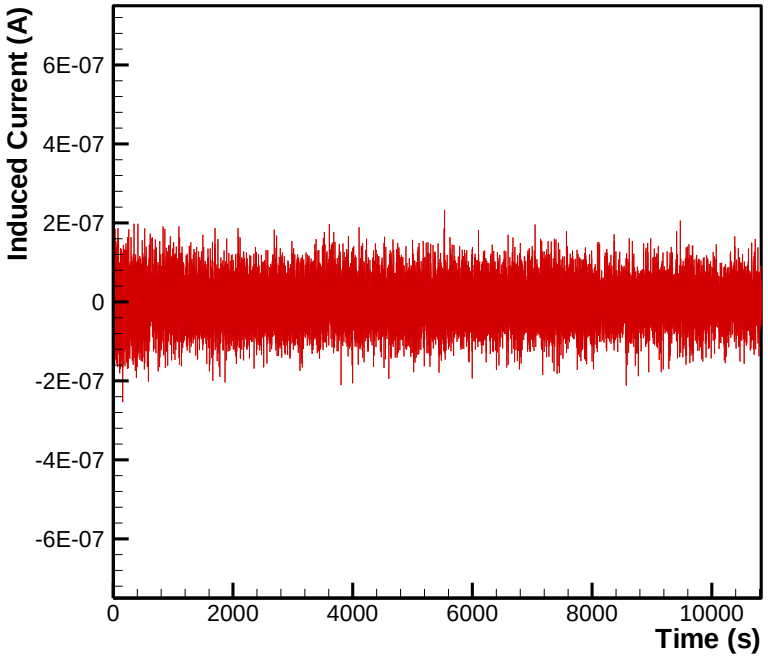

(b)

Figure 6.9 Comparison of induced current generated by different kinds of particles (air flowrate=1600L/min, air superficial velocity 21.2 m/s, flood-fed condition): (a) PP samples (Gap A shows that the instrument was broken down by spark generation); (b) PVC samples.

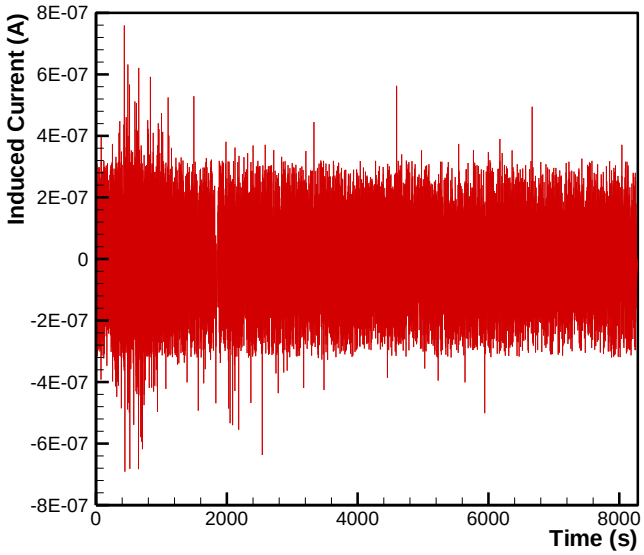

(a)

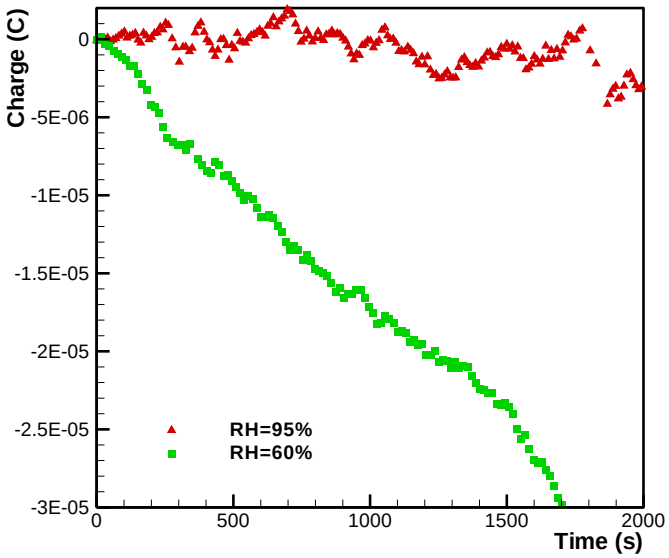

(b)

Figure 6.10 Comparison of induced current with Figure 6.8 (a) for PP samples: (a) Induced current (air flowrate=1600L/min, air superficial velocity 21.2m/s, flood-fed condition, ambient RH=95%); (b) Pipe wall charge integrated from the induced current data.

Table 6.1 Comparison of experimental conditions for spark generation of PP samples after running the conveying system for 1700s.

	Particle size (mm)	Solid flow rate (g/s)	Ambient air humidity [a] (RH)	Induced current (A)
Spark	2.8~3.35	42.3~49.0	60%	6×10^{-7}
No spark	1.18~2.8	37.3~44.0	95%	2×10^{-7}

[a] Relative humidity (RH) of air inside the pneumatic conveying pipe was fixed at 5%

6.3 Concluding remarks

The primary results for the sensitivity analysis of ECT measurement due to the electrostatic charge are summarized here. First of all, electrostatic charge generated from $90°$ pipe bend influenced ECT measurement most significantly. Furthermore, electrostatic charge affected solids concentration of ECT measurements and even resulted in a distorted image when strong charges were generated. In an extreme case, when electrostatic charge is accumulated to a sufficiently high magnitude, sparking occurs and this leads to a complete distortion of ECT image. In this chapter, theoretical analysis was also developed to demonstrate the error of ECT measurements caused by the non-uniform electrostatic charge distribution in the conveying pipe. However, surface charge distribution is difficult to be measured using the current experimental setup. Therefore, our present study of quantifying the effects of electrostatics on ECT measurements would be a necessary first step towards the overall research goal by developing a set of techniques or protocols for the elimination of errors in ECT measurements arising from such effects.

Furthermore, in a case study of generation of spark due to the electrostatics was induced using the electrometer at the horizontal pipe after running the conveying system for around 30min. At the moment of sparking, the magnitude of induced current could reach as high as 6×10^{-7}A and the levels of induced current and charge density show severe variation and unsteady fluctuations. Working conditions were found to significantly affect spark occurrence. Particles and pipe wall with high discrepancy in triboelectric series in the condition of high solid flow rate, large size

and low ambient air humidity would facilitate the generation of sparking in the conveying system. The static charge can build up to dangerous levels and cause major discharges (dielectric breakdown of the air) inside the pipeline to damage the measurement electronics in severe cases, unless precautions are taken before hand to protect these electronic devices.

In addition, the safety measures are summarized below. Firstly, the experimental setup and instruments should be grounded well to avoid the accumulation of electrostatic charge. Secondly, the commercially available antistatic agents could be used to reduce the charge accumulated on particles and pipe wall. Thirdly, the conveying speed should be controlled to reduce, when the experiment was carried out in low RH level. Forthly, the experimental system should be installed far from the tinder.

Chapter 7. Conclusions and recommendations

The present study investigated the electrostatic characteristic of granular flow in pneumatic conveying systems. For vertical and horizontal conveying flow, as described in the second chapter, three flow patterns, dispersed, half-ring and ring flow, observed in the experiment were studied. It was found that electrostatic behavior of granular flow was mainly related to the airflow rate. Lower airflow rates led to the higher induced current, particle charge density and equivalent current of the charged granular flow, and thus resulted in half-ring and ring flow structures. Electrostatic charge generation also increased from horizontal pipe to vertical pipe, with time development and with the decreasing of air humidity. In the experiment of charge generation mechanism, it was verified that electrostatics was generated due to the triboelectrification and was also influenced by the material of pipe wall. Furthermore, the charge effects could be reduced drastically by mixing the antistatic agent, Larostat-519 powders.

For the granular flow conveyed in 45 °inclined pipe presented in the third chapter, the concentration and velocity distributions of particles, directions of particle motions and electrostatic properties for three flow patterns, dispersed, reverse and half-ring flow, were described and compared using separate measurements. For the dispersed flow pattern, the solid fraction was dilute and solids moved forward in the entire cross-section of conveying pipe. For the reverse flow pattern, some particles deposited at the bottom of the pipe and slid downwards. In contrast, for the half-ring flow pattern, most of particles stuck on the pipe wall and formed an uncompleted ring

structure. The whole solid phase was divided into a few regions based on the fraction and motion of solids to analyze dynamic forces on the single particle. According to such an analysis, the phenomena of three flow patterns could be explained. It is concluded that the air flow rate and associated electrostatic force were the basic elements for determining granular flow behavior, and these in turn led to the formation of such particle structures as the remarkable reverse flow in transition region and the stagnant ring flow in dense region. This hypothesis was also supported by experimental results, when particles were mixed with the antistatic agent, Larostat-519 powders.

Among the few impact factors of the electrostatic character of granular flows, particle attrition was highlighted in the fourth chapter. This work explains the attrition effect on electrostatic character of granular flows from the angle of granular physical properties and their variation by attrition. Consequently, the electrostatic charge generation of flowing particles, including induced current and particle charge density, were compared between intact and attrited particles (here, attrited particles are referred to the particles after attrition experiments), which were also related to the particle size distribution and pipe wall abrasion. In this work, it was found that particle attrition mostly occurred in the rotary valve rather than in the conveying. This statement was drawn by comparing the size distribution after attrition in both systems and the relationship between fractional degradation and temporal evolution of the Gwyn function during the process of attrition. It was found that the induced current decreased but the charge density increased after attrition with decreasing particle size due to the effects of particle flowability. This phenomenon was demonstrated to be worsening during attrition in physical experiments and particle material affected

electrostatic character both on charge polarity and quantity. In addition, this attrition study reconfirmed the observation in the second chapter that electric charge was generated by the friction between particles and pipe wall. Such friction also caused pipe wall abrasion, which was most severe in pipe bend, then in the vertical pipe section. However, the above results and findings were specific to the test rig and products used, for example, blow-through rotary valve, PVC pipe and PP/PVC particles. Therefore, it is suggested that future work should further extend the experimental conditions to generalize the conclusions, for example, to extend the work to other configurations/valve designs and to use particles having a greater hardness than those investigated in this study.

During the electrostatic experiment, the potential hazard was revealed, for example, electrostatic charge could damage the ECT instrument in this work. Therefore, the sensitivity of ECT influenced by the electrostatic charge was summarized as: electrostatic charge generated from sharp bend (e.g. 90 º) of pipe influenced ECT measurement most seriously, compared to that generated from horizontal pipe and vertical pipe section, as well as that generated from 45 ºpipe bend and 135 ºpipe bend. It was also observed that charge introduced to the bottom of the pipe significantly affected ECT measurements. This study offered a perspective to examine whether the accuracy of ECT measurements suffers from electrostatics. The present work described the phenomena of charge influence on ECT and also provided an explanation on such influence according to the charge balance in a switch capacitor configuration. In the future, more work should focus on how to eliminate such errors in the measurements. A few potential methods to remove the influence of the electrostatics on ECT measurement would be briefly described below. First of all,

conductive material might be coated over the insulated pipe section for the ECT sensor to ensure uniform electrostatic charge distribution. Secondly, it is proposed that commercially available antistatic agents, such as Larostat-519 powder could be used to reduce the charge accumulated on particles. In the next phase of the research program, it is recommended that analytical method will need to be developed to compensate and calibrate the measurement errors caused by non-uniform electrostatic charge distribution in the conveying pipe.

The hazard with electrostatics is also recognized, for instance, when electric charge accumulated on pipe was high enough, sparks would be generated along the pipe wall. Therefore, its connections with granule related parameters of the system were investigated. From the observation made in the experiments, some phenomena related to spark can be summarized in the followings. Firstly, when sparks occurred, induced current and charge density fluctuated between negative and positive values. Secondly, sparks were usually observed to be generated by large particles in higher solid flow rate, and also at low ambient air humidity and between two insulated materials with high discrepancy in triboelectric series. However, due to the time and the equipment limitation, understanding of this phenomenon was not sufficiently thorough. Therefore, it is suggested that future work should concentrate on what the required conditions would be for the generation of sparks and development of a fundamental understanding of the relation between granular flow patterns and the distribution of induced electric field. Such a relation may potentially be used for predicting when and where spark discharging would occur and so would be useful for industrial operations.

In conclusion, the current study aims at a complete investigation on the electrostatic

characteristics in model pneumatic conveying systems. This would enable us to gain insights into the relationship between the solids flow behavior and electrostatic charges. Furthermore, in the future, typical important and interesting physical phenomena in the pneumatic conveying system may be further quantified. Examples of such phenomenon include special particulate flow patterns under electrostatic effects, evolution of particulate distribution with particle attrition, the presence of electrostatic field on solid flow pattern and its prediction for the occurrence of spark discharge.

Bibliography

Al-Adel, M. F., Savile, D. A., Sundaresan, S. The effect of static electrification on gas-solid flows in vertical risers. *Ind. Eng. Chem. Res.* **2002**, 41, 6224-6234.

Antonyuk, S., Tomas, J. Heinrich, S. Mörl, L. Breakage behaviour of spherical granulates by compression. *Chem. Eng. Sci.* **2005**, 60, 4031-4044.

Bemrose, C. R., Bridgwater, J. A review of attrition and attrition test methods. *Powder Technol.* **1987**, 49, 97-126.

Carstensen, J. T., Chan, P. C. Relation between particle size and repose angles of powders. *Powder Technol.* **1976**, 15, 129-131.

Chang, H., Louge, M. Fluid dynamic similarity of circulation fluidized beds. *Powder Technol.* **1992**, 70, 259-270.

Choi, B. S., Fletcher, C. A. J. Turbulent particle dispersion in an electrostatic precipitator. *Appl. Math. Model.* **1998**, 22, 1009-1021.

Dhodapkar, S. V., Klinzing, G. E. Pressure fluctuations in pneumatic conveying systems. *Powder Technol.* **1993**, 74, 179-195.

Diaz, A. F., Felix-Navarro, R. M. A semi-quantitative tribo-electric series for polymeric materials: the influence of chemical structure and properties *J. Electrostat.* **2004**, 62, 277-290.

Dyakowski, Y., Jaenmeure, L. F. C., Jaworski, A. J. Application of electrical tomography for gas-solids and liquid-solids flows----a review. *Powder Technol.* **2000**, 112, 174-192.

Fan, J. R., Yao, J., Cen, K. F. Antierosion in a 90 ºbend by particle impaction. *AIChE J.* **2002**, 48, 1401-1412.

Fitzpatrick, J. J., Barringer, S. A., Iqbal, T. Flow property measurement of food powders and sensitivity of Jenike's hopper design methodology to the measured values. *J. Food Eng.* **2004**, 61, 399-405.

Glor, M. Ignition hazard due to static electricity in particulate processes. *Powder Technol.* **2003**, 135-136, 223-233.

Goldfarb, D. J., Glasser, B. J., Shinbrot, T. Shear instabilities in granular flow. *Nature* **2002**, 415, 302-305.

Gorham, D. A., Salman, A. D., Pitt, M. J. Static and dynamic failure of PMMA spheres. *Powder Technol.* **2003**, 138, 229-238.

Gupta, R., Gidaspow, D., Wasan, D. T. Electrostatic separation of powder mixtures based on the work functions of its constituents. *Powder Technol.* **1993**, 75, 79-87.

Gwyn, J. E. On the particle size distribution function and the attrition of cracking catalysts. *AIChE J.* **1969**, 15, 35-39.

Hirota, M., Sogo, Y., Marutani, T., Suzuki, M. Effect of mechanical properties of powder on pneumatic conveying in inclined pipe. *Powder Technol.* **2002**, 122, 150-155.

Hua, J., Wang, C. H. Electrical capacitance tomography measurements of gravity-driven granular flow. *Ind. Eng. Chem. Res.* **1999**, 38, 621-630.

Inculet, I., Bousquet, J., Briens, C., Duchesne, E., Port, B. Reduction of electrostatic charging of particles in pneumatic conveying (patent pending). *J Electrostat.* **1997**, 40&41, 337-342.

Joseph, S., Klinzing, G. E. Vertical gas-solid transition flow with electrostatics. *Powder Technol.* **1983**, 36, 79-87.

Kanazawa, S., Ohkubo, T., Nomoto, Y., Adachi, T. Electrification of a pipe wall during powder transport. *J. Electrostat.* **1995**, 35, 47-54.

Kleber, W., Makin, B. Triboelectric powder coating: a practical approach for industrial use. *Particul. Sci. Technol.* **1998**, 16, 43-53.

Klinzing, G. E., Marcus, R. D., Rizk, F., Leung, L.S. Pneumatic conveying of solids: a theoretical and practical approach, second edition. London: Chapman and Hall. **1997**

Komatsu, T. S., Inagaki, S., Nakagawa, N. Nasuno, S. Creep motion in a granular pile exhibiting steady surface flow. *Phys. Rev. Lett.* **2001**, 86, 1757-1760.

Konami, M., Tanaka, S. Matsumoto, K. Attrition of granules during repeated pneumatic transport. *Powder Technol.* **2002**, 125, 82-88.

Leung, L. S., Wiles, R. J. Process design develop. *Ind. Eng. Chem. Res.* **1976**, 15, 652.

Levy, A., Mooney, T., Marjanovic, P., Mason, D. J. A comparison of analytical and numerical models with experimental data for gas-solid flow through a straight pipe at different inclinations. *Powder Technol.* **1997**, 93, 253-260.

Lim, E. W. C., Zhang, Y., Wang, C. H. Effects of an electrostatic field in pneumatic conveying of granular materials through inclined and vertical pipes. *Chem. Eng. Sci.* **2006**, 61, 7889-7908.

Machida, M., Scarlett, B. Development of displacement current tomography system. *Particul. Sci. Technol.* **1998**, 15, 36-41.

Maré, T., Voicu, I., Miriel, J. Numerical and experimental visualization of reverse flow in an inclined isothermal tube. *Exp. Therm. Fluid Sci.* **2005**, 30, 9-15.

Masuda, H., Komatsu, T., Iinoya, K. The static electrification of particles in gas-solid pipe flow. *AIChE J.* **1976**, 22, 558-564.

Masuda, H., Komatsu, T., Mitsui, N., Iinoya, K. Electrification of gas-solid suspensions flowing in steel and insulating-coated pipes. *J. Electrostat.* **1977**, 2, 341-350.

Masuda, H., Iinoya, K. Electrification of particles by impaction on inclined metal

plate. *AIChE J.* **1978**, 24, 950-956.

Mathur, M. P. Klinzing, G. E. Flow measurement in pneumatic transport of pulverized coal. *Powder Technol.* **1984**, 40, 309-321.

Matsusaka, S., Nishida, T., Gotoh, Y., Masuda, H. Electrification of fine particles by impact on a polymer film target. *Adv. Powder Technol.* **2003**, 14, 127-138.

Matsusaka, S., Masuda, H. Electrostatics of particles. *Adv. Powder Technol*. **2003,** 14, 143-166.

Matsusaka, S., Masuda, H. Simultaneous measurement of mass flow rate and charge-to-mass ratio of particles in gas-solids pipe flow. *Chem. Eng. Sci.* **2006**, 61, 2254-2261.

Molerus, O. Overview: pneumatic transport of solids. *Powder Technol.* **1996**, 88, 309-321.

Msosorov, V., Sankowski, D., Manzurkiewicz, L., Dyakowski, T. The 'best-correlated pixels' method for solid mass flow measurements using electrical capacitance tomography. *Meas. Sci. Technol*. **2002**, 13, 1810-1814.

Mueth, D. M., Debregeas, G. F., Karczmar, G. S., Eng, P. J., Nagel, S. R. Jaeger, H. M. Signatures of granular microstructure in dense shear flows. *Nature* **2000**, 406, 385-389.

Neil, A. U., Bridgwater, J. Attrition of particulate solids under shear. *Powder Technol.* **1994**, 80, 207-219.

Neil, A. U., Bridgwater, J. Towards a parameter characterising attrition. *Powder Technol.* **1999**, 106, 37-44.

Nieh, S., Nguyen, T. Effects of humidity, conveying velocity, and particle size on electrostatic charges of glass beads in a gaseous suspension flow. *J. Electrostat.* **1988**, 21, 99-114.

Paramanathan, B. K., Bridgwater, J. Attrition of solids-I Cell development. *Chem. Eng. Sci.* **1983a**, 38, 197-206.

Paramanathan, B. K., Bridgwater, J. Attrition of solids-II Material Behaviour and kinetics of attrition. *Chem. Eng. Sci.* **1983b**, 38, 207-224.

Rao, S. M., Zhu, K., Wang, C.-H., Sundaresan. S. Electrical capacitance tomography measurements on the pneumatic conveying of solids. *Ind. Eng. Chem. Res.* **2001**, 40, 4216–4226.

Salmana, A. D., Gorhamb, D. A., Szabo´ M., Hounslow, M. J. Spherical particle movement in dilute pneumatic conveying. *Powder Technol.* **2005**, 153, 43-50.

Schuhmann, R. Principles of comminution, I-Size distribution and standard calculations. *Mining Technol.* AIME TP **1940**, 1189, 1-11.

Shipway, P. H., Hutchings, I. M. Attrition of brittle spheres by fracture under compression and impact loading. *Powder Technol.* **1993**, 76, 23-30.

Smeltzer, E. E., Weaver, M. L., Klingzing, G. E. Individual electrostatic particle interaction in pneumatic transport. *Powder Technol.* **1982**, 33, 31-42.

Sommerfeld, M. Analysis of collision effects for turbulent gas-particle flow in a horizontal channel: Part I. particle transport. *Int. J. Multiphas Flow* **2003**, 29, 675-699.

Soo, S. L. Design of pneumatic conveying systems. *J. Powder Bulk Solids Technol.* **1980**, 4, 33-43.

Su, B. L., Zhang, Y. H., Peng, L. H., Yao, D. Y., Zhang, B. F. The use of simultaneous iterative reconstruction technique for electrical capacitance tomography. *Chem. Eng. J.* **2000**, 77, 37-41.

Teunou, E., Fitzpatrick, J. J., Synnott, E. C. Characterisation of food powder flowability. *J. Food Eng.* **1999**, 39, 31-37.

Tsuji, Y., Morikawa, Y. Flow pattern and pressure fluctuation in air-solid two-phase flow in a pipe at low air velocities. *Int. J. Multiphas. Flow*, **1982**, 8, 329-341.

Watano, S., Miyanami, K. Image processing for on-line monitoring of granule size distribution and shape in fluidized bed granulation. *Powder Technol.* **1995**, 83, 55-60.

Watano, S. Mechanism and control of electrification in pneumatic conveying of powders. *Chem Eng. Sci.* **2006**, 61, 2271-2278.

Willem, J. B., Gabrie, M. H. M., Todd, B., Alfred, G., Mark, G., Brian, S. Failure mechanism determination for industrial granules using a repeated compression test. *Powder Technol.* **2003**, 130, 367-376.

Wolny, A., Opalinski, I. Electric charge neutralization by addition of fines to a fluidized bed composed of coarse dielectric particles. *J. Electrostat.* **1983**, 14, 179-289.

Wypych, P., Hastie, D. Yi, J. Low-velocity pneumatic conveying technology for plastic pellets. *Proc. 6th World Cong. of Chem. Eng.* Melbourne, Australia, **2001**.

Yanar, D. K., Kwetkus, B. A. Electrostatic separation of polymer powders. *J. Electrostat*. **1995**, 35, 257-266.

Yao, J., Zhang, B. Z. Fan, J. R. An experimental investigation of a new method for protecting bends from erosion in gas-solid flows. *Wear* **2000**, 240, 215-222.

Yao, J., Zhang, Y., Wang, C. H., Matsusaka, S., Masuda, H. Electrostatics of the granular flow in a pneumatic conveying system. *Ind. Eng. Chem. Res.* **2004**, 43, 7181-7199.

Yao, J., Wang, C. H., Lim, W. C. E., Bridgwater, J. Granular attrition in a rotary valve: Attrition product size and shape. *Chem. Eng. Sci.* **2006a**, 61, 3435-3451.

Yao, J., Zhang, Y., Wang, C. H, Liang, Y. C. On the Electrostatic Equilibrium of Granular Flow in Pneumatic Conveying Systems. *AIChE J.* **2006b**, 52, 3775-3793.

Zhang, Y. F., Yang, Y., Arastoopour, H. Electrostatic effect on the flow behavior of a dilute gas/cohesive particle flow system. *AIChE J.* **1996**, 42, 1590-1599.

Zhou, Y. C., Xu, B. H. Yu, A. B. Numerical investigation of the angle of response of monosized spheres. *Phys. Rev. E.* **2001**, 64, 021301.

Zhu, K., Rao, S. M., Wang, C. H. Sundaresan, S. Electrical capacitance tomography measurements on vertical and inclined pneumatic conveying of granular solids. *Chem Eng. Sci.* **2003**, 58, 4225–4245.

Zhu, K, Wong, C. K., Rao, S. M., Wang, C. H. Pneumatic conveying of granular solids in horizontal and inclined pipes. *AIChE J.* **2004a**, 50, 1729-1745.

Zhu, K., Rao, S. M., Huang, Q. H., Wang, C. H., Matsusaka, S., Masuda, H. On the electrostatics of pneumatic conveying of granular materials using electrical capacitance tomography. *Chem. Eng. Sci.* **2004b**, 59, 3201-3213.

Appendix

From the Figure 4.19, the charges on the wall are assumed to be infinitesimal point charges, *dq*, and every particle is taken as a point charge, *Q*. The point charge on pipe wall is

$$dq=\lambda dz \tag{A.1}$$

here, λ is the linear charge density along pipe wall.

Therefore, according to the Coulomb's law, the electric field intensity on the point charge of particle due to the point charge on the pipe wall is

$$d\vec{E}=\frac{1}{4\pi\varepsilon_0}\frac{dq}{r^2}=\frac{\lambda dz}{4\pi\varepsilon_0(l^2+z^2)} \tag{A.2}$$

here, ε_0 is permittivity constant in vacuum; *r* is the distance from point charge on the pipe, *dq*, to object point charge of particle, *Q*; *l* is the vertical distance from pipe wall to object point charge.

The electric field intensities on the y axis and z axis due to the entire charged pipe wall are

$$\vec{E}_y=\int d\vec{E}_y=\int d\vec{E}\cdot\cos\theta \tag{A.3}$$

and

$$\vec{E}_z=\int d\vec{E}_z=\int d\vec{E}\cdot\sin\theta \tag{A.4}$$

Here, θ is the angle between *r* and *l*.

Thus

$$\vec{E}_y = \frac{\lambda}{4\pi\varepsilon_0}\int_{-\infty}^{\infty}\frac{\cos\theta}{l^2+z^2}dz \tag{A.5}$$

and

$$\vec{E}_z = \frac{\lambda}{4\pi\varepsilon_0}\int_{-\infty}^{\infty}\frac{\sin\theta}{l^2+z^2}dz \tag{A.6}$$

where, $dz=ld\tan\theta=ld\theta/\cos^2\theta$, and $l^2+z^2=l^2+(l\tan\theta)^2=l^2(1+\tan^2\theta)=l^2/\cos^2\theta$, respectively. Furthermore, when $z=\infty$, $\theta=\pi/2$; when $z=-\infty$, $\theta=-\pi/2$.

Therefore,

$$\vec{E}_y = \frac{\lambda}{4\pi\varepsilon_0}\int_{-\frac{\pi}{2}}^{\frac{\pi}{2}}\frac{\cos\theta}{l^2}d\theta = \frac{\lambda}{4\pi\varepsilon_0 l}\int_{-\frac{\pi}{2}}^{\frac{\pi}{2}}\cos\theta d\theta = \frac{\lambda}{2\pi\varepsilon_0 l} \tag{A.7}$$

and

$$\vec{E}_z = \frac{\lambda}{4\pi\varepsilon_0}\int_{-\frac{\pi}{2}}^{\frac{\pi}{2}}\frac{\sin\theta}{l^2}d\theta = \frac{\lambda}{4\pi\varepsilon_0 l}\int_{-\frac{\pi}{2}}^{\frac{\pi}{2}}\sin\theta d\theta = 0 \tag{A.8}$$

Therefore, the electric field intensity due to the charged pipe wall is represented as follows:

$$\vec{E} = \vec{E}_y = \frac{\lambda}{2\pi\varepsilon_0 l} \tag{A.9}$$

List of Publications

Yao, J., Zhang, Y., Wang, C. H., Matsusaka, S., Masuda. H. Electrostatics of the Granular Flow in a Pneumatic Conveying System, *Ind. Eng. Chem. Res.* **2004**, 43, 7181–7199.

Lim, W. C. E., Zhang, Y., Wang, C. H. Effects of an Electrostatic Field in Pneumatic Conveying of Granular Materials through Inclined and Vertical Pipes, *Chem. Eng. Sci.* **2006**, 61, 7889-7908.

Yao, J., Zhang, Y., Wang, C. H. Liang, C. Y. On the Electrostatic Equilibrium of Granular Flow in Pneumatic Conveying Systems, *AIChE J.* **2006**, 52, 3775-3793.

Zhang, Y., Wang, C. H. Particle Attrition due to Rotary Valve Feeder in a Pneumatic Conveying System: Electrostatics and Mechanical Characteristics, *Can. J. Chem. Eng.* **2006**, 84, 663-679.

Zhang, Y., Lim, W. C. E., Wang, C. H. Pneumatic Transport of Granular Materials in an Inclined Conveying Pipe: Comparison of CFD-DEM, ECT and PIV Results, *Ind. Eng. Chem. Res.* **2007**, in press.